

New approaches in squeezed light generation

-

**Quantum states of light with GHz squeezing bandwidth
and squeezed light generation via the cascaded Kerr effect**

Der Fakultät für Mathematik und Physik
der Gottfried Wilhelm Leibniz Universität Hannover
zur Erlangung des Grades

**Doktor der Naturwissenschaften
Dr. rer. nat.**

genehmigte Dissertation
von

Dipl.-Phys. Stefan Ast

geboren am 03. Oktober 1983 in Verden, Deutschland

2015

Referent: Prof. Dr. Roman Schnabel
Korreferent: Prof. Dr. Karsten Danzmann
Tag der Promotion 30.01.2015

für Oma Marga

Abstract

The first generation of squeezed states of light nearly 30 years ago marked the starting point for intensive research towards applications. One potential use of squeezed light is quantum key distribution (QKD). It enables the encryption of data with a mathematically proven security. Although QKD devices are already commercially available today, they lack in data rate as well as secure communication distance.

This thesis presents new approaches in nonclassical-light generation at the telecommunication wavelength of 1550 nm for potential applications in QKD. I developed three prototype nonlinear resonators for the generation of squeezed light. In this context, a highly efficient second harmonic generation cavity was realized having a conversion efficiency of 95 % at 1550 nm.

The first squeezing source was designed as a proof of principle experiment for the generation of a high-bandwidth spectrum of nonclassical light only limited by the phase matching of the nonlinear crystal.

The second squeezing resonator was a monolithic crystal cavity with a linewidth of 2.26 GHz. A fast homodyne detector with highly efficient photodiodes measured an average nonclassical noise suppression of 3.5 dB over a bandwidth of 1 GHz. Two of those compact resonators were set-up for the generation and detection of two-mode entangled light with GHz bandwidth. The resulting measurements violated the Duan inseparability criterion over the full spectrum.

The third experiment realized the generation and detection of continuous-wave squeezed states of light via the cascaded Kerr effect. A bow-tie type resonator was used to achieve a nonclassical noise suppression of up to 2.2 dB at a sideband frequency of 1.074 GHz and a carrier wavelength of 1550 nm.

The generated quantum states are suitable for boosting the data rate in QKD experiments and open new perspectives for fundamental research of quantum effects.

Keywords: Squeezed light, quantum key distribution, cascaded Kerr effect, entanglement, second harmonic generation

Kurzfassung

Die erstmalige Erzeugung von gequetschtem Licht vor nahezu 30 Jahren war der Startpunkt für eine intensive Erforschung dieser Technik in Richtung Anwendungen. Die Quantenschlüsselverteilung (QKD) stellt eine potenzielle Nutzung von gequetschtem Licht dar. Diese ermöglicht die Verschlüsselung von Daten mit einer mathematisch bewiesenen Sicherheit. Obwohl Geräte zur Quantenschlüsselverteilung bereits kommerziell erhältlich sind, haben sie Defizite in der Datenrate und der sicheren Übertragungsreichweite.

In dieser Arbeit werden neue Ansätze zur Erzeugung von nichtklassischem Licht bei der Telekommunikationswellenlänge von 1550 nm für mögliche Anwendungen in der Quantenschlüsselverteilung vorgestellt. Drei Prototypen von Quetschlichtresonatoren wurden hierfür entwickelt und eine hocheffiziente Frequenzverdopplung mit einer Konversionseffizienz von 95 % bei 1550 nm konnte realisiert werden.

Die erste Quetschlichtquelle diente als Machbarkeitsstudie zur Erzeugung eines Quetschlichtspektrums, dessen Bandbreite nur durch die Phasenanpassung des nichtlinearen Kristalls limitiert wurde.

Der zweite Quetschlichtresonator war ein monolithischer Kristall mit einer Linienbreite von 2,26 GHz. Ein schneller Homodyndetektor mit hocheffizienten Photodioden detektierte eine mittlere nichtklassische Rauschunterdrückung von 3,5 dB über eine Bandbreite von 1 GHz. Zwei dieser kompakten Resonatoren dienten zur Erzeugung und Detektion eines zwei-moden verschränkten Zustands mit GHz Bandbreite. Die anschließende Messung unterbot das Inseparabilitätskriterium von Duan über das gesamte Spektrum.

Das dritte Experiment realisierte die Erzeugung und Detektion von gequetschtem Licht im Dauerstrichbetrieb mittels des kaskadierten Kerr-effekts. Hierfür wurde ein gefalteter Wanderwellenresonator vom Typ *bow-tie* verwendet, welcher eine nichtklassische Rauschunterdrückung von bis zu 2,2 dB bei 1,074 GHz und einer Wellenlänge von 1550 nm erzielte.

Die generierten Quantenzustände sind in der Lage die Datenrate in QKD Experimenten zu erhöhen und eröffnen neue Perspektiven zur Erforschung fundamentaler Quanteneffekte.

Schlüsselworte: Gequetschtes Licht, Quantenschlüsselverteilung, kaskadierter Kerr-effekt, Verschränkung, Frequenzverdoppelung

Contents

Contents	9
List of Figures	13
List of Abbreviations	17
1. Introduction	21
1.1. Squeezed light enhanced interferometry	22
1.2. Quantum Key Distribution	23
1.3. The goal of this thesis	24
1.4. The structure of this thesis	25
2. Theory	27
2.1. Quadrature operators	27
2.2. Squeezed states of light	28
2.2.1. Two-mode squeezed states of light	30
2.3. Homodyne detection for squeezed states	31
2.4. Duan criterion for entanglement	34
2.5. Nonlinear optics	35
2.5.1. Optical parametric amplification	35
2.5.2. Cascaded Kerr effect	37
3. High conversion efficiency second harmonic generation	41
3.1. Introduction	41
3.1.1. Limitations for second harmonic generation	42
3.2. Experimental setup	43
3.2.1. Hemilithic SHG cavity	45
3.3. Pump depletion measurement concept	47
3.4. Experimental results	48
3.4.1. High-conversion pump depletion measurement	48
3.4.2. Estimated error for the pump depletion	49
3.4.3. Conversion versus pump power	50
3.5. Summary & Outlook	51

CONTENTS

4. Squeezed light source without squeezing resonator	53
4.1. Introduction	53
4.2. Design concept of the hemilithic high bandwidth squeezing source	54
4.3. Experimental setup	55
4.3.1. Hemilithic cavity mode-matching	56
4.4. Experimental results	58
4.4.1. Homodyne detector characterization	58
4.4.2. Squeezed light measurement	60
4.4.3. Total detection efficiency estimation	62
4.5. Summary & Outlook	63
5. High-bandwidth monolithic squeezing resonator	65
5.1. Introduction	65
5.2. Design of the monolithic crystal cavity	66
5.2.1. Squeezing optimization with N.L.C.S.	67
5.2.2. Monolithic crystal cavity mode degeneracy	68
5.3. Monolithic cavity parameters & crystal oven	70
5.4. Experimental setup	72
5.4.1. Cavity mode-matchings & parametric gain	73
5.5. Optical path loss estimation	76
5.6. Squeezed vacuum measurement with GHz bandwidth	76
5.6.1. GHz bandwidth homodyne detector characterization	76
5.6.2. First GHz bandwidth measurement	78
5.7. High detection efficiency MHz bandwidth measurement	79
5.8. High detection efficiency GHz bandwidth measurement	81
5.8.1. Custom-made GHz homodyne detector characterization	81
5.8.2. Stabilization techniques for the monolithic squeezing resonator	83
5.8.3. High detection efficiency measurement results	84
5.9. Parasitic frequency doubling in the monolithic crystal	86
5.10. Path difference for high-bandwidth homodyne detection	87
5.11. Summary & Outlook	88
6. GHz bandwidth entanglement generation	91
6.1. Introduction	91
6.2. Experimental setup	92
6.2.1. Stabilized homodyne detection	93
6.2.2. Mode-matchings for OPA1 and OPA2	94

6.2.3. Homodyne detector characterization	96
6.3. V-class entanglement measurement	97
6.4. S-class entanglement measurement	99
6.4.1. Duan criterion spectrum	101
6.5. Discussion of the total detection loss	103
6.6. Summary & Outlook	105
7. Squeezed light generated via the cascaded Kerr effect	107
7.1. Introduction	107
7.2. Designing the Kerr squeezing experiment	108
7.2.1. Kerr squeezing resonator design	109
7.2.2. Sideband extraction modecleaner concept	111
7.3. Experimental setup	112
7.3.1. Bow-tie & SEMC mode-matchings	112
7.3.2. Homodyne detector visibility	113
7.4. Measurement results	115
7.4.1. Kerr squeezing measurements at subsequent free spectral ranges	116
7.5. Simulated & estimated loss	118
7.6. Summary & Outlook	121
8. Conclusion	123
A. Appendix	125
A.1. Open-loop gain for the high conversion efficiency SHG	125
A.2. Monolithic squeezing resonator N.L.C.S. simulations .	126
A.2.1. Pictures from the experimental setup	128
A.3. Pump phase stabilization open-loop gain	131
A.4. GHz bandwidth homodyne detector circuit	131
A.5. GHz entanglement homodyne detector spectra	133
A.6. Kerr squeezing bow-tie experimental pictures	135
A.7. Kerr squeezing bow-tie CAD drawings	138
Bibliography	139
Acknowledgements	147
Curriculum Vitae	149
List of Publications	151

List of Figures

2.1. Phasor picture of the vacuum mode and the squeezed vacuum mode	29
2.2. Schematic of a typical balanced homodyne detection setup	32
2.3. Illustration of Kerr squeezing in the phasor picture representation	38
3.1. High-conversion SHG experimental setup	43
3.2. Measured mode-matching and PDH error signal for the modecleaner	44
3.3. SHG cavity transmitted signal	44
3.4. Mode-matching for the SHG cavity in reflection	46
3.5. SHG conversion vs. temperature	46
3.6. SHG pump depletion measurement for a fundamental input power of 1.1 W	49
3.7. Conversion efficiency and harmonic power (775 nm) versus fundamental input power (1550 nm)	50
4.1. Experimental setup of the hemilithic OPA	56
4.2. Hemilithic OPA: Pump field mode-matching and PDH error signal	57
4.3. Hemilithic OPA: Control field mode-matching	57
4.4. Balanced homodyne detector characterization with FCI-H250G-InGaAs-70 photodiodes	59
4.5. Characterization of the homodyne detector's linearity	59
4.6. Homodyne detector visibility	61
4.7. Normalized squeezing spectrum hemilithic squeezer	61
4.8. Loss simulation for the hemilithic squeezer	62
5.1. Monolithic squeezer: variation of the incoupling reflectivity	66
5.2. Monolithic squeezer: High harmonic power simulation	67
5.3. Mode degeneracy of a 2.6 mm monolithic PPKTP crystal cavity at 1550 nm	69

LIST OF FIGURES

5.4. Mode degeneracy of a 2.6 mm monolithic PPKTP crystal cavity at 775 nm	69
5.5. Monolithic squeezer: OPO threshold simulation	70
5.6. Schematic CAD drawing of the newly designed squeezing resonator oven construction	71
5.7. Schematic setup of the monolithic squeezing resonator experiment	72
5.8. Schematic setups for the mode-matching of control field and pump field	73
5.9. Control field and pump field mode-matchings of the monolithic squeezing resonator	75
5.10. Gain of the monolithic crystal cavity	75
5.11. Characterization of the <i>New Focus 1617-AC FS</i> homodyne detector	77
5.12. Normalized spectrum of the New Focus 1617-AC FS homodyne detector	77
5.13. Monolithic cavity squeezing measurement using New Focus 1617-AC FS homodyne detector	79
5.14. Squeezing measurement using high efficiency homodyne detector in the MHz frequency band	80
5.15. Characterization of high-bandwidth homodyne detector with high quantum efficiency photodiodes	82
5.16. Schematic of the pump phase and homodyne phase stabilization	83
5.17. Squeezing and anti-squeezing spectra for the fully locked experiment	85
5.18. Simulated loss for the best squeezing measurement	86
5.19. Incidental UV light generation in the monolithic squeezing resonator	87
5.20. Path length difference induced loss in GHz bandwidth squeezed light measurement	88
5.21. N.L.C.S. simulation to compare 12.3 dB squeezer and high-bandwidth squeezer	89
6.1. Setup for the GHz entanglement experiment	93
6.2. OPA 1 and OPA 2 control mode-matchings	95
6.3. OPA 1 and OPA 2 pump mode-matchings	95
6.4. Vacuum noise levels for the subtraction of two homodyne detectors	96

LIST OF FIGURES

6.5. Spectra of the v-class entanglement measurement of squeezing resonator 1	98
6.6. Normalized spectra of the v-class entanglement measurement of squeezing resonator 1	99
6.7. Spectra of the s-class entanglement measurement	100
6.8. Normalized spectra of the s-class entanglement measurement	101
6.9. Duan criterion for the s-class spectrum measurement	102
7.1. Schematic design of the bow-tie type Kerr squeezing resonator	109
7.2. Photograph of the Kerr squeezing bow-tie cavity with glass housing	110
7.3. Free spectral ranges Kerr squeezer vs. SEMC	111
7.4. Schematic of the experimental setup for Kerr squeezing	113
7.5. Mode-matchings: Bow-tie cavity and SEMC	114
7.6. Measured homodyne detection visibility	114
7.7. Kerr effect induced resonance peak deformation for the bow-tie resonator	115
7.8. Normalized Kerr squeezing spectrum at 358.3 MHz sideband frequency	117
7.9. Normalized Kerr squeezing spectrum at 1074.9 MHz sideband frequency	117
7.10. Loss simulation for the Kerr squeezing measurements	119
A.1. SHG open loop gain	125
A.2. Photograph of the pump path to the monolithic squeezing resonator	129
A.3. Photograph of the control field path of the monolithic squeezing resonator	129
A.4. Photograph of the inputs and outputs of the monolithic squeezing resonator oven	130
A.5. Open-loop gain of the pump phase lock for the monolithic squeezing resonator	131
A.6. Electronic circuit of the GHz bandwidth homodyne detector	132
A.7. Characterization of the two subtracted GHz homodyne detector signals	133
A.8. Characterization of GHz homodyne detector 1	134
A.9. Characterization of GHz homodyne detector 2	134

LIST OF FIGURES

A.10.Front view of the Kerr squeezing bow-tie resonator in the experimental setup	136
A.11.Front view of the Kerr squeezing bow-tie resonator . .	136
A.12.Side view of the Kerr squeezing bow-tie resonator . . .	137
A.13.Isometric view of the Kerr squeezing bow-tie resonator	137
A.14.Top view of the Kerr bow-tie CAD drawing	138
A.15.Isometric view of the Kerr bow-tie CAD drawing . . .	138

List of Abbreviations

\mathcal{F}	Finesse of a cavity
AC	Alternating current
AR	Anti-reflective coating
BHD	Balanced homodyne detector
CAD	Computer-aided design
CV	Continuous variable
cw	Continuous wave
DBS	Dichroic beam splitter
DC	Direct current
EOM	Electro-optic modulator
EPR	Einstein-Podolsky-Rosen
FSR	Free spectral range
FWHM	Full width at half maximum
GPS	Global positioning system
GW	Gravitational wave
HR	High-reflective coating
InGaAs	Indium gallium arsenide
KTP	Potassium titanyl phosphate
LIGO	Laser Interferometer Gravitational-Wave Observatory
LO	Local oscillator
MC	Modecleaner

LIST OF ABBREVIATIONS

N.L.C.S.	Nonlinear cavity simulator by Nico Lastzka
NTC	Negative Temperature Coefficient Thermistor
OPA	Optical parametric amplifier / squeezing resonator
PD	Photodiode / photodetector
PDC	Parametric down conversion
PDH	Pound-Drever-Hall
POM	Polyoxymethylene
PPKTP	Periodically poled potassium titanyl phosphate
QKD	Quantum key distribution
RBW	Resolution bandwidth
RoC	Radius of curvature
SEMC	Sideband extraction modecleaner
SHG	Second harmonic generation (cavity)
TEM	Transversal electromagnetic mode
TO	Transistor outline
UV	Ultra-violet
VBW	Video bandwidth

1

Chapter 1.

Introduction

Quadrature squeezed states of light are a special form of laser light showing a useful nonclassical quantum effect. The name “squeezed” light originates from the fact that its quasi-probability distribution in phase space has a distinct squeezed shape compared to (classical) coherent states. The variance of one of the electric field quadrature amplitudes (amplitude or phase) drops below the vacuum noise. Squeezing can be employed to enhance quantum noise limited measurements. It enables the operation of interferometric devices below their standard quantum limit [1, 2, 3]. Another feature of squeezed light is that it can be utilized to generate continuous-variable multi-mode entanglement [4]. Squeezed states of light are thus capable of being the resource for entanglement-based quantum key distribution (QKD) [5, 6, 7, 8]. They have become a useful tool in many quantum optical experiments since their theoretical prediction in 1976 as “two-photon coherent states” [9].

The first experimental realization of squeezed states of light in 1985 by Slusher et al. [10] promised to be a starting point for intensive research towards applications. For almost 20 years the progress in squeezing experiments has been suffering heavily under the fragile nature of squeezed light. Its vulnerability against decoherence (mostly optical loss) and the high complexity of experimental setups for squeezing generation were reasons for delayed progress of the promised “squeezing revolution”. However, scientists achieved the generation of squeezed states of light at a variety of optical wavelengths from about 500-1550 nm, and in recent years, squeezing factors of up to 12.7 dB [11, 12]. Squeezed light has not only been generated in the continuous-wave regime but also for pulsed lasers [13, 14, 15].

1. Introduction

The only method for the generation of squeezed light is via nonlinear optical processes. The first squeezing experiment used four-wave mixing in a sodium gas cell (Na), while other approaches were using optical parametric amplification [16, 17], the optical Kerr effect [18] or even ponderomotive squeezing generation via opto-mechanical oscillators [19]. Today, a common method of producing continuous-wave squeezing is optical parametric amplification in second-order nonlinear crystals placed inside optical resonators [20]. A benchmark experiment was performed in 2005 by Vahlbruch et al. [11]. They managed to generate a stable and strongly squeezed vacuum state with 10 dB of nonclassical noise suppression at 1064 nm. Current state of the art squeezing resonators are capable of producing nonclassical light with a noise suppression of up to 12.7 dB at 1064 nm and 1550 nm, but only within a frequency range of 10 Hz to 100 MHz [12, 21, 22]. However, squeezing bandwidths above 100 MHz have not been realized in continuous-wave squeezing experiments so far.

1.1. Squeezed light enhanced interferometry

The main contribution to the success in generating strongly squeezed light was performed by the gravitational wave detection community. Their scientific instruments were the first application of a squeezed light enhanced experiment.

Gravitational waves are ripples in the fabric of space-time traveling at the speed of light. They are caused by cataclysmic astrophysical events, such as supernovae explosions or the merger of two neutron stars [23]. By measuring changes in the distance between free falling test masses one can, in principle, detect gravitational waves. This idea is used in laser interferometric gravitational wave (GW) detectors. They consist of a Michelson-type interferometer with an armlength of several kilometers. Currently, there is a worldwide network of five ground-based GW detectors. The two LIGO detectors in Hanford and Livingston (US) have armlengths of about 4 km and are currently in an upgrade phase to their advanced configurations (2014) [24]. There are two European detectors VIRGO [25] in Cascina (Italy) with 3 km long arms and GEO 600 [26] near Hannover (Germany) with 1.2 km long folded arms. The fifth detector is KAGRA [27] which is currently being installed in the Kamioka mine (Japan) using cryogenically cooled mirrors and an armlength of 3 km.

All ground-based GW detectors are limited by photon shot noise in

1.2. Quantum Key Distribution

a certain frequency range. The injection of squeezed states of light offers a reduction of the vacuum noise entering the output port of the GW detector and improves their measurement sensitivity.

The first detector using squeezed states of light was GEO 600 in 2011 [28], followed by LIGO Hanford in 2013 [29]. GEO 600 however was the only GW detector continuously using squeezed light in science mode, from 2011-2014 [30]. A squeezed light improvement of 3.7 dB was achieved, corresponding to a factor of 1.5 in sensitivity enhancement. This means a 3.6-fold increase in the observational volume for gravitational-wave events in the universe.

The design of third generation GW detectors (2020+) is planned to operate with a squeezing enhancement factor of 10 (e.g. the Einstein telescope design study [31]). Current state-of-the-art squeezed light sources already fulfill the requirements for these future detectors.

1.2. Quantum Key Distribution

Quantum key distribution uses quantum states to generate a secret key between two parties. This secret key can be used to encrypt data streams with a mathematically proven security, which is unachievable with today's common cryptographic systems. The level of security is granted through the “no-cloning” theorem of quantum theory, which ultimately originates from the collapse of the quantum mechanical wave function [32, 33].

Only recently, Eberle [34] was able to distribute an unconditionally secure quantum key with 1.5 MB by measuring 10^8 samples of Einstein-Podolsky-Rosen entangled light. The setup used optical parametric amplification in a squeezing resonator to generate the quantum state by superimposing two squeezed light fields on a beam splitter. The experiment was limited in secret key data rate through the finite measurement sample size of 10^8 as well as in secure distance to about 30 km.

The ultimate goal of QKD devices will be to establish a quantum network for multiple parties over large areas with high data rates. This demands an enhanced secret key rate for the future. The secret key size of 1.5 MB was quite small when compared to applications like the Internet, where data rates of several tens of MB per second are commonly used. Especially since a one time pad key encryption requires the secret key to have the same length as the encoded data [35]. This means the experiment generating the key with 1.5 MB is only able to

1. Introduction

decode a simple photograph from a digital camera with its 10^8 measurements. For the encoding of videos or other larger data packages, it lacks in data rate.

A new approach in squeezed light generation is necessary to overcome the limitations for two-mode squeezing based quantum key distribution.

1.3. The goal of this thesis

The development of squeezed light sources has successfully matured to fulfill even the demands of third generation gravitational wave detectors. However, their potential in quantum key distribution has only been explored to act as proof-of-principle devices so far. In particular, the robustness against decoherence and the data rate are under intense investigation.

This thesis focuses mainly on further developing the centerpiece of continuous-variable QKD experiments with squeezed light: the non-classical light source.

The data rate for entanglement based QKD using squeezed states is dependent on the squeezing strength and is proportional to the squeezing bandwidth. While the first increases the average number of bits per measurement, the latter will allow a higher measuring speed. Thus both increase the key rate. The highest bandwidth for continuous-wave squeezed light before this work was measured in [36] where 100 MHz and a nonclassical noise suppression of up to 11.5 dB was achieved at 1064 nm. One approach for applications of QKD is the distribution of continuous variable (CV) entangled states via standard telecommunication fibers [37, 38]. The wavelength of 1550 nm offers the advantage of low optical loss in the fibers, which is necessary to protect the entanglement against decoherence [39]. In a km scale fiber network, however, decoherence will still be the limiting factor and the squeezing bandwidth is more robust than the squeezing strength.

The main part of this thesis is dedicated to experiments for the generation of squeezed and entangled states of light with high-bandwidth for future QKD applications. In this context, a second harmonic generation with the highest ever observed conversion efficiency was experimentally demonstrated. The high efficiency was necessary to produce strong pump fields for the process of high-bandwidth optical parametric amplification. Additionally, I will describe the first experimental demonstration of squeezed light via a cascaded Kerr nonlinear res-

1.4. The structure of this thesis

onator. The Kerr effect without resonator promises to be a useful tool for the generation of non-gaussian states of light in the future. These states have highly nonclassical properties and are interesting for fundamental research of quantum phenomena.

1.4. The structure of this thesis

- Chapter 2 will start with a description of the theoretical background for squeezed states of light and their generation. It will introduce quadrature operators, squeezed states of light and homodyne detection. In this context, I will explain the nonlinear processes of optical parametric amplification and the cascaded Kerr effect. Additionally, I will present the Duan criterion for continuous variable entanglement, which was used in this thesis.
- Chapter 3 is dedicated to an experimental setup for a high conversion efficiency second harmonic generation cavity. I will introduce a method of measuring the conversion efficiency with a small relative error through pump depletion. The results will show the highest ever observed efficiency in any frequency doubling device so far.
- Chapter 4 introduces the first experimental approach to produce cw squeezed vacuum without a cavity for the fundamental field. I will report on the highest ever observed continuous wave squeezing bandwidth so far. The experiences from this experiment lead to a superior squeezing resonator design, which will be discussed in the next chapter.
- Chapter 5 reports on a compact monolithic squeezing resonator with a very high free spectral range (FSR) for the generation of strong squeezing over a bandwidth of several GHz. The source was built to be used for two-mode entanglement generation for applications in quantum key distribution.
- Chapter 6 uses two of the aforementioned squeezing resonators to show a proof-of-principle measurement of two-mode entangled states with GHz bandwidth. Two homodyne detectors with 99 % efficiency photodiodes were used to measure the entanglement.
- Chapter 7 will demonstrate, for the first time, the generation of squeezed states of light via the cascaded Kerr effect with a non-

1. Introduction

classical noise suppression below the vacuum noise. The experiment used a high finesse bow-tie cavity with a periodically-poled potassium titanyl phosphate crystal and a sideband extraction method to detect the squeezed field at high MHz frequencies.

- Chapter 8 will conclude with a summary and an outlook of the new prospects in squeezed and entangled light generation.

2

Chapter 2.

Theory

This chapter sketches some theoretical background about the experiments performed throughout the thesis. I follow the review article “Quantum information with continuous variables” by Braunstein and van Loock [40].

The chapter introduces quadrature operators of the electromagnetic radiation field. The single-mode quadrature squeezed states as well as two-mode squeezed states are derived, and homodyne detection as a technique to measure squeezed light is discussed. The Duan criterion for entanglement is explained afterwards. The last part focuses on concepts in nonlinear optics for squeezed light generation used in this thesis.

2.1. Quadrature operators

In quantum optics, the quadrature operators for a quantized field are formally equivalent to the classical position and momentum of an oscillator. They are non-commuting Hermitian operators and thus the oscillators position and momentum obey a Heisenberg uncertainty relation. Effectively this gives rise to the non-zero quantum mechanical vacuum energy and thus vacuum noise.

The Hamiltonian of a quantum harmonic oscillator with unit mass using the creation and the annihilation operators for a single mode k reads

$$\hat{H}_k = \hbar\omega_k \left(\hat{a}_k^\dagger \hat{a}_k + \frac{1}{2} \right), \quad (2.1)$$

with \hbar the reduced Planck constant, ω the oscillator eigenfrequency, the annihilation operator \hat{a} , the creation operator \hat{a}^\dagger and k as an index

2. Theory

for the k -th mode of the electromagnetic field.

In terms of position and momentum operators the Hamiltonian has the form

$$\hat{H}_k = \hbar\omega_k (\hat{x}_k^2 + \hat{p}_k^2), \quad (2.2)$$

with the dimensionless position and momentum operators

$$\hat{x}_k = (\hat{a}_k + \hat{a}_k^\dagger)/2 \quad (2.3)$$

and

$$\hat{p}_k = (\hat{a}_k - \hat{a}_k^\dagger)/2i. \quad (2.4)$$

These operators are the quadratures of a single mode k and also correspond to the amplitude and the phase of the electromagnetic field. They obey a commutation relation

$$[\hat{x}_k, \hat{p}_{k'}] = \frac{i}{2} \delta_{kk'}, \quad (2.5)$$

which results in a Heisenberg uncertainty relation for the variances of position and momentum

$$\langle (\Delta\hat{x}_k)^2 \rangle \langle (\Delta\hat{p}_k)^2 \rangle \geq \frac{1}{4} |\langle [\hat{x}_k, \hat{p}_k] \rangle|^2 = \frac{1}{16}. \quad (2.6)$$

This is the vacuum fluctuation of the electromagnetic field. For the example of a single mode coherent state, each quadrature contributes a variance of $1/4$. The Heisenberg uncertainty principle only restricts the product of the variance of amplitude and phase quadrature from being less than $1/16$. The individual quadratures, however, can drop below the vacuum level, which means that the amplitude *or* phase can be measured more precisely than for an ordinary vacuum state. This will be discussed in the next section.

2.2. Squeezed states of light

A squeezed state of light is defined by $\langle (\Delta\hat{x}_k)^2 \rangle \neq \langle (\Delta\hat{p}_k)^2 \rangle$, where either $\langle (\Delta\hat{x}_k)^2 \rangle < 1/16$ or $\langle (\Delta\hat{p}_k)^2 \rangle < 1/16$. These states still have to fulfill the Heisenberg uncertainty relation. However, the amplitude fluctuations or the phase fluctuation, which are equivalent to the position and momentum operator respectively, can drop below the vacuum level. The uncertainty of the state is therefore “squeezed” in one of its observables, while the uncertainty at the conjugate variable is “anti-squeezed”.

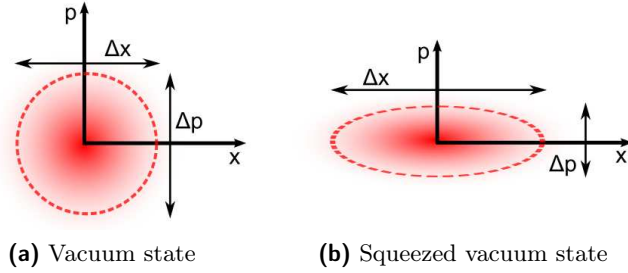


Figure 2.1.: Visualization of the (coherent) vacuum mode and the squeezed vacuum mode as gaussian quasi-probability distributions in the phasor picture. A minimal noise ellipse is necessary due to Heisenberg's uncertainty relation. These are the so-called vacuum fluctuations of the electromagnetic field. However, one quadrature can be squeezed below the vacuum noise level at the expense of an anti-squeezing of the orthogonal quadrature.

Mathematically, a single-mode vacuum operator \hat{a} or \hat{a}^\dagger of the electromagnetic field can be transformed by the unitary operator

$$\hat{S}(\zeta) = \exp\left(\frac{\zeta^*}{2}\hat{a}^2 - \frac{\zeta}{2}\hat{a}^{\dagger 2}\right). \quad (2.7)$$

This is the squeezing operator with $\zeta = -r \exp(i\Theta)$, where r denotes the squeezing factor and Θ is an angle changing the quadrature to be squeezed.

By applying the squeezing operator to the single mode vacuum operators \hat{a} and \hat{a}^\dagger we obtain

$$\hat{S}^\dagger(\zeta)\hat{a}\hat{S}(\zeta) = \hat{a} \cosh r + \hat{a}^\dagger e^{i\Theta} \sinh r, \quad (2.8)$$

$$\hat{S}^\dagger(\zeta)\hat{a}^\dagger\hat{S}(\zeta) = \hat{a}^\dagger \cosh r + \hat{a} e^{-i\Theta} \sinh r. \quad (2.9)$$

We define the rotated quadrature operators of position and momentum as

$$\hat{x}^{(\Theta)} = (\hat{a}e^{-i\Theta} + \hat{a}^\dagger e^{i\Theta})/2, \quad (2.10)$$

$$\hat{p}^{(\Theta)} = (\hat{a}e^{-i\Theta} - \hat{a}^\dagger e^{i\Theta})/2i, \quad (2.11)$$

where the whole continuum of quadratures is covered by $\hat{x}^{(\Theta)}$, since $\hat{p}^{(\Theta)} = \hat{x}^{\Theta+\pi/2}$.

The rotated mode

$$\hat{x}^{(\Theta/2)} + i\hat{p}^{(\Theta/2)} = (\hat{x} + i\hat{p})e^{-i\Theta/2} = \hat{a}e^{-i\Theta/2} \quad (2.12)$$

2. Theory

can be transformed by the squeezing operator to

$$\hat{S}^\dagger(\zeta)(\hat{x}^{(\Theta/2)} + i\hat{p}^{(\Theta/2)})\hat{S}(\zeta) = e^{+r}\hat{x}^{(\Theta/2)} + ie^{-r}\hat{p}^{(\Theta/2)}. \quad (2.13)$$

By using $\Theta = 0$ the position and momentum operators transform as

$$\hat{x}(r) = e^{+r}\hat{x}^{(0)}, \quad \hat{p}(r) = e^{-r}\hat{p}^{(0)} \quad (2.14)$$

resulting in an amplification of one quadrature and an attenuation of the other with a strength determined by the squeezing factor r . A visualization of the coherent vacuum and the squeezed vacuum in a phasor picture using the quadratures for x and p is depicted in Fig. 2.1. Experimentally, the squeezing operator is achievable via nonlinear optical effects. They will be discussed in section 2.5.

2.2.1. Two-mode squeezed states of light

Two-mode squeezed states can be experimentally realized by overlapping two single-mode squeezed vacuum states

$$\hat{a}_1(r) = \hat{a}_1 \cosh r + \hat{a}_1^\dagger \sinh r, \quad (2.15)$$

$$\hat{a}_2(r) = \hat{a}_2 \cosh r - \hat{a}_2^\dagger \sinh r, \quad (2.16)$$

on a 50/50 beam splitter with a relative phase of 90° .

This yields the two-mode squeezed fields

$$\hat{b}_1(r) = (\hat{a}_1(r) + \hat{a}_2(r))/\sqrt{2} = \hat{b}_1 \cosh r + \hat{b}_2^\dagger \sinh r, \quad (2.17)$$

$$\hat{b}_2(r) = (\hat{a}_1(r) - \hat{a}_2(r))/\sqrt{2} = \hat{b}_2 \cosh r + \hat{b}_1^\dagger \sinh r. \quad (2.18)$$

The field operators $\hat{b}_1(r)$ and $\hat{b}_2(r)$ are the output ports of the beam splitter and will show quadrature entanglement. This can be seen by rewriting the field operators with the rotated quadrature operators of position and momentum

$$\hat{x}_1(r) = (e^{+r}\hat{x}_1^{(0)} + e^{-r}\hat{x}_2^{(0)})/\sqrt{2}, \quad (2.19)$$

$$\hat{p}_1(r) = (e^{-r}\hat{p}_1^{(0)} + e^{+r}\hat{p}_2^{(0)})/\sqrt{2}, \quad (2.20)$$

$$\hat{x}_2(r) = (e^{+r}\hat{x}_1^{(0)} - e^{-r}\hat{x}_2^{(0)})/\sqrt{2}, \quad (2.21)$$

$$\hat{p}_2(r) = (e^{-r}\hat{p}_1^{(0)} - e^{+r}\hat{p}_2^{(0)})/\sqrt{2}. \quad (2.22)$$

The individual quadratures variances of $(\hat{x}_1, \hat{x}_2, \hat{p}_1, \hat{p}_2)(r)$ will be higher than the combined vacuum variance of $1/2$ for two modes.

2.3. Homodyne detection for squeezed states

Considering the difference of the position operators as well as the sum of the momentum operators

$$\hat{x}_1(r) - \hat{x}_2(r) = \sqrt{2}e^{-r}\hat{x}_2^{(0)}, \quad (2.23)$$

$$\hat{p}_1(r) + \hat{p}_2(r) = \sqrt{2}e^{-r}\hat{p}_1^{(0)}, \quad (2.24)$$

the variances of both will be below the vacuum level with

$$\langle(\hat{x}_1 - \hat{x}_2)^2\rangle = e^{-2r}/2 \quad (2.25)$$

and

$$\langle(\hat{p}_1 + \hat{p}_2)^2\rangle = e^{-2r}/2. \quad (2.26)$$

This is referred to as quadrature entanglement. The existence of such states was first discussed in the famous gedanken experiment by Einstein, Podolsky and Rosen [41]. Note that equation 2.25 & 2.26 only refer to a measurement of the relative position and the total momentum. Therefore, it does not violate Heisenberg's uncertainty relation. We name the situation of overlapping two single-mode squeezed states with $r_{1,2} > 0$ "s-class" entanglement. On the other hand the situation of overlapping one single-mode squeezed state with vacuum are named "v-class" entanglement.

In practice, a squeezed state of light will be comprised of a continuum of modes and the squeezing factor r could very well not be equal for both modes. Those effects can be derived in analogy to the calculations in this chapter and do not offer new insights for us. For further details the reader is referred to [40].

2.3. Homodyne detection for squeezed states

The most common method in measuring squeezed states of light is balanced homodyne detection [42, 43], which was also used throughout the experiments in this thesis. It is implemented by superimposing a bright local oscillator beam with the signal (squeezed) field on a balanced beam splitter (see Fig. 2.2). The phase of the local oscillator with respect to the signal beam determines the measured quadrature angle. Both outputs of the beam splitter are being detected and the subtracted signals yield the desired expectation value of the signal field.

The mode of the local oscillator will be denoted by \hat{b} , while the mode of the signal field will be denoted by \hat{a} . Additionally, the phase induced

2. Theory

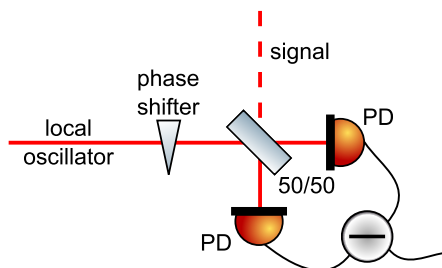


Figure 2.2.: Schematic of a typical balanced homodyne detection setup. A bright local oscillator field is superimposed with a weak signal field on a 50/50 beam splitter. Two photodiodes detect the outputs of the balanced beam splitter and their photo currents are directly subtracted. A phase shifting mirror is placed in the local oscillator path before the beam splitter to adjust the readout phase for the homodyne detection.

to the local oscillator beam is denoted by φ .

After superimposing the two modes at the balanced beam splitter, the output modes are

$$\hat{c} = \frac{1}{\sqrt{2}}(\hat{a} + \hat{b}e^{i\varphi}), \quad (2.27)$$

$$\hat{d} = \frac{1}{\sqrt{2}}(\hat{a} - \hat{b}e^{i\varphi}). \quad (2.28)$$

The photo currents are acquired by multiplying the output modes with their complex conjugate

$$\hat{i}_1 \propto \frac{1}{2}(\hat{a}^\dagger + \hat{b}^\dagger e^{-i\varphi})(\hat{a} + \hat{b}e^{i\varphi}), \quad (2.29)$$

$$\hat{i}_2 \propto \frac{1}{2}(\hat{a}^\dagger - \hat{b}^\dagger e^{-i\varphi})(\hat{a} - \hat{b}e^{i\varphi}). \quad (2.30)$$

The subtracted photo currents will take the following form

$$\hat{i}_1 - \hat{i}_2 \propto (\hat{a}^\dagger \hat{b}e^{i\varphi})^\dagger + \hat{a}^\dagger \hat{b}e^{i\varphi}. \quad (2.31)$$

This was achieved under the assumption that the photodiodes have the same gain and thus that the proportionality factor is the same.

The modes can be linearized as $\hat{a} = |\alpha\rangle + \delta\hat{\alpha}$ and $\hat{b} = |\beta\rangle + \delta\hat{\beta}$, which assumes that the operators are composed of the coherent excitation α, β and the fluctuation/noise $\delta\hat{\alpha}, \delta\hat{\beta}$. The latter are meant to be small and thus only the first order noise terms are taken into account. This will lead to the expression

$$\begin{aligned} \hat{i}_1 - \hat{i}_2 \propto 2|\alpha||\beta|\cos\varphi + |\beta|(\delta\hat{\alpha}^\dagger e^{i\varphi} + \delta\hat{\alpha}e^{-i\varphi}) \\ + |\alpha|(\delta\hat{\beta}^\dagger e^{-i\varphi} + \delta\hat{\beta}e^{i\varphi}). \end{aligned} \quad (2.32)$$

2.3. Homodyne detection for squeezed states

The second term contains the noise of the signal field amplified by the coherent excitation of the local oscillator. This enables the measurement of the \hat{x} quadrature with $\varphi = 0$ and the \hat{p} quadrature with $\varphi = \frac{\pi}{2}$ from section 2.2. To not measure the local oscillator noise, one has to assume that the local oscillator power $|\beta|$ is much larger than $|\alpha|$. For squeezed vacuum states this is indeed the case with $|\alpha| = 0$. Note that the first term of equation 2.32 describes the beat between the local oscillator and the control beam. This can be used as an error signal for a stabilization of the local oscillator phase with respect to the squeezed phase and thus gives us access to the \hat{p} quadrature (see section 5.8.2).

The squeezed light measurements throughout this thesis were taken at high sideband frequencies. In this case, a path difference after the outputs of the beam splitter to the photodiodes will lead to a phase shift of $e^{i\Delta\phi_{\text{SB}}}$, where

$$\Delta\phi_{\text{SB}} = \frac{2\pi\Delta L}{\lambda_{\text{SB}}}. \quad (2.33)$$

In this equation ΔL is the path difference in meters and λ_{SB} is the wavelength of the sideband frequency to be measured. This path difference is introduced after superimposing the local oscillator and the signal field and will thus lead to a varying photo current in one diode of

$$\hat{i}_1^* \propto \frac{1}{2}(\hat{a}^\dagger + \hat{b}^\dagger e^{-i\varphi})(\hat{a} + \hat{b}e^{i\varphi}) \cdot e^{i\Delta\phi_{\text{SB}}}, \quad (2.34)$$

$$\hat{i}_2^* \propto \frac{1}{2}(\hat{a}^\dagger - \hat{b}^\dagger e^{-i\varphi})(\hat{a} - \hat{b}e^{i\varphi}). \quad (2.35)$$

Therefore, the subtracted photo currents have the form

$$\begin{aligned} \hat{i}_1^* - \hat{i}_2^* \propto & \hat{b}^\dagger \hat{b} (e^{i\Delta\phi_{\text{SB}}} - 1) + (\hat{a}^\dagger \hat{a})^\dagger (e^{-i(\varphi + \Delta\phi_{\text{SB}})} + e^{-i\varphi}) \\ & + \hat{a}^\dagger \hat{b} (e^{i(\varphi + \Delta\phi_{\text{SB}})} + e^{i\varphi}) + \hat{a}^\dagger \hat{a} (e^{i\Delta\phi_{\text{SB}}} - 1), \end{aligned} \quad (2.36)$$

which can be simplified by using two special cases. The case of no path difference with $\Delta\phi_{\text{SB}} = 0$ will lead to the normal homodyne detection as calculated before. For a path length difference of $\Delta L = \frac{\lambda_{\text{SB}}}{2}$ the equation 2.36 will transform to

$$\hat{i}_1^* - \hat{i}_2^* \propto \hat{b}^\dagger \hat{b} + \hat{a}^\dagger \hat{a}. \quad (2.37)$$

Using the linearization $\hat{a} = |\alpha| + \delta\hat{a}$ and $\hat{b} = |\beta| + \delta\hat{b}$ as well as the approximation from before, this will yield

$$\hat{i}_1^* - \hat{i}_2^* \propto |\beta|^2 + |\beta| (\delta\hat{b}^\dagger + \delta\hat{b}). \quad (2.38)$$

2. Theory

The homodyne detection in this case will only measure the noise of the local oscillator ($\delta\hat{\beta}, \delta\hat{\beta}^\dagger$) and no contribution from the signal (squeezed noise). However, the effect is only visible at high sideband frequencies, where a path length difference is on the same order as the sideband wavelength. For example, performing a sideband frequency measurement at 5 MHz, the path length difference has to be on the order of $\Delta L = 30$ m. On the other hand, the sideband frequency measurement at 1 GHz will exhibit this effect with a path length difference of only $\Delta L = 0.15$ m. When acquiring a spectrum with a path length difference, one will observe a mixture of the noises from the (squeezed) signal and the local oscillator. Effectively, the squeezed spectrum will degrade at higher measurement frequencies. Avoiding this effect at high frequency measurements of squeezed light is the topic of section 5.10.

2.4. Duan criterion for entanglement

It is possible to give a measure of the entanglement strength for a continuous-variable bipartite state using the criterion by Duan et al. [44].

The Duan criterion defines two ‘‘EPR-type’’ operators

$$\hat{x}_{AB} = |a| \hat{x}_A - \frac{1}{a} \hat{x}_B, \quad \hat{p}_{AB} = |a| \hat{p}_A + \frac{1}{a} \hat{p}_B, \quad (2.39)$$

with the real number $a \neq 0$. The operators have to obey a commutation relation

$$[\hat{x}_j, \hat{p}_k] = i\delta_{jk}. \quad (2.40)$$

The sum of their variances has to fulfill the following inequality

$$\Delta^2 \hat{x}_{AB} + \Delta^2 \hat{p}_{AB} \geq a^2 + \frac{1}{a^2} \quad (2.41)$$

if they represent a separable state.

Rewriting the relation in terms of measured quadrature variance, one finds for a non-separable state:

$$\Delta^2(\hat{x}_A - \hat{x}_B) + \Delta^2(\hat{p}_A + \hat{p}_B) < 1, \quad (2.42)$$

using the A & B as the bipartite measuring devices, e.g. two homodyne detectors A & B.

Measuring two uncorrelated vacuum states at detectors A and B yields

1, as shown in equation 2.42. Measuring the variances for the sum and difference of the orthogonal quadratures would therefore yield a value below that of the combined vacuum state of 1. Two-mode squeezed states violate this inequality and are therefore inseparable. A value closer to zero means a stronger inseparability of the bipartite state.

2.5. Nonlinear optics

The field of nonlinear optics arises from the higher order terms in the infinite Taylor-expansion of the optical polarization for an electromagnetic field

$$P(E) = \epsilon_0 \left(\chi^{(1)}E + \chi^{(2)}E^2 + \chi^{(3)}E^3 + \dots \right). \quad (2.43)$$

This equation uses $P(E)$ as the polarization induced by an electric field E , where ϵ_0 is the dielectric constant and the $\chi^{(n)}$ refer to the dielectric susceptibility of n-th order. The $\chi^{(n)}$ depend upon material parameters in the nonlinear media, for example inside a crystal. An electric field E will therefore induce not only the linear term of the field polarization $\chi^{(1)}$ but also the higher order terms, given the electric field strength is high enough. In this context high enough means for example a strong laser pump field of several Watts of power with a small waist size inside a crystal. Typical crystal nonlinearities are on the order of $\chi^{(2)} \propto 10^{-12}$ m/V and $\chi^{(3)} \propto 10^{-15}$ m/V and thus extremely small.

In the following, I will describe the generation of squeezed light via the $\chi^{(2)}$ effect of *optical parametric amplification* and I will introduce the *cascaded Kerr effect* as a special case for a $\chi^{(2)}$ effect mimicking the third order *Kerr effect*. There are experimental realizations of both effects discussed throughout this thesis.

2.5.1. Optical parametric amplification

The second order nonlinear effect of optical parametric amplification is probably the most successful technique in the generation of squeezed states of light today. I will discuss degenerate parametric amplification, where the so called signal and idler fields both have the same frequency which is half the pump frequency. This pump acts as a driving field for the vacuum fluctuations of signal and idler, thus creating photon pairs, which give rise to the quadrature squeezing.

2. Theory

The interaction Hamiltonian for a parametric process can be expressed as

$$\hat{H}_{\text{int}} = i\hbar \frac{\kappa}{2} (\hat{a}^{\dagger 2} e^{i\Theta} - \hat{a}^2 e^{-i\Theta}). \quad (2.44)$$

The equation uses $\kappa \propto \chi^{(2)} |\alpha_{\text{pump}}|$ as a parameter including the second order nonlinearity of the medium $\chi^{(2)}$ and the real amplitude of the coherent pump mode $|\alpha_{\text{pump}}|$. Note that this is the so-called parametric approximation for no pump depletion and thus treats the pump as a classical field. κ immediately shows that a high nonlinearity of the medium combined with a high pump amplitude will enable a high interaction. Furthermore, Θ represents the pump phase and changes between amplification of the signal mode \hat{a} and the idler mode \hat{a}^\dagger at half the pump frequency.

Inserting the interaction Hamiltonian \hat{H}_{int} into the Heisenberg equation of motion for the annihilation operator will lead to

$$\frac{d}{dt} \hat{a}(t) = \frac{1}{i\hbar} [\hat{a}(t), \hat{H}_{\text{int}}] = \kappa \hat{a}^\dagger(t). \quad (2.45)$$

The solution for this equation is

$$\hat{a}(t) = \hat{a}(0) \cosh(\kappa t) + \hat{a}^\dagger(0) \sinh(\kappa t). \quad (2.46)$$

This time evolution with the Heisenberg equation of motion for the quadrature operators correspondingly leads to

$$\hat{x}(t) = e^{+\kappa t} \hat{x}(0), \quad \hat{p}(t) = e^{-\kappa t} \hat{p}(0). \quad (2.47)$$

The evolution of the quadrature operators due to a parametric interaction is thus equivalent to the squeezed quadratures from equation 2.14 using $\kappa t = r$. This is clarified by using the unitary evolution of the interaction Hamiltonian from equation 2.44

$$\hat{U}(t, 0) = \exp \left[\frac{\kappa}{2} (\hat{a}^{\dagger 2} e^{i\Theta} - \hat{a}^2 e^{-i\Theta}) t \right], \quad (2.48)$$

which is exactly the squeezing operator from equation 2.7

$$\hat{S}(\zeta) = \exp \left(\frac{\zeta^*}{2} \hat{a}^2 - \frac{\zeta}{2} \hat{a}^{\dagger 2} \right).$$

The time as a constant in the squeezing factor $r = \kappa t$ shows that not only the pump amplitude $|\alpha_{\text{pump}}|$ and the effective nonlinearity $\chi^{(2)}$ are important but also the interaction time of the fields in the

nonlinear medium. A parametric amplifier in an optical cavity for the signal/idler field can greatly enhance this interaction time, while an optical cavity for the pump enhances the pump amplitude. The bandwidth of the squeezed field and thus the continuum mode content is however also affected by the cavity. To achieve a high bandwidth for the squeezing, the cavity for the squeezed frequency (signal/idler) has to be of comparably low finesse. This has been discussed in [45]. Throughout the thesis the signal/idler field and thus the squeezed field will be at a wavelength of 1550 nm, while the pump field will constitute of 775 nm laser light.

2.5.2. Cascaded Kerr effect

The optical Kerr effect refers to a third order nonlinear effect ($\chi^{(3)}$) and is also capable of generating quadrature squeezed light. This can be physically explained by an intensity dependent phase shift for the fundamental pump field of

$$\phi(z) \propto \phi_0(z) \pm \chi^{(3)} z^2 I_{\text{fund}}, \quad (2.49)$$

induced by the nonlinear Kerr effect. The equation describes the phase shift $\phi(z)$ with respect to the propagation coordinate z . It consists of the initial phase shift $\phi_0(z)$ due to the propagation of the field and a term proportional to the third order nonlinearity $\chi^{(3)}$ as well as the fundamental intensity I_{fund} .

The phase shift depends on the squared amplitude of the fundamental field $I_{\text{fund}} = |\alpha_{\text{fund}}|^2$. However, the quadrature squeezing only arises due to the vacuum noise of the electromagnetic field. The non-vanishing variance of the amplitude quadrature can be seen as a fluctuation of the field amplitude. One can deduce a high phase shift for an increased amplitude and a lower phase shift for a decreased amplitude from equation 2.49. A coherent quantum state with a large amplitude α_{fund} will be transformed to an amplitude squeezed state under the influence of a Kerr nonlinear phase shift. The effect is illustrated in a phasor picture in Fig. 2.3.

Unfortunately, the third order nonlinearities of $\chi^{(3)} \propto 10^{-15} \text{m/V}$ are extremely low and thus require high pump powers not feasible for continuous-wave experiments. An alternative is the cascaded Kerr effect which mimics the optical Kerr effect through a cascading second harmonic generation process [46]. It utilizes the derivation of the

2. Theory

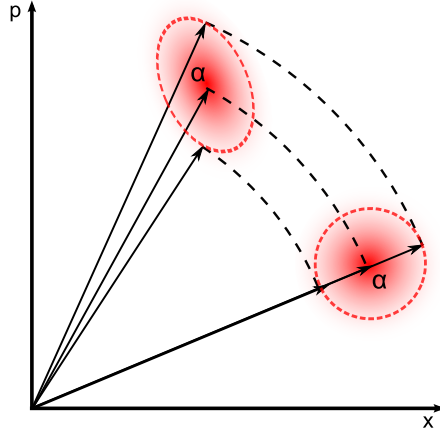


Figure 2.3.: Phasor picture illustration of the intensity dependent phase shift leading to Kerr squeezing. The vacuum noise on the initial coherent state with amplitude α (right circle) is composed of different coherent amplitudes as depicted via arrows of different lengths. The higher amplitudes receive a higher phase shift due to the Kerr effect. The resulting ellipse on the left is a squeezed state again having a coherent amplitude of α .

field equations for second harmonic generation (see [47]) to achieve an intensity dependent phase shift of

$$\phi(z) \propto \phi_0(z) + \frac{\Delta k z}{8 + \frac{(\Delta k)^2}{\chi' I_{\text{fund}}}} \cdot \left[1 - \text{sinc} \left(z \cdot \sqrt{\left(\frac{\Delta k}{2} \right)^2 + 2\chi' I_{\text{fund}}} \right) \right]. \quad (2.50)$$

Here, χ' is a factor proportional to the second order nonlinearity $\chi^{(2)}$ and Δk is the phase mismatch of the wave vectors for fundamental and harmonic wave. The last term in the equation disappears for a maximum second harmonic conversion efficiency at $\Delta k = 0$. On the other hand, the equation will transform to equation 2.49 at the first minimum for second harmonic conversion when $\Delta k \approx \frac{2\pi}{z}$. This means that a second harmonic generator at the first conversion minimum has formally the same effect as the intensity dependent phase shift by the optical Kerr effect. However, the intensity dependent phase shift will vanish at maximum conversion efficiency as explained before.

An intuitive explanation is that the fundamental field will convert to the second harmonic at the first half of the medium and will be back-converted to its fundamental at the second half. Both fields will

however experience a differential phase shift from the different refractive indices. The total phase shift for the output field consists of the combined phase shift for fundamental and harmonic light. Again, the vacuum fluctuations of the amplitude will lead to a fluctuating second harmonic conversion efficiency and thus affect the weighting of both parts. Effectively, this is equivalent to the optical Kerr effect induced intensity dependent phase shift.

The Kerr interaction Hamiltonian highlights another interesting property. It reads

$$\hat{H}_{int} = \hbar\kappa\hat{a}^{\dagger 2}\hat{a}^2 = \hbar\kappa\hat{n}(\hat{n} - 1) \quad (2.51)$$

with $\kappa \propto \chi^{(3)}$ and \hat{n} being the photon number operator. This is a Hamiltonian quartic in \hat{a} rather than quadratic as for optical parametric amplification and other second order nonlinear effects. In principle, the Kerr interaction creates a photon number squeezed state with sub-Poissonian statistics contrary to the ordinary quadrature squeezed state. It is more similar to a non-gaussian Fock state than to a quadrature eigenstate. In the phasor picture the coherent state turns into a “banana-shaped” state rather than a squeezing ellipse. The small nonlinearity in typical media will produce a “banana” with a radius of curvature far larger than the length of the ellipse. The effect is negligible in this case. Therefore, a very high nonlinear interaction is necessary to observe the non-gaussian behavior of states generated via the (cascaded) Kerr effect. This has not yet been experimentally realized.

3

Chapter 3.

High conversion efficiency second harmonic generation

3.1. Introduction

A second harmonic generation cavity (SHG) is an important tool in a variety of quantum optics experiments. It is necessary to provide the pump field for squeezed light generation via parametric down conversion (PDC). High pump powers are important in the generation of feasible squeezing strengths in high-bandwidth squeezed light sources due to energy conservation [45]. There are other experiments which profit from high conversion efficiency frequency conversion. In laser interferometric gravitational wave detectors, frequency up-converted light with a high efficiency is a promising method for improving the detector sensitivities [48, 49]. Furthermore, the frequency conversion of quantum states of light requires highly efficient nonlinear processes, e.g. second harmonic generation, to avoid decoherence [50, 51].

In this chapter, I report on the implementation of second harmonic generation of 1550 nm continuous-wave laser light with a very high efficiency close to unity. The experiment used a standing wave cavity consisting of a high-reflective coated periodically poled potassium titanyl phosphate crystal (PPKTP) as nonlinear medium and an external mirror. We measured the conversion efficiency via pump depletion of the fundamental field at 1550 nm with a photodetector. The relative pump depletion yielded a small error for the conversion efficiency, while a power meter was used to verify the measurement. The SHG was built as an essential component for high-bandwidth squeezed light sources in future experiments.

3. High conversion efficiency second harmonic generation

First, I will briefly discuss the theoretically limiting factors in cavity based second harmonic generation of laser light. The experimental setup and the SHG cavity design will then be described. Afterwards, the conversion efficiency measurement concept via pump depletion will be explained and I will present the measurement results. The chapter will conclude by investigating the limiting factors of the measured conversion and I will give a brief summary of the experiment.

This experiment was realized in collaboration with A. Schönbeck and R. Moghadas Nia as part of their Bachelor theses. The results were published in [52] and large parts of the following text, as well as some pictures, are taken from this paper.

3.1.1. Limitations for second harmonic generation

Theoretically, a frequency conversion efficiency of up to 100 % is possible in lossless nonlinear optical materials. In practice, the conversion is limited because of the material's finite effective nonlinearity, $\chi_{\text{eff}}^{(2)}$, the available optical pump power and in particular due to optical loss. A lack of pump power or nonlinearity can be partially compensated by using an optical resonator for the fundamental field with an appropriate intra-cavity waist size [53]. The resonant enhancement of the fundamental field will increase the interaction strength and lead to a higher conversion efficiency [47].

In cavity-based second harmonic generation, the round-trip loss inside the resonator has to be minimized in order to achieve high conversion efficiencies. This requires high quality mirrors with low scattering and absorption, anti-reflective coatings with the lowest possible reflectivity and nonlinear crystals with low absorption as well as scattering. The round-trip loss directly reduces the conversion efficiency, but also limits the cavity finesse and the possible resonant field enhancement. Furthermore, a high crystal absorption leads to heating, thermal lensing and a deformation of the cavity mode, which limits the conversion efficiency [54].

Therefore, a conversion efficiency close to unity is possible by designing a nonlinear crystal cavity with low round-trip loss and a finesse optimized for the available pump power.

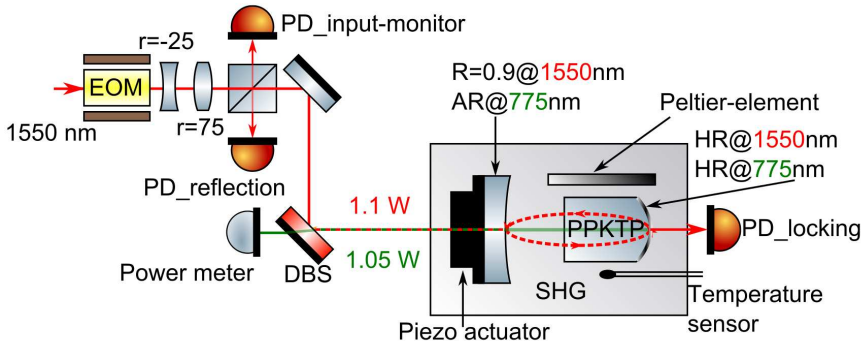


Figure 3.1.: Schematic of the experimental setup for the high-conversion efficiency second harmonic generation. SHG: second harmonic generation with nonlinear PPKTP crystal, DBS: dichroic beam splitter to separate 775 nm and 1550 nm light, PD_input-monitor: photodetector monitoring power fluctuations of the 1550 nm pump field, PD_reflection: photodetector for relative measurement of the conversion efficiency via pump depletion, PD_locking: photodetector for the cavity length stabilization, EOM: electro-optic modulator producing sidebands of 138 MHz for the cavity length stabilization. [52]

3.2. Experimental setup

The experimental setup is depicted in Fig. 3.1. An erbium-doped fiber laser type *Scorpio* by *NP Photonics* with 1.3 W output power at 1550 nm in a class 1000 clean room environment was used.

A three mirror ring resonator with high impedance matching spatially filtered the beam. This mode cleaning cavity (MC) also suppressed amplitude and phase noise above its linewidth of about 2.4 MHz. A homemade electro-optic modulator (EOM) phase modulated the 1550 nm light with 124 MHz to generate a Pound-Drever-Hall error signal (PDH) for the cavity's length stabilization. We achieved a mode-matching of 98% to the MC (see Fig. 3.2) and optimized the control electronics to a unity-gain frequency of 6 kHz.

After transmission through the MC, about 1.1 W laser light was mode-matched into the SHG. We phase modulated the light field with 138 MHz using another EOM in the beam path. This generated a PDH error signal for the stabilization of the second harmonic generation cavity (see Fig. 3.3). A resonant photodetector in transmission of the SHG served as the sensor for the cavity length stabilization. A gain-optimized servo controller with respect to the SHG's transfer function achieved a unity-gain frequency of 4 kHz (appendix Fig. A.1).

3. High conversion efficiency second harmonic generation

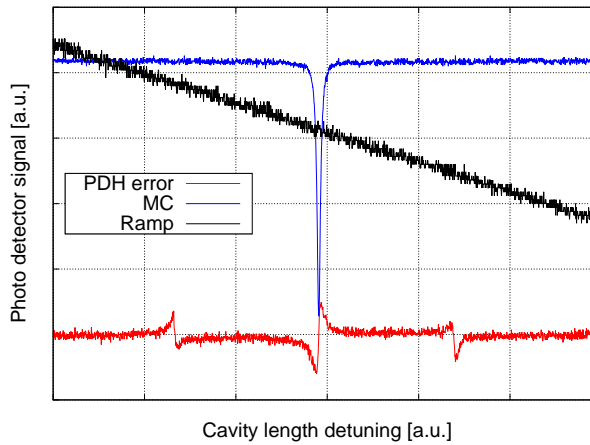


Figure 3.2.: Photodetector signal in reflection of the modecleaner cavity measuring the mode-matching. The cavity's fundamental resonance (blue) and the Pound-Drever-Hall error signal (red) are detected by continuously shifting the cavity length with a ramp signal (black). The mode-matching was estimated to be better than 98 %.

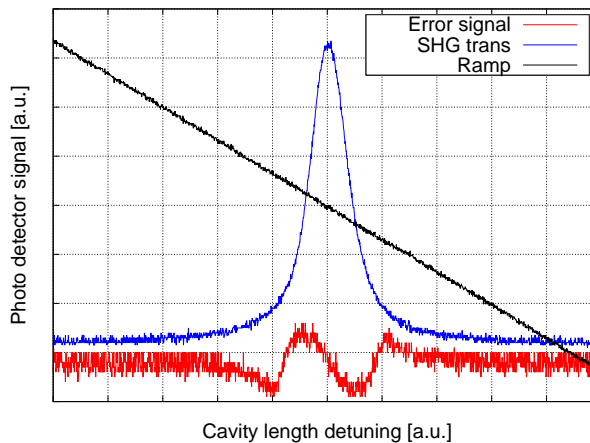


Figure 3.3.: Photodetector signal in transmission of the second harmonic generation cavity measuring the mode-matching for the fundamental resonance (blue) and the modulation/demodulation error signal (red). The cavity length was continuously shifted with a ramp signal applied to a piezo-actuated mirror (black). The fundamental power at 1550 nm entering the SHG was about 1 W.

In order to monitor power drifts, a part of the 1550 nm laser was reflected off an anti-reflective coated substrate and was detected on photodetector *PD_input-monitor* before entering the SHG. The measured power drifts were below 1 % and could be neglected for the conversion efficiency measurement. A fraction of the SHG's reflected light at 1550 nm was measured by *PD_reflection*. This pick-off was used for the conversion efficiency measurement by monitoring the pump depletion of the fundamental field.

A dichroic beam splitter (DBS) with $R_{1550} > 99.98\%$ and $R_{775} = 0.7\%$ separated the fundamental and harmonic field directly in front of the SHG. The frequency doubled field was detected by a power meter in transmission of the DBS to validate the conversion efficiency measurements and measure the temperature dependent conversion.

3.2.1. Hemilithic SHG cavity

The SHG resonator consisted of a custom-made housing for the PPKTP crystal and one external cavity incoupling mirror. The coated end surface of the crystal and the external mirror formed the cavity. An aluminum plate held the external mirror and was screwed to the housing of the nonlinear crystal. This quasi-monolithic (hemilithic) cavity design ensured a very stable frequency doubling operation.

The PPKTP crystal [55] was plano-convex with dimensions of $1 \times 2 \times 9.3 \text{ mm}^3$ and one curved surface with a radius of curvature of 12 mm. This surface was dielectrically coated yielding a reflectivity of about 99.95 % at the wavelengths of 1550 nm and 775 nm. The crystal's plane surface was anti-reflective coated ($R < 0.05\%$) for both wavelengths to achieve low intra-cavity loss. We measured the PPKTP absorption to be $\alpha_{1550} = (0.0084 \pm 0.004) \text{ ppm/cm}$ and $\alpha_{775} = (0.0127 \pm 0.0026) \text{ ppm/cm}$ for the fundamental and the harmonic wavelength [56].

An external cavity mirror with 25 mm radius of curvature and with reflectivities of $R_{1550} = 90.0 \pm 1.5\%$ and $R_{775} < 0.2\%$ served as the incoupling mirror for the SHG cavity. The mirror's distance from the plane crystal surface was about 24 mm, resulting in a cavity waist size of $w_0 = 37.6 \text{ }\mu\text{m}$ for 1550 nm. It was attached to a piezo-electric transducer to scan and stabilize the resonator length.

We measured the mode-matching of the TEM_{00} mode into the SHG cavity to be about 98 % (see Fig. 3.4). This value sets an upper limit for our conversion efficiency. The plot shows a cavity length scan over one free spectral range of the SHG resonator. Some very small

3. High conversion efficiency second harmonic generation

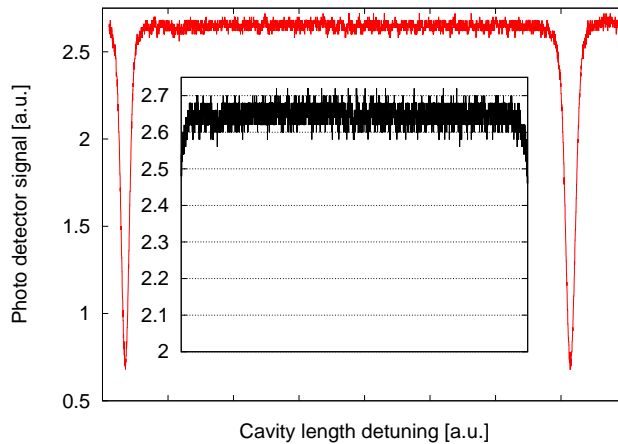


Figure 3.4.: Mode-matching for the SHG cavity measured in reflection. The cavity length was shifted via a piezo actuated mirror over a full free spectral range (red). The area between the fundamental modes is magnified to show the low higher-order mode content (grey). The fundamental power at 1550 nm entering the SHG was 25 mW, which yielded a mode-matching of about 98 %.

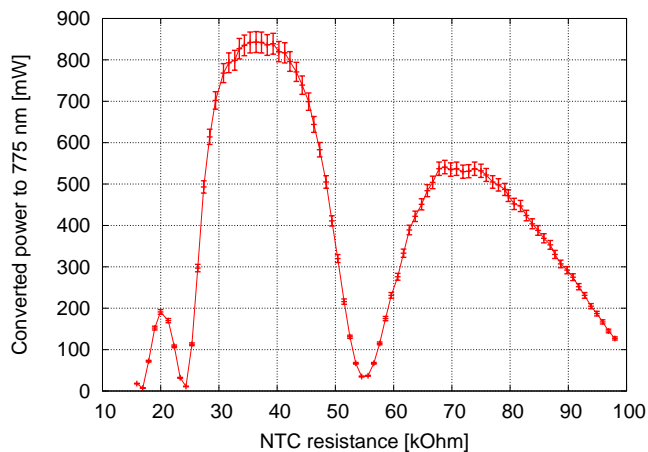


Figure 3.5.: SHG quasi-sinc-function showing the temperature dependent conversion efficiency. The cavity was pumped with 1050 mW fundamental light. The converted light at 775 nm was detected by a power meter. We varied the crystal temperature using a Peltier-element and stabilized the cavity on resonance for the conversion measurement. A maximum conversion efficiency was present at around 37 kOhm, which corresponds to around 45 °C. The power meter measurement error was specified to be 3%. The strong asymmetrical form in comparison to a sinc-function is induced by the different penetration depths of the fundamental and the harmonic field in the crystal's HR coating.

3.3. Pump depletion measurement concept

higher-order modes are faintly visible in the mode spectrum, but almost vanish in the photodetector's dark noise.

A Peltier-element driven by a custom temperature controller stabilized the crystal temperature for ideal quasi-phase-matching. The temperature was found to be around 45 °C by measuring the quasi-sinc-function of the second harmonic generation process (see Fig. 3.5). Note that the cavity was not optimally mode-matched for this measurement and thus did not yield the maximally achievable conversion efficiency.

3.3. Pump depletion measurement concept

A pump depletion measurement is a feasible technique in the determination of the conversion efficiency of a second harmonic generation cavity [57]. The pump depletion here means that the 1550 nm fundamental light is entering the SHG cavity, converts to 775 nm and will thus not be detected anymore. However, the pump depletion is only a good measure for the SHG process if the cavity exhibits low absorption, low scattering loss and is far away from impedance matching. All three effects mimic the effect of pump depletion and would eventually deteriorate the measurement result.

The absorption as well as the overall intra-cavity loss were very small (see section 3.2.1) and were assumed to be negligible in our experiment.

The impedance matching was the most critical part and had to be examined carefully. If a cavity is impedance matched, its reflected field intensity on resonance is zero. This effect, however, is indistinguishable from pump depletion, which will lead to a measurement error for the conversion efficiency. An over-coupled or under-coupled cavity will reflect most of the light and is thus best suited for the pump depletion measurement.

We performed the pump depletion measurement by detecting the 1550 nm light in reflection of the cavity using photodiode PD_reflection. The SHG cavity in our experiment was highly over-coupled and reflected about 99.15 % of the incoming light on resonance. Note that this was just the case for no SHG conversion. For an increasing conversion the over-coupling of the cavity was reduced because the conversion is identical to loss for the intra-cavity field. This means that a higher fraction of the remaining intra-cavity field was transmitted at high conversion compared to zero conversion. We could quantify this

3. High conversion efficiency second harmonic generation

effect by simulating the change of the cavity impedance matching via the *Nonlinear cavity simulator* by Nico Lastzka (N.L.C.S. see [58, 59]). It changed from 0.85 % transmission at zero conversion to $> 5.7\%$ transmission at 95 % conversion. This means 5.7 % of the remaining 5 % fundamental field in the cavity is transmitted, thus yielding an error of $0.057 \cdot 0.05 = 0.0029$. We verified this quantitatively with a power meter by measuring the less pronounced reduction of the faint light transmitted through the cavity. This error was taken into account in the final measurement results for the conversion efficiency. The major advantage of the pump depletion measurement is the small absolute error compared with a calibration error of a power meter. The pump depletion as carried out with a photodiode is a relative measurement of the fundamental pump field and is not relying on absolute values.

3.4. Experimental results

The measurements for the conversion efficiency were carried out by the pump depletion method as well as a commercially available power meter. The pump depletion was measured in reflection of the SHG and detected the relative depletion of the 1550 nm light, while the power meter directly compared the power at 1550 nm in front of the SHG with the converted 775 nm light in reflection.

3.4.1. High-conversion pump depletion measurement

We performed a conversion efficiency measurement for a fundamental input power of 1.1 W by detecting the pump depletion in reflection of the SHG cavity (see Fig. 3.6).

For a cavity operated off-resonance the fundamental input field did not enter the cavity and hence gave a 0 % conversion efficiency reference on our photodetector PD_reflection (orange). A reference for maximum conversion (100 %) was measured by blocking all light in front of the photodiode (black). When the cavity length was tuned on resonance, the fundamental field entered the SHG and a large fraction was converted to its harmonic. This appeared as loss on the detected signal. Figure 3.6 shows the pump depletion for a swept cavity length (blue) and for a cavity length controlled on maximum conversion (green). This yielded a total conversion efficiency of

$$(95 \pm 0.81) \%$$

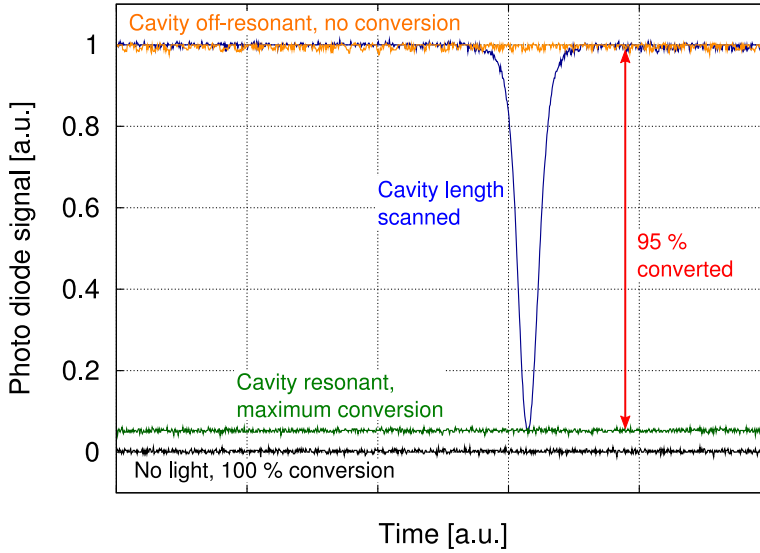


Figure 3.6.: Depletion measurement for a fundamental input power of 1.1 W. Bottom trace (black): no light on PD_reflection refers to 100 % conversion. Top trace (orange): SHG cavity off-resonant refers to 0 % conversion. Trace at about 0.05 (green): SHG cavity is stabilized on maximum conversion. Peaked curve (blue): Scan of the cavity length over the resonance peak of the TEM₀₀ mode. The conversion efficiency is deduced to be 95 ± 0.81 % from this measurement. The error of 0.81 % was estimated in section 3.4.2 and included a total loss calculation. [52]

measured via pump depletion. The contributions leading to the error of 0.81 % are presented in the next section.

3.4.2. Estimated error for the pump depletion

The error was estimated to consist of the following contributions: the measurement statistics; the non-perfect anti-reflection coating of the crystal, the uncertainties on the absorption as well as the unknown contribution of scattering losses inside the crystal and the related changes of the cavity over-coupling. The photodetector nonlinearity was estimated to contribute an error of ~ 0.1 % over the dynamic range used. Additionally, the AR coating (AR = 0.05 %) of the crystal surface inside the cavity created round-trip losses leading to an error of ~ 0.32 %. The error of the measured crystal absorption for the fundamental and harmonic field, as well as intra-cavity scattering

3. High conversion efficiency second harmonic generation

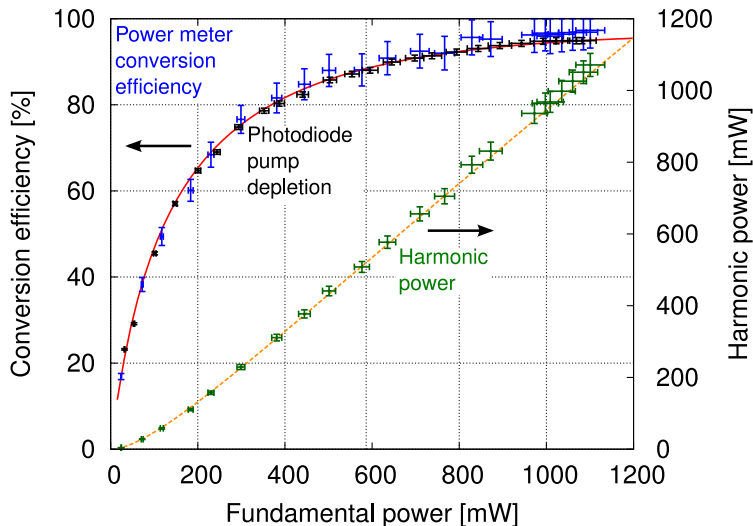


Figure 3.7.: Conversion efficiency and harmonic power (775 nm) versus fundamental input power (1550 nm). Data with small error bars (black): pump depletion measurements. Data with large error bars (blue and green): absolute power measurements at both wavelengths. The dotted orange line and the solid red line show the full simulation of our system using N.L.C.S. based on independently determined parameters and a fitted crystal nonlinearity of 7.3 pm/V. [52]

losses, were estimated to be $< 0.1\%$ in total. The change of impedance matching due to high conversion in the cavity finally introduced an error of $\sim 0.29\%$ (see section 3.3).

The total error therefore was 0.81% for the measurement of the relative pump depletion.

3.4.3. Conversion versus pump power

We measured a pump power dependent conversion efficiency with the pump depletion method as well as with a power meter (see Fig. 3.7). The data points with small error bars (black) represent the pump depletion measurements detected by PD_reflection. In order to make an experimental consistency check we performed a second measurement using a commercial power meter (*Ophir Optronics*) with a thermal measuring head (blue). This data is indeed consistent, although it has considerably larger error bars of about 6%. This error consists of the specified calibration error for the power meter of about 3% and

has to be taken into account twice, since the conversion efficiency is measured by comparing the 1550 nm with the 775 nm light.

The data is in good agreement with the result from our numerical time-domain simulation by N.L.C.S. (solid red line) setting the effective nonlinearity of our crystal to a value of $\chi_{\text{eff}}^{(2)} = 7.3 \text{ pm/V}$.

The limitations for the conversion efficiency of the SHG cavity were the mode-matching of around 98 % and the limited available pump power of about 1.15 W of 1550 nm light.

3.5. Summary & Outlook

This chapter reports on the observation of second harmonic generation of continuous wave laser light with a conversion efficiency of $(95 \pm 0.81)\%$ measured via optical pump depletion. The experiment used a PPKTP crystal in a standing wave cavity and a wavelength of 1550 nm. To the best of our knowledge, we report the highest external cw second harmonic conversion efficiency observed so far.

The hemilithic second harmonic generation resonator converted a fundamental field of 1.10 W to 1.05 W at 775 nm. Based on independent measurements, we estimate the crystal absorption and other optical losses. The two highest error contributions to the measured conversion efficiency were the intra-cavity round trip loss of about 0.32 % and the change in cavity impedance matching yielding an error of 0.29 %. The results were consistent with independent but less accurate measurements with a calibrated power meter. We found very good agreement with a numerical time-domain simulation by N.L.C.S. of our experiment.

The simulation indicated that our conversion efficiency was limited by the non-perfect mode-matching and by the non-perfect cavity impedance matching for the maximum input power available. At a pump power of 1.3 W, a maximum conversion of about 98 % should be reached for the given cavity design. An improvement in mode-matching would even lead to higher conversion efficiencies up to 99 %. The conversion efficiency is ultimately only limited by the intra-cavity loss and the changing cavity impedance matching. The experiment demonstrated that a custom-designed SHG cavity is able to produce frequency doubled light with nearly 100 % efficiency at any given input power. The key features are very low absorption crystals and high quality coatings on the crystal surfaces as well as on the mirrors. Future experiments are likely to focus on highly efficient second har-

3. High conversion efficiency second harmonic generation

monic generation at different wavelengths, for example the ultra-violet regime.

This experiment set a new benchmark in developing second harmonic generation resonators with an optimized efficiency. The realization of an SHG efficiency close to unity will greatly enhance frequency up-conversion of nonclassical states of light, such as single photon states and squeezed states of light [60, 61].

4

Chapter 4.

Squeezed light source without squeezing resonator

4.1. Introduction

Quantum key distribution via two-mode squeezed states of light has the potential to become one of the standard data encryption systems in the near future. Recently, this technique was applied to generate a secure key of 1.5 MB via measuring 10^8 samples in a table top experiment [34]. This experiment investigated the use of fiber based key distribution at a wavelength of 1550 nm for the squeezed light. The telecommunication wavelength of 1550 nm has the advantage of low loss in optical fibers [37, 38], which is particularly important for squeezed states.

A further development will be to experimentally enhance the secret key rate for potential applications in the future. It can either be improved by measuring a higher squeezing strength or by increasing the detection speed. Since even low optical loss will in practice limit the squeezing strength to a finite value (≈ 10 dB), the detection speed is a more feasible approach to enhance the data rate. Here the detection speed means the recording of more samples per second, which is ultimately only limited by the bandwidth of the squeezing resonator. Besides, the squeezing bandwidth is unaffected by optical decoherence in fibers in contrast to the squeezing strength. Modern telecommunication fibers introduce an optical loss of 0.2 dB per kilometer, which will strongly decrease the squeezing strength over distance. The bandwidth however will be independent of the transmission distance. An improvement in squeezing bandwidth thus promises to be a more ro-

4. Squeezed light source without squeezing resonator

bust approach to enhance the QKD data rate. For further information see chapter 1.

The following experiment was designed to generate a squeezed field with a white squeezing spectrum up to GHz frequencies. The experimental setup used parametric down-conversion via a PPKTP crystal in an optical resonator. However, the optical parametric amplifier (OPA) did not contain any resonant enhancement for the fundamental wavelength, which should in principle generate squeezed light over the full phase-matching bandwidth of several nanometers. The consequences are a very high pump threshold for parametric oscillation and small achievable squeezing factors. We partially compensated the absence of the resonator at the fundamental wavelength by resonantly enhancing the pump light instead.

I will first describe the design of the OPA used in the experiment. This will be followed by an overview of the experimental setup used to generate GHz bandwidth squeezing with a hemilithic cavity. Then I will analyze the cavity mode-matchings and characterize the homodyne detector. I will present the squeezing measurements and explain the optical detection loss. In the end, I will give a short summary of the experimental results as well as an outlook for improving the experiment.

The chapter is based on our publication in the journal Optics Letters (see [62]).

4.2. Design concept of the hemilithic high bandwidth squeezing source

There are two possible approaches for achieving high squeezing bandwidths with cavity assisted optical parametric amplification. Either broaden the cavity linewidth by lowering the mirror reflectivities for the fundamental wavelength, or increase the cavity's free spectral range by shortening its optical length. This experiment was designed via the first approach and used no resonant enhancement for the fundamental squeezed field. The squeezing bandwidth should thus only be limited by the phase matching bandwidth of the nonlinear crystal. The squeezed light source used a PPKTP crystal with the dimensions $1 \times 2 \times 9.3 \text{ mm}^3$ and a quasi phase-matching temperature of about 46°C . Its one end surface had a radius of curvature of $\text{RoC} = 12 \text{ mm}$ and a highly reflective coating ($\text{HR} = 99.95\%$) for the fundamental

as well as for the harmonic wavelength. The crystal's other surface was planar and anti-reflective coated ($AR < 0.1\%$) to minimize intracavity loss. We measured the crystal absorption in reference [56] to be $\alpha_{1550} = 84 \pm 40$ ppm/cm and $\alpha_{775} = 127 \pm 26$ ppm/cm for the fundamental and harmonic wavelengths, respectively. The crystal had a refractive index of $n_{1550} = 1.816$ and an effective non-linearity of about $d_{\text{eff}} = 7.3$ pm/V.

A curved mirror ($\text{RoC} = 25$ mm) with reflectivities $R_{1550} < 1\%$ and $R_{775} = 98.5\%$ was placed 24 mm in front of the crystal, leading to a free spectral range of 3.67 GHz and a waist size of $w_{0,1550} = 37.6$ μm for the squeezed field. The crystal's end surface and the external mirror formed the linear cavity with a finesse of about $\mathcal{F}_{775} = 350$ for the harmonic pump field. The waist size for the pump field at 775 nm was $w_{0,775} = 27$ μm . Our simulation suggests that pump powers as high as 2.18 kW were necessary to reach the optical parametric oscillation threshold and thus maximum squeezing. The high cavity finesse for the harmonic field enhanced the pump power by roughly a factor of 248. This compensated for the non-existing squeezing enhancement of the resonator.

4.3. Experimental setup

In the experimental setup (see Fig. 4.1) we used 1550 nm of continuous-wave laser light with around 1.3 W of output power from an erbium-doped fiber laser. First, the laser light was transmitted through a three mirror ring resonator for spatial mode cleaning. 1.1 W were then phase modulated with 138 MHz by a custom made EOM and mode-matched into a second harmonic generation cavity containing a PPKTP crystal. We used the SHG cavity described in [52], which converted up to 95% of the 1550 nm laser light into 775 nm pump light for the OPA.

A dichroic beam splitter in front of the SHG separated the fundamental and the harmonic field. The pump light of about 300 mW was again transmitted through another DBS and was mode-matched to the hemilithic OPA. We stabilized the cavity length with the pump field by using a Pound-Drever-Hall (PDH) scheme. Here the phase modulation of 138 MHz applied before the SHG was down-converted and used to generate the error signal for the PDH stabilization. A resonant photodetector with built in mixer demodulated the sideband in reflection of the OPA and acted as sensor for the cavity length sta-

4. Squeezed light source without squeezing resonator

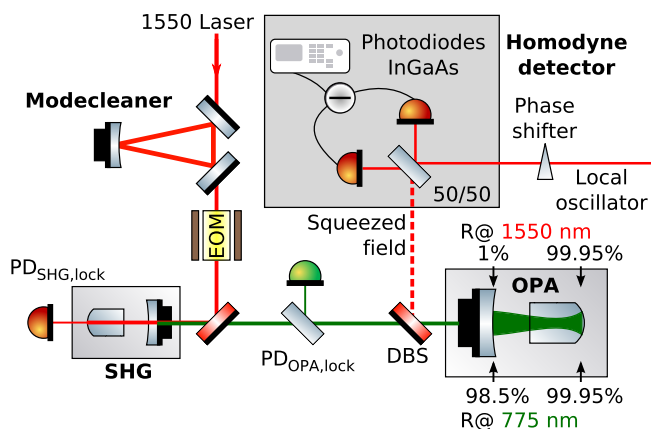


Figure 4.1.: Schematic of the experimental setup for the squeezed light source without squeezing resonator. Modecleaner: three mirror spatial filter cavity; SHG: second harmonic generation cavity with nonlinear PPKTP crystal; OPA: squeezed light source with nonlinear PPKTP crystal and high squeezing bandwidth; Phase shifter: piezo-actuated mirror tuning the homodyne readout phase; DBS: dichroic beam splitter to separate 775 nm and 1550 nm light; PD_{SHG/OPA,lock}: photodetector measuring error signals for cavity length stabilization with 138 MHz demodulation frequency; EOM: electro-optic modulator producing sidebands of 138 MHz for the cavity length stabilization. [62]

bilization.

The DBS in front of the OPA separated the pump field from the generated squeezed vacuum, which was superimposed with a bright local oscillator on the homodyne detection beam splitter. A piezo-actuated mirror in the local oscillator beam path was used to shift the phase of the respective fields and thus change the measurement between squeezing and anti-squeezing. The homodyne detection visibility was adjusted with an auxiliary control field at 1550 nm.

4.3.1. Hemilithic cavity mode-matching

We mode-matched the control field at 1550 nm as well as the pump field at 775 nm to the hemilithic OPA. Both fields entered the cavity through the input coupling mirror with $R_{1550} < 1\%$ and $R_{775} = 98.5\%$, respectively.

The mode-matching of the pump field was measured with a photodetector in reflection of the OPA yielding a value of about 80% (see Fig. 4.2). A Pound-Drever-Hall error signal for the pump field was detected with the same photodiode and was used to stabilize the cavity

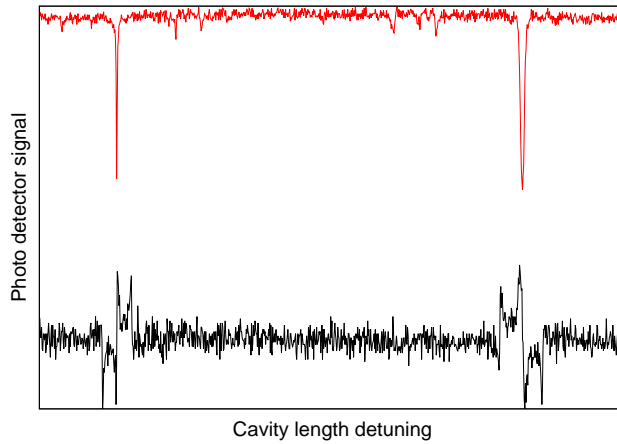


Figure 4.2.: Mode-matching of the pump field at 775 nm (red) with the Pound-Drever-Hall error signal for the cavity length stabilization (black) measured in reflection of the OPA. The PPKTP crystal's absorption induced a photo thermal self-phase modulation to the resonance peaks at 270 mW pump power. This results in a broadening of the right peak shape (lengthening cavity) and a narrowing of the left peak shape (shortening cavity). The mode-matching was estimated to be around 80 %.

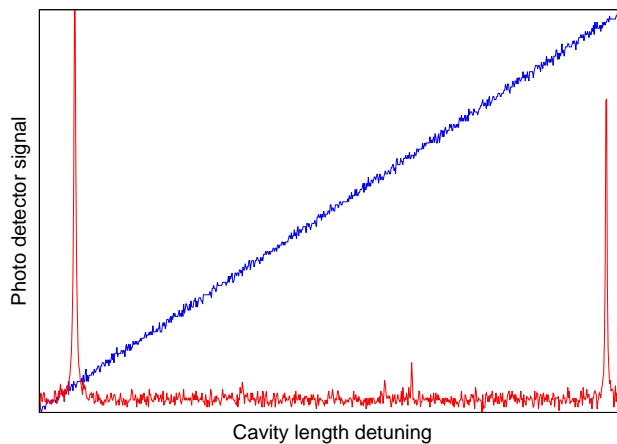


Figure 4.3.: Mode-matching for the frequency doubled 1550 nm control field to the hemilithic OPA. Red: length scan over one cavity FSR; Blue: ramp signal applied to the piezo actuated mirror. Two higher order transversal modes appear in the spectrum and limit the mode-matching to about 88 %. The peak height difference of the TEM₀₀ modes is caused by the resonant enhancement of the fundamental 1550 nm field due to the small cavity finesse for 1550 nm.

4. Squeezed light source without squeezing resonator

on resonance for the 775 nm harmonic field. The measurement used 270 mW of pump power, thus showing an absorption induced photo-thermal self-phase modulation of the resonance peaks.

The control field was only used to serve as a reference for the homodyne detection visibility adjustment and was later blocked during the squeezed light measurement. The low reflectivity for 1550 nm of the input mirror with $R_{1550} < 1\%$ did not allow for a normal mode-matching procedure. In fact, there were no resonance peaks visible due to the very low finesse of the cavity at 1550 nm. Therefore, we injected the control field into the cavity and detected its frequency doubled field at 775 nm with a photodetector in transmission. By adjusting the control field for mode-matching, the 775 nm resonance peak reached a TEM₀₀ mode content of about 88%.

4.4. Experimental results

In a first step we characterized the self-made homodyne detector with GHz bandwidth photodiodes by investigating the detector's linearity as well as the dark-noise clearance for a spectrum from 5 MHz to 2 GHz. Afterwards the homodyne detection visibility was measured and we performed squeezed vacuum measurements as well as a characterization of the optical loss in the experiment.

4.4.1. Homodyne detector characterization

Our balanced homodyne detector (BHD) consisted of two FCI-H250G-InGaAs-70 (*OSI Optoelectronics*) photodetectors with build-in transimpedance amplifiers, which were able to measure with a bandwidth of up to 2 GHz. A subtraction of the measured signals was achieved via commercially available power splitters within a frequency range of 50 MHz to 1 GHz and of 1 GHz to 2 GHz, respectively. The detector's dark-noise clearance from the shot-noise level at 0.75 mW local oscillator power was about 8 dB over a frequency range of several hundred MHz, slowly degrading to 2 dB towards 2 GHz (see Fig. 4.4).

The dark noise was measured with all BHD inputs blocked. The shot noise level was measured with only the signal input blocked. Several electronic pick-up peaks showed up in the homodyne detector's dark noise and the shot noise. There are modulation peaks from the PDH locking frequencies at 101 MHz and 138 MHz, as well as their harmonics. The peaks between 1 GHz and 2 GHz can be seen in the detector

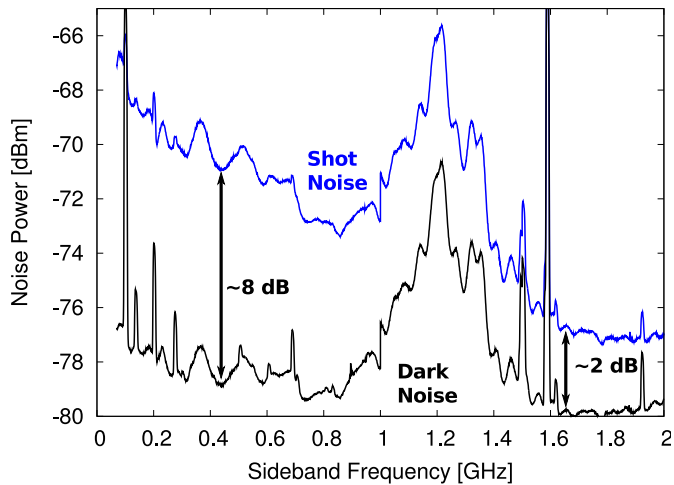


Figure 4.4.: Balanced homodyne detector characterization from 50 MHz to 2 GHz using the FCI-H250G-InGaAs-70 photodiodes. Top: Homodyne detector shot noise at 0.75 mW local oscillator power. Bottom: Homodyne detector dark noise. The dark-noise clearance ranges from about 9 dB at 50 MHz, 8 dB at 500 MHz, and slowly degrades to about 2 dB at 2 GHz. [62]

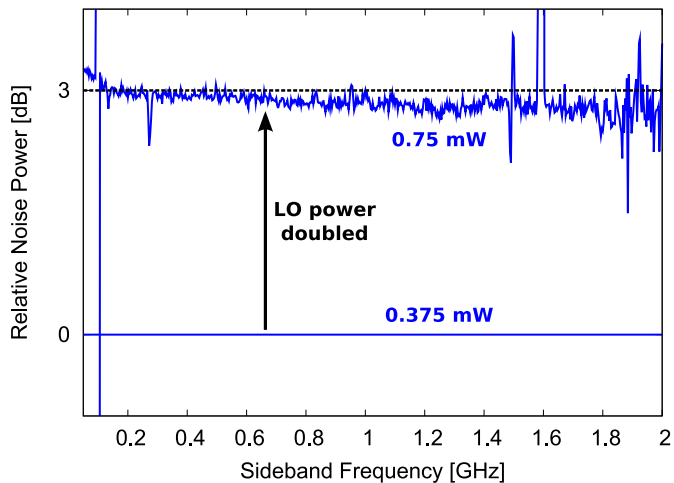


Figure 4.5.: Characterization of the homodyne detector's linearity. Measured shot noise levels at 0.75 mW (top) and 0.375 mW (bottom) local oscillator powers, both are dark-noise corrected and normalized to the data of the latter. At these LO power levels the homodyne detector is linear since doubling the LO power results in a 3 dB increase of the shot noise. A small saturation effect is revealed towards higher frequencies. [62]

4. Squeezed light source without squeezing resonator

dark noise and correspond to external electronic pick up noise. The broad peak structure around 1.2 GHz is due to a parasitic resonance in the electronic circuit of the detector.

The homodyne detector spectrum was linear at a local oscillator power of up to 0.75 mW (Fig. 4.5). Saturation effects start to appear above 0.7 GHz as the curve is slightly lower than 3 dB. This effect degraded the measured squeezing strength, but only by negligible amounts.

4.4.2. Squeezed light measurement

The visibility for the homodyne detector was measured by overlapping the control field and the local oscillator field with equal powers on the homodyne beam splitter, while continuously shifting the local oscillator's phase with a piezo-actuated mirror. The sinusoidal interference contrast was detected by a photodiode (see Fig. 4.6). The visibility at the homodyne detector was measured to be $\eta_{\text{vis}} = 88\%$ using the formula

$$\eta_{\text{vis}} = \frac{I_{\text{max}} - I_{\text{min}}}{I_{\text{max}} + I_{\text{min}}},$$

where $I_{\text{max}} = 1.0$ is the maximum of the photodiodes sinusoidal signal, while $I_{\text{min}} = 0.064$ is the minimum of the photodiodes sinusoidal signal.

After characterizing the homodyne detection visibility, we performed a squeezed vacuum measurement. The result was a dark-noise corrected squeezing level of up to 0.3 dB and anti-squeezing of up to 0.5 dB from 50 MHz to 2 GHz using a harmonic pump power of about 250 mW and a LO power of 0.75 mW (see Fig. 4.7). The squeezing spectrum is indeed almost white over the whole frequency range. It was only slightly degraded at high frequencies due to the finite cavity linewidth and possibly due to the poor dark-noise clearance at high frequencies. The peaks in the normalized spectrum also arise in the detector's dark noise and can be associated with electronic pick-up noise.

The squeezing strength is mainly limited by insufficient pump power far below the parametric oscillation threshold. We simulated the threshold for optical parametric oscillation using N.L.C.S. to be 8.8 W of external pump power, which is about 2.18 kW of intra-cavity power for the OPA's parameters. The maximally available pump power of 62 W intra-cavity was still far below the threshold, thus limiting the achievable squeezing. We measured a parametric gain of about 1.62 at 250 mW harmonic pump power, which corresponds to a squeezing

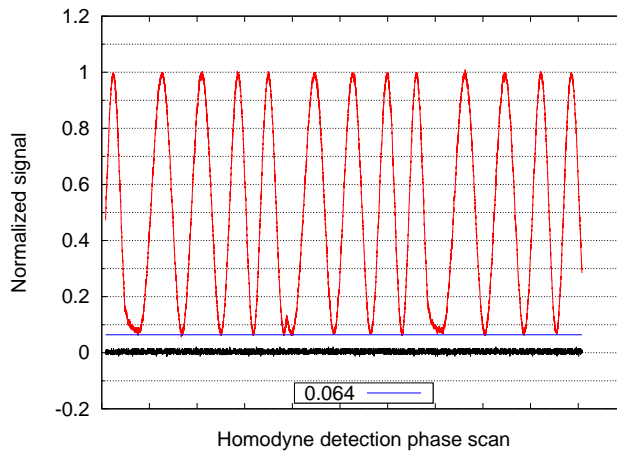


Figure 4.6.: Measured visibility of the homodyne detector with a local oscillator and signal power of 0.75 mW each. The local oscillator was continuously phase shifted using a piezo-actuated mirror. The measurement indicates a homodyne visibility of 88%.

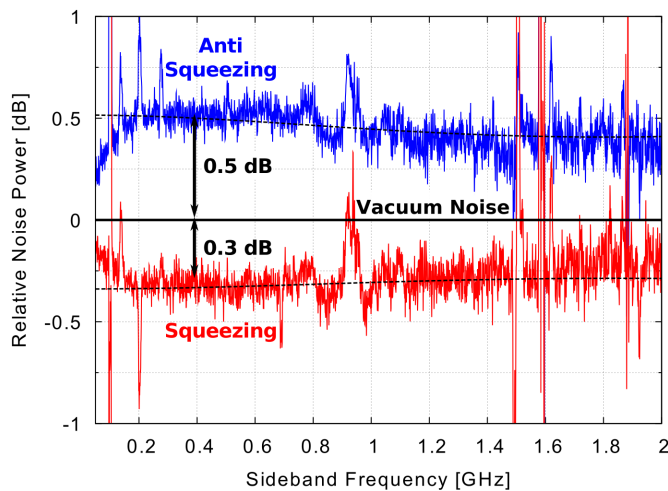


Figure 4.7.: Quantum noise spectra normalized to vacuum noise. The spectrum was obtained by combining four individually measured spectra with 500 MHz bandwidth. The spectrum analyzer used a resolution bandwidth (RBW) of 10 MHz and a video bandwidth (VBW) of 200 Hz. **Blue:** Anti-Squeezing, **Red:** Squeezing, **Black:** Vacuum noise level. The traces shown include a dark-noise correction, which allows a comparison with numerical simulations of our system (dashed lines) and which marginally improves the squeezing data only above 1 GHz. A nonclassical noise suppression (squeezing) of up to 0.3 dB and 0.5 dB of anti-squeezing are observed from 0.05 - 2 GHz. [62]

4. Squeezed light source without squeezing resonator

level of 2.1 dB below shot noise for our cavity design. When we further increased the input pump power, we did not observe a corresponding increase of the intra-cavity pump power. The cavity transmitted light power did not increase, and the squeezing factor did not improve either. From these observations we conclude that thermal lensing inside the crystal reduced the spatial overlap between the pump field and the fundamental field being mode-matched to the BHD. This limited the achievable squeezing to 2.1 dB with the given cavity design and the limitation in pump power.

4.4.3. Total detection efficiency estimation

A calculation based on a lossless initial squeezing value of around 2.1 dB was used to determine the total optical loss for the squeezing measurement. The gain of about 1.62 at 250 mW pump power for optical parametric amplification was in good agreement with the estimated initial squeezing value. The simulation yielded a total loss of around 80 % (see Fig. 4.8).

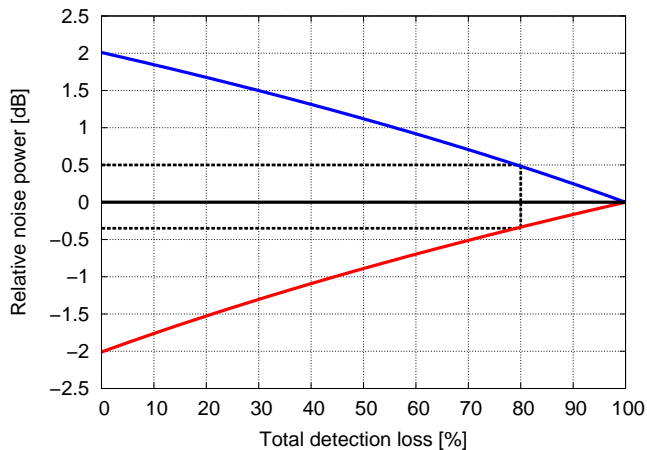


Figure 4.8.: Total detection loss plotted against squeezing and anti-squeezing strength. The initial squeezing for zero loss is 2.1 dB for the hemilithic OPA pumped with 250 mW harmonic light. This initial squeezing value fits the measured parametric gain. The measured squeezing and anti-squeezing values suggest a loss of 80 %, which corresponds to a total detection efficiency of 0.2. The individually estimated loss sources are the homodyne detection visibility (0.774), the optical path loss (0.85) and the quantum efficiency of the photodiodes (0.3).

The highest contribution for the loss was the poor quantum efficiency of less than 0.3 from the FCI-H250G-InGaAs-70 photodiodes. The homodyne detection visibility yielded an efficiency of $0.88^2 = 0.774$. The optical path loss reduced the efficiency by another factor of 0.85. The resulting total detection efficiency was only about 0.2, which corresponds to a loss of 80 % in the experiment.

4.5. Summary & Outlook

In this chapter, I described the design and implementation of a squeezed light source without resonant enhancement for the fundamental wavelength. The goal was to obtain a squeezed light source with a white squeezing spectrum over several GHz of bandwidth. Our result serves as a proof-of-principle experiment for the generation of a GHz bandwidth squeezed state, which can be used to generate two-mode squeezing for high-speed entanglement-based QKD.

We produced a continuous-wave squeezed vacuum field with a measured squeezing bandwidth of 2 GHz with 0.3 dB of squeezing and 0.5 dB of anti-squeezing. To the best of our knowledge, this is the highest cw squeezing bandwidth ever observed.

The bandwidth of our squeezing source was possibly only limited by the crystal's phase-matching bandwidth. However, the observed squeezing spectrum was considerably narrower and limited by the 2 GHz detection bandwidth of the homodyne detector.

The measured squeezing strength was just up to 0.3 dB below shot noise, which is too low for efficient entanglement-based QKD. The squeezing value was limited by insufficient intra-cavity pump power due to thermal lensing in the crystal and the poor quantum efficiency of about 30 % for the homodyne detector photodiodes.

The conclusion from our experiment is that it will be necessary to find a trade-off between the bandwidth and squeezing strength of the source. This trade-off can be realized by applying an enhancement resonator with a large linewidth of several GHz at the fundamental wavelength. A cavity with only several millimeters of optical length and a reflectivity around 50 % for the outcoupling mirror of the fundamental squeezed field will be a good possibility. The result will be a strong enhancement of the squeezing factor due to the fundamental cavity finesse, while only sacrificing the non-detectable bandwidth above 2 GHz. The realization of such a squeezing resonator design will be discussed in the next chapter 5.

5

Chapter 5.

High-bandwidth monolithic squeezing resonator

5.1. Introduction

The experiment in the previous chapter was motivated by the possibility of an enhanced data rate for QKD via high bandwidth squeezed light. Unfortunately, the use of a hemilithic squeezing resonator without fundamental cavity only yielded a nonclassical noise suppression of 0.3 dB below vacuum noise. The setup was fundamentally limited to a squeezing value of 2 dB, which would limit the available secret key rate to very low values. This result demanded a new cavity design to achieve a trade-off between high bandwidth and reasonable squeezing strength.

The following chapter introduces a newly designed monolithic PPKTP squeezing resonator. This cavity was designed to have a very high free spectral range, while employing a mediocre finesse for the squeezing wavelength. The goal was to build a high-bandwidth squeezed light source with the potential of having a strong nonclassical noise suppression.

I will first describe the simulation which led to the design of the compact monolithic squeezing resonator. I will then give an overview of the experimental setup with an analysis of the cavity mode-matching. Three different homodyne detectors were characterized, which exhibited different detection efficiencies and measurement bandwidths. The squeezing measurements will be presented using all three homodyne detectors for comparison. I will examine the optical detection loss and thus the limitations for the squeezing measurements. Finally, I will

5. High-bandwidth monolithic squeezing resonator

conclude with a summary and an outlook.

This chapter is based on our publication in the journal Optics Express (see [63]).

5.2. Design of the monolithic crystal cavity

The experiences from the experiment described in chapter 4 were used for designing the squeezing resonator via simulations implemented with N.L.C.S. The cavity was designed to be a 2.6 mm long monolithic PPKTP crystal cavity yielding a high finesse for the harmonic pump field and a mediocre finesse for the fundamental squeezing wavelength. The intention was to have a good trade-off between high squeezing strength and bandwidth.

An N.L.C.S. simulation was performed to analyze the frequency dependent squeezed field for the cavity while changing the harmonic pump power and the fundamental incoupling reflectivity of the cavity. Afterwards a frequency domain simulation with “Finesse” provided the cavity parameters and the mode degeneracy of the resonator.

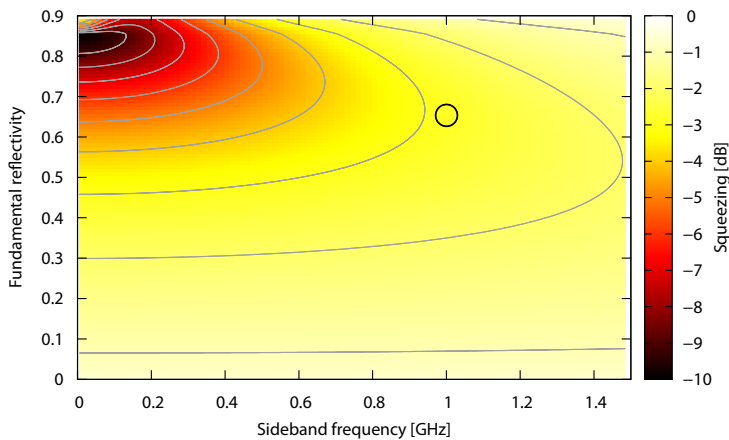


Figure 5.1.: Monolithic squeezing resonator design simulation with N.L.C.S. for a variation of the incoupling reflectivity for the fundamental field versus sideband frequency. The major parameters for the simulation were a length of 2.6 mm for the crystal cavity and a harmonic pump power of 0.1 W. The squeezing at 1 GHz sideband frequency reaches a maximum of 2.8 dB at 64 % of fundamental reflectivity (black circle).

5.2.1. Squeezing optimization with N.L.C.S.

The N.L.C.S. simulations varied two parameters for the 2.6 mm long crystal cavity to achieve at least 3 dB squeezing at 1 GHz. The fundamental squeezed output reflectivity and the harmonic pump power. All simulations included a reflective coating of $R_1 = 99.98\%$ at 1550 nm for the rear side of the PPKTP crystal and surface reflectivities of $R_1 = 98\%$, $R_2 = 99.98\%$ yielding a cavity finesse of about 307 for the pump field at 775 nm. This compensated for the low enhancement of the squeezed field with a specified finesse between 1 and 60. Furthermore a crystal nonlinearity $\chi_{\text{eff}}^{(2)} = 6.5 \text{ pm/V}$ for PPKTP was used for the simulation. The N.L.C.S. script with all parameters can be found in appendix A.2.

In the first simulation, the fundamental incoupling reflectivity was varied from 0-90% (see Fig. 5.1). The plot shows a frequency spectrum of the simulated squeezing with 90% detection efficiency and 0.1 W of harmonic pump power. The maximally available squeezing at 1 GHz for those parameters was about 2.8 dB at a fundamental reflectivity of around 64%.

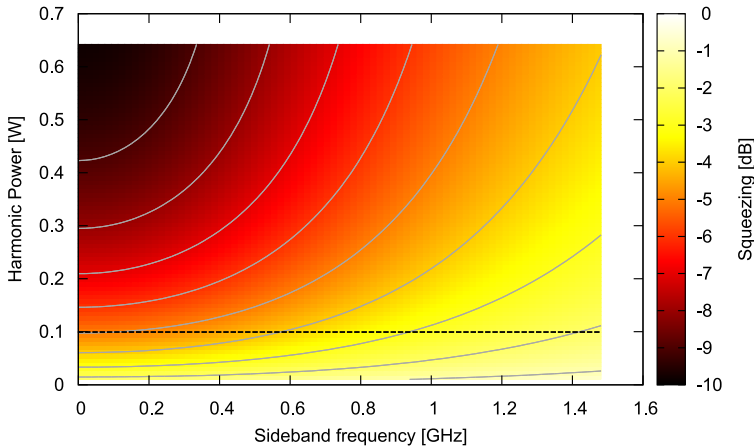


Figure 5.2.: Monolithic squeezing resonator design simulation with N.L.C.S. for a variation of the harmonic pump power versus sideband frequency. The simulation used a crystal length of 2.6 mm and a fundamental output mirror reflectivity of 64% as fixed parameters. In principle, a squeezing value of about 5.5 dB at 1 GHz sideband frequency should be possible with a detection efficiency of 90% and 650 mW pump power. The dashed line corresponds to the results obtained from Fig. 5.1.

5. High-bandwidth monolithic squeezing resonator

In the second simulation, the reflectivity of 64% was fixed and the harmonic pump power was varied (see Fig. 5.2) from 0.01 W to the parametric oscillation threshold at 0.655 W. The observations from chapter 4 suggested that the external pump power was limited to about 350 mW (67.9 W internal) due to thermal effects in the crystal cavity.

A squeezing level of 4.8 dB at 1 GHz seemed feasible with a pump power of 350 mW, assuming a cavity with the simulated optimal reflectivity of 64% and a total detection efficiency of 90%.

5.2.2. Monolithic crystal cavity mode degeneracy

I simulated the mode degeneracy of mode orders up to 10 for the given parameters by using the frequency domain simulation tool “Finesse”. The simulation for the (squeezing) wavelength of 1550 nm revealed a mode spacing of 1.55 GHz from the fundamental TEM_{00} mode to the adjacent mode of fifth order (see Fig. 5.3). Unfortunately, this was within the cavity linewidth of 2.26 GHz for the squeezing resonator. In this case, the high linewidth is the major limitation in achieving weak mode degeneracy.

On the other hand, the mode degeneracy of the pump field at 775 nm was much better (see Fig. 5.4). The fifth order mode adjacent to the fundamental TEM_{00} mode was far outside of the small linewidth of approximately 101 MHz for 775 nm.

The mode non-degeneracy of the pump field should in principle suppress the poor mode degeneracy at the squeezing wavelength, since the harmonic TEM_{00} mode at 775 nm is down-converted to squeezed photons at 1550 nm. It is unlikely for photons to convert from a harmonic TEM_{00} mode to a fifth order cavity mode of the fundamental field. However, a deformation of the control field mode at the beam coupled out of the squeezing resonator was observed. This might have been caused by the slight mode degeneracy but the origin could not be verified (see section 5.5).

5.2. Design of the monolithic crystal cavity

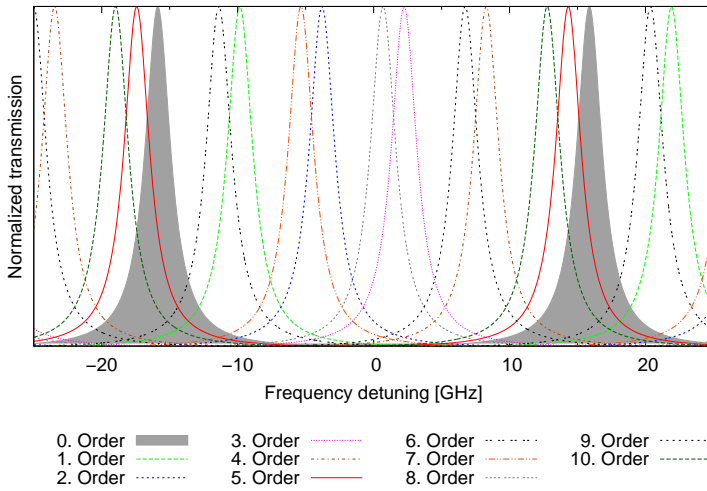


Figure 5.3.: “Finesse” simulation calculating the mode degeneracy of the 2.6 mm monolithic PPKTP crystal cavity at the squeezing wavelength of 1550 nm. The fundamental TEM_{00} mode and the adjacent fifth order mode have a frequency distance of roughly 1.55 GHz, which is within the cavity linewidth of 2.26 GHz. This might have introduced additional loss for the squeezed field and was a possible reason for a later observed control field mode deformation. Further details are given in the text.

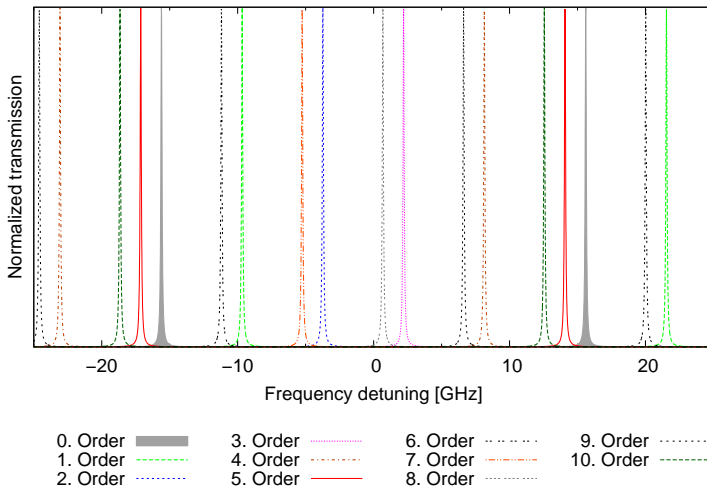


Figure 5.4.: “Finesse” simulation calculating the mode degeneracy of the 2.6 mm monolithic PPKTP crystal cavity at the pump wavelength of 775 nm. The fundamental TEM_{00} mode is well separated from the adjacent fifth order mode due to the small linewidth of about 101 MHz for the harmonic field.

5. High-bandwidth monolithic squeezing resonator

5.3. Monolithic cavity parameters & crystal oven

The final squeezing resonator design consisted of a biconvex monolithic PPKTP crystal with reflective coatings for 775/1550 nm and radii of curvature of 12 mm on its surfaces. The crystal coating's reflectivities were $R_1 = 99.98\%$, $R_2 = 64\%$ at 1550 nm and $R_1 = 98\%$, $R_2 = 99.98\%$ at 775 nm, respectively. Together with the short crystal (cavity) length of 2.6 mm, this led to a high resonator bandwidth of about 2.26 GHz, a finesse of about 14 and a free spectral range of about 31.75 GHz for the squeezing wavelength of 1550 nm.

The finesse measured for the 775 nm pump field was 307, corresponding to a resonant enhancement of the intra-cavity power by a factor of about 194. The squeezing resonator was pumped with 375 mW of 775 nm light (73 W intra-cavity). This was below the OPA threshold power of 655 mW (127 W intra-cavity). I numerically simulated the

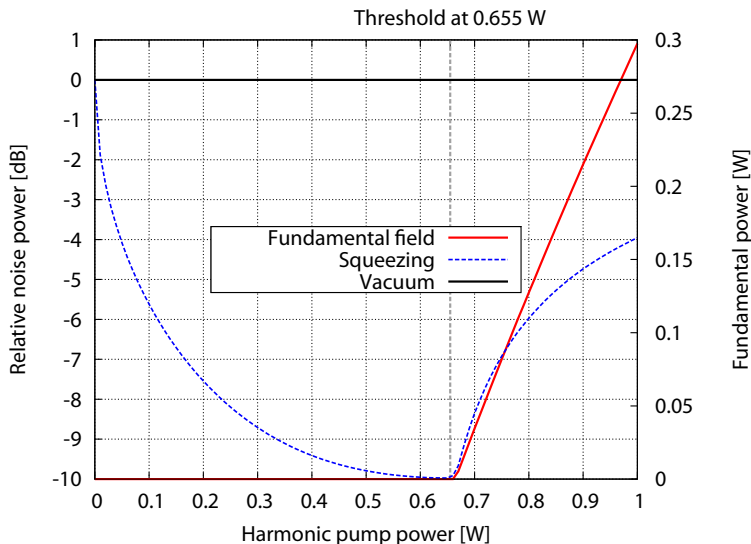


Figure 5.5.: Monolithic squeezing resonator design simulation with N.L.C.S. for the squeezing strength (left axis) and the fundamental power from the parametric oscillation (right axis) plotted against the harmonic pump power. The squeezing strength increases up to 10 dB with an increasing pump power assuming a detection efficiency of 90%. Above the threshold of 655 mW pump power the parametric oscillation generates a bright field at 1550 nm. As theory predicts, the squeezing is decreasing rapidly above the oscillation threshold. Note that the simulation used a higher crystal nonlinearity of $d_{\text{eff}} = 7.3$ pm/V in comparison to the other simulations, which was derived from the later experimental results. The full simulation script can be found in appendix A.2.

5.3. Monolithic cavity parameters & crystal oven

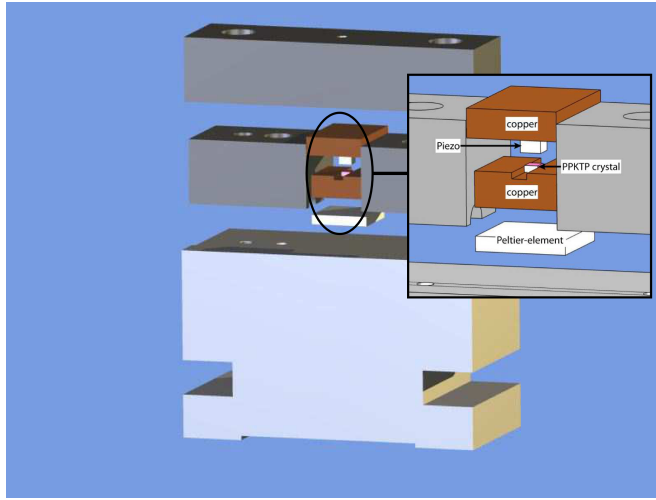


Figure 5.6.: Schematic CAD drawing of the squeezing resonator oven construction designed with *Autodesk Inventor*. The gray part at the bottom is a mount made of aluminum, while the three upper parts in black are made of polyoxymethylene (POM). Stainless steel screws were used to assemble the oven components. Further details are given in the text.

threshold with N.L.C.S. by taking into account the intra-cavity waist sizes of $w_{0,1550} = 33.86 \mu\text{m}$ and $w_{0,775} = 23.94 \mu\text{m}$, the crystal's experimentally measured effective nonlinearity of $d_{\text{eff}} = 7.3 \text{ pm/V}$ and the crystal's absorption for both wavelengths (see Fig. 5.5).

We measured the absorption for PPKTP to be $\alpha_{1550} = 84 \pm 40 \text{ ppm/cm}$ and $\alpha_{775} = 127 \pm 26 \text{ ppm/cm}$ for the fundamental and harmonic wavelengths, respectively, as reported in reference [56].

The housing for the monolithic crystal cavity was an in-house fabricated aluminum construction (see Fig. 5.6). A small copper piece supported the crystal and acted as thermally conducting material for the temperature stabilization. A Negative Temperature Coefficient Thermistor (NTC) sensed the temperature of the crystal from within a small hole inside the copper. Below the copper, a Peltier-element was actively stabilizing the cavity to resonance via manual adjustment of the crystal temperature. A feed-back control loop for the cavity resonance was not necessary due to the intrinsically stable, short monolithic cavity design. At the chosen temperature, the crystal was also close to its quasi-phase matching temperature of about 46°C . Originally, a $3 \times 3 \text{ mm}^2$ piezo actuator was placed on top of the crystal. The piezo was meant to act as a length tuning device for the

5. High-bandwidth monolithic squeezing resonator

cavity via tension induced refractive index changes. Unfortunately, we did not see any length change effect by applying a supply voltage of up to 100 V to the piezo and thus the temperature control was used to stabilize the cavity on resonance.

5.4. Experimental setup

A schematic overview of our experimental setup is shown in Fig. 5.7. The laser source was an erbium-doped fiber laser with an output power of 1.3 W at 1550 nm. A three-mirror ring cavity served as a spatial mode cleaning device and suppressed amplitude- and phase noise above its linewidth of about 2.6 MHz. A fraction of the power was transmitted towards the balanced homodyne detector as a local oscillator beam as well as a control beam for the alignment of the squeezed vacuum mode onto the balanced homodyne detector.

The remaining 1.1 W was converted into about 1 W at 775 nm inside a second-harmonic generation resonator. Details on the SHG are described in [21]. A second three-mirror ring cavity filtered the light at 775 nm, which was then coupled into the optical parametric amplifier. We observed a small thermally induced deformation of the cavity

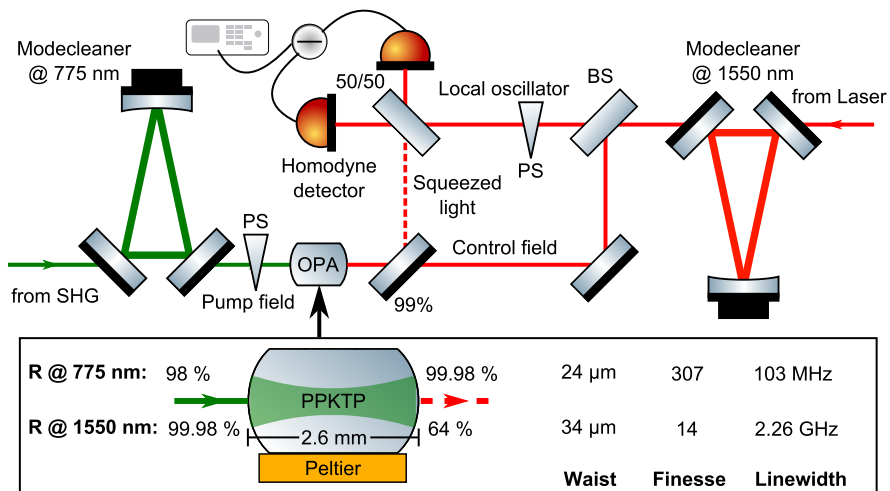


Figure 5.7.: Schematic of the experimental setup. Modecleaner: three-mirror ring cavity for spatial mode filtering; OPA: monolithic PPKTP cavity (squeezing resonator) with reflective coatings on the crystal surfaces; control field: reference beam for alignment of the squeezed vacuum mode onto the balanced homodyne detector; BS: beam splitter; PS: piezo-actuated mirror for shifting the phase. [63]

mode and second-harmonic generation to 387.5 nm in the squeezing resonator. For further details see section 5.9. To avoid damaging the crystal, we did not increase the intra-cavity pump power to more than 72 W.

The squeezed vacuum state left the crystal opposite to the side through which the pump field entered. It propagated through several mode-matching optics and was detected with a balanced homodyne detector. A control field at 1550 nm served as a spatial reference for the propagating squeezed vacuum and was used to adjust the homodyne detector visibility. We blocked the control field while performing the squeezed light measurement.

We subsequently used three homodyne detectors with different electronic circuits and photodiodes for measuring and analyzing the squeezing.

5.4.1. Cavity mode-matchings & parametric gain

A schematic picture explaining the mode-matching procedures is depicted in Fig. 5.8.

We first matched the mode of the control field to the monolithic squeezing resonator. It served as a reference beam for the visibility adjustment as well as a phase reference for the homodyne readout phase angle stabilization. The control field was coupled into the cavity through the reflective coating with 64 % for 1550 nm and detected

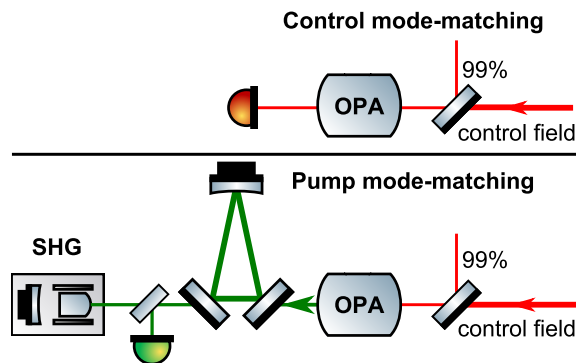


Figure 5.8.: Schematic setups for the mode-matching of the control field (top) and the pump field (bottom). The control field mode-matching was detected in transmission of the monolithic crystal cavity with about $500 \mu\text{W}$ of 1550 nm light. The mode-matching of the pump field was acquired by frequency doubling the control field in the nonlinear crystal and detecting the light in transmission of a modecleaner in the pump path.

5. High-bandwidth monolithic squeezing resonator

with a photodetector in transmission of the squeezing resonator. For a rough mode-matching of the cavity, the laser frequency was scanned by applying a voltage to the internal laser piezo-actuator. The tuning range of the laser frequency was too small to achieve a full mode scan over the large FSR of 31.75 GHz for the monolithic resonator. A fine tuned mode-matching was thus achieved by continuously sweeping the crystal temperature (see Fig. 5.9a) and therefore changing the effective crystal length. This was very challenging due to the slow actuation of the temperature control. Some higher order modes were present in the mode spectrum, thus limiting the mode-matching to around 81 %. Note that the different fundamental resonance peaks' widths as well as their spacing arise from the nonlinear response of the crystal length to the temperature tuning. The plot shows a steady heating of the crystal for a time of about 40 s, which occurs much faster at lower temperatures than at higher temperatures.

The pump field was mode-matched by converting the 1550 nm control field to its harmonic wavelength in the squeezing resonator (see Fig. 5.9b). The crystal was stabilized on resonance for frequency doubling by temperature control. The converted 775 nm light was mode-matched to a modecleaner in the pump path. Therefore, the cavity length was continuously tuned and a photodiode in transmission of the MC detected the 775 nm field. We achieved a mode-matching of more than 98 % of the pump field to the squeezing resonator.

Finally, a measurement of the parametric gain was performed to verify the later squeezing results. We therefore injected both the control field and the pump field into the cavity, while stabilizing the cavity length and the quasi-phase matching with the temperature controller. The pump field phase was continuously swept via a piezo-actuated mirror in the beam path, to change from an amplification to a de-amplification process.. A photodetector measured the parametric gain of the 1550 nm field in reflection of the squeezing resonator. We used a control field of about 0.5 mW and a pump field of about 395 mW, which resulted in a parametric gain of about 9 (red). We detected a non-amplified reference signal for the photodetector by blocking the pump field in front of the cavity (blue), while a null measurement was acquired by also blocking the control field (black).

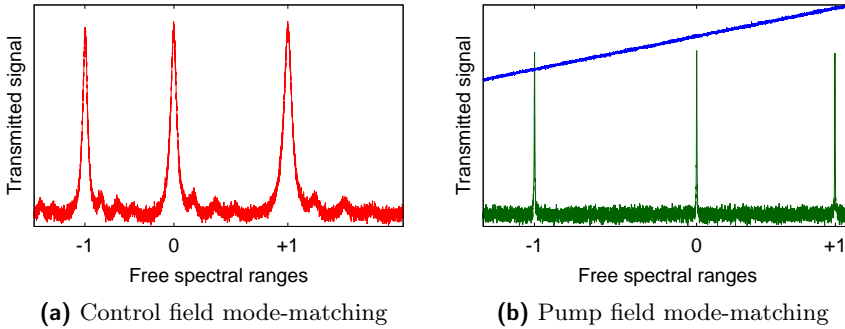


Figure 5.9.: Mode-matchings of the control field and the pump field to the monolithic squeezing resonator. The control field (left) was mode-matched with an efficiency of about 81 %. The cavity length was tuned by heating the crystal with the Peltier-element. The mode scan (red) was performed over two full FSRs and was detected with a photodiode in transmission of the cavity. Some higher order modes are visible in the spectrum. The different peak widths and the unequal spacing between the FSRs is due to the nonlinear response of the crystal to the heating procedure. The pump field (right) was mode-matched with an efficiency of more than 98 %. The measurements were performed by frequency doubling the 1550 nm field in the nonlinear cavity and mode-matching the resulting 775 nm light to a MC in its pump path. The plot shows the ramp signal used to scan the MC cavity length (blue) and the transmitted signal of the 775 nm pump field (dark-green).

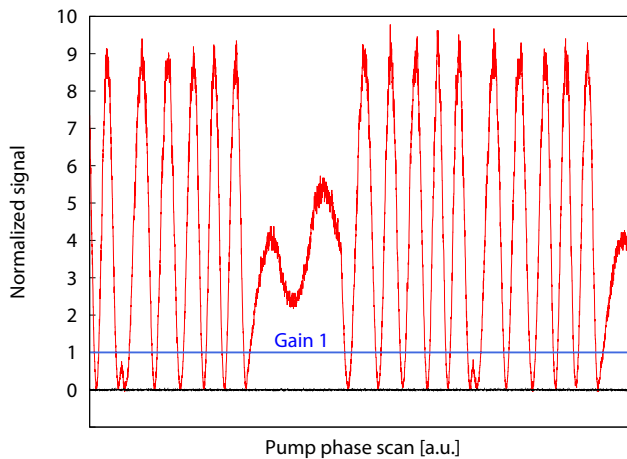


Figure 5.10.: Parametric gain of the monolithic crystal cavity measured with 395 mW pump power at 775 nm and about 0.5 mW of control field power. A piezo actuated mirror continuously swept the phase of the pump field. This changed the effect from amplification to deamplification with a resulting gain of about 9 (red) with respect to the reference measurement (blue). A null measurement is acquired by blocking the photodiode (black).

5.5. Optical path loss estimation

The propagation loss in the squeezed field path was estimated to be about $L = 0.1$ due to non-perfect HR/AR coatings on mirrors and lenses. We observed a lower limit for the homodyne visibility of around $\eta_{\text{vis}} = 0.9$. The outcoupling efficiency of our squeezing resonator was close to unity and was therefore negligible in our experiment. Without taking the photodiode quantum efficiency into account, the detection efficiency was $\eta = \eta_{\text{vis}}^2 \cdot (1 - L) = 0.73$.

The homodyne detection visibility was limited to $\eta_{\text{vis}} = 90\%$ due to a deformation of the control field's fundamental mode, which was coupled out of the squeezing resonator. We were not able to determine the exact origin of the effect. It was possibly due to second harmonic generation of the 775 nm pump field, which lead to the generation of 387.5 nm light (see section 5.9). Other possible reasons could be thermal lensing inside the crystal or the slight mode degeneracy of the cavity's fundamental mode with the fifth order mode. We ruled out impurities of the crystal.

5.6. Squeezed vacuum measurement with GHz bandwidth

We performed a squeezed vacuum measurement with GHz bandwidth using a commercially available homodyne detector. I will describe the characterization of the homodyne detector including dark noise spectra, vacuum noise measurements and the photodiode's quantum efficiencies. Then I will present the squeezing measurements at frequencies up to 1.2 GHz and analyze the overall detection loss in the experimental setup.

5.6.1. GHz bandwidth homodyne detector characterization

The first detector we used was a balanced photo receiver from *New Focus*, type *1617-AC FS* with InGaAs photodiodes having an active area of 100 μm . The data sheet specified a responsivity of 1.0 A/W at 1550 nm, which converted into a quantum efficiency of about 0.8 not taking into account reflection loss on the diode's TO window and surface. We characterized the detector by measuring the dark noise as well as the vacuum noise with 1 mW and 2 mW, respectively. At a local oscillator power of 2 mW (1 mW for each photodiode) the detector had

5.6. Squeezed vacuum measurement with GHz bandwidth

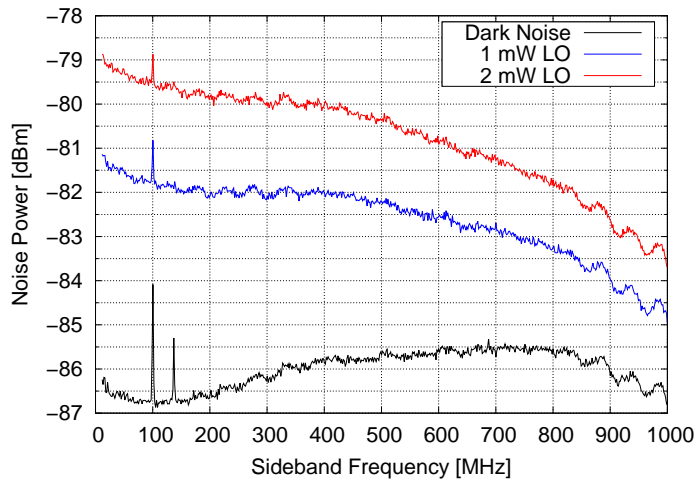


Figure 5.11.: Characterization of the *New Focus 1617-AC FS* homodyne detector. A measurement of the detector dark noise and a total local oscillator power of 1 mW and 2 mW are depicted. The spectrum analyzer was set to a resolution bandwidth (RBW) of 5 MHz, a video bandwidth (VBW) of 3 kHz and a sweep time of 170 ms. The dark-noise clearance with 2 mW local oscillator power ranged from 7 dB at 10 MHz to around 3 dB at 1 GHz.

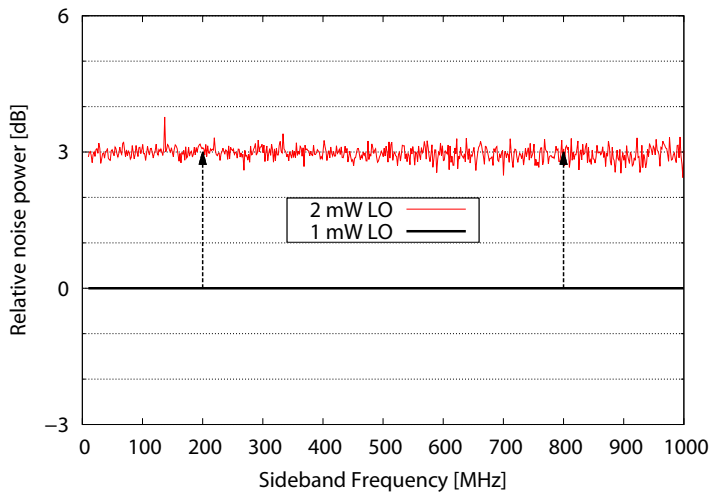


Figure 5.12.: Dark-noise corrected *New Focus 1617-AC FS* spectrum normalized to 1 mW local oscillator power for characterizing the homodyne detector's linearity. We doubled the local oscillator power from 1 mW to 2 mW, with a resulting noise level increase of about 3 dB. This clearly proved a shot noise limited measurement as well as the homodyne detector's linearity.

5. High-bandwidth monolithic squeezing resonator

a dark-noise clearance ranging from 7 dB at 10 MHz to around 3 dB at 1 GHz (see Fig. 5.11). The recorded spectra were measured with a spectrum analyzer type *FSU 3.6 GHz* from *Rhode & Schwarz* with a resolution bandwidth (RBW) of 5 MHz, a video bandwidth (VBW) of 3 kHz and a sweep time of 170 ms.

We measured a dark-noise corrected spectrum normalized to 1 mW of local oscillator power to verify the homodyne detector's linearity (see Fig. 5.12). The plot clearly shows that doubling the power from 1 mW to 2 mW resulted in a rising noise level of 3 dB, which was a proof for the detector's linear behavior at this local oscillator powers.

5.6.2. First GHz bandwidth measurement

We performed the squeezed vacuum measurement by blocking the control field before the squeezing resonator, using a pump power of 375 mW and a local oscillator power of 2 mW. Figure 5.13 shows a dark-noise corrected squeezing spectrum from 10 MHz to 1.2 GHz normalized to the vacuum noise level. Our measurement yielded a maximal squeezing value of up to 3.0 dB and an anti-squeezing value of up to 10.4 dB at a frequency of 50 MHz. The squeezed vacuum decreased to 2 dB and the anti-squeezed vacuum decreased to 3.5 dB at sideband frequencies of 1.2 GHz due to the finite linewidth of 2.26 GHz for the squeezing resonator. Note that the directly observed squeezing was about 2.5 dB at 10 MHz and about 1 dB at 1.2 GHz limited partly by the low dark-noise clearance of the balanced photodetector. Nevertheless, we measured a squeezed vacuum state with a 10-15 fold increase in bandwidth compared to typical previous squeezing resonators (see gray shaded area in Fig. 5.13).

The measured values correspond to a total detection efficiency of about 0.53. Using the visibility related homodyne efficiency of $\eta = \eta_{\text{vis}}^2 \cdot (1 - L) = 0.73$, we deduced a photodiode detection efficiency of 73%. The dark-noise corrected squeezing strengths are thus mainly limited by optical losses in the detection process.

We numerically simulated the measurements with the given parameters for the cavity, the pump field and the homodyne detection efficiency using N.L.C.S. The simulations are in very good agreement with the measured spectra. They include the decreasing noise suppression due to the cavity linewidth limitation and can be found as dashed lines in Fig. 5.13.

5.7. High detection efficiency MHz bandwidth measurement

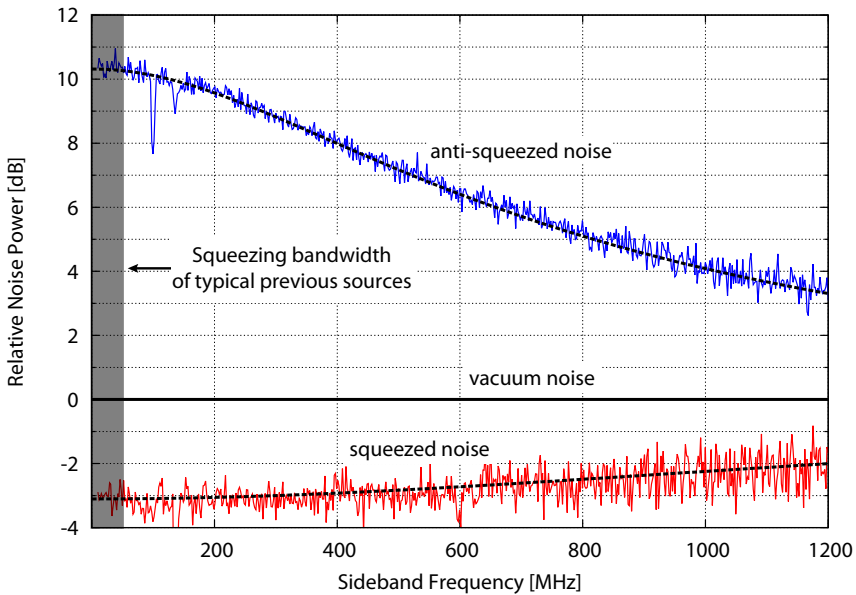


Figure 5.13.: Squeezed vacuum measurement from 10 MHz to 1.2 GHz sideband frequency using the balanced photo receiver *New Focus* type *1617-AC FS*. We measured a squeezing (red) of up to 3 dB as well as anti-squeezing (blue) of up to 10.4 dB above vacuum noise (black). Squeezing decreased to 2 dB and anti-squeezing to 3.5 dB due to the finite cavity linewidth of the squeezing resonator. The measurements shown are dark-noise corrected. The dark-noise clearance was merely 7 dB at 5 MHz decreasing to 3 dB at 1 GHz. Typical previous squeezed light sources had bandwidths that were orders of magnitude smaller than our bandwidth (see for example [21, 64, 65, 66]), which is highlighted here by the gray-shaded area. The total detection efficiency of our system was fitted to be 53%. N.L.C.S. used all given parameters to simulate the measured squeezing (dashed black). [63]

5.7. High detection efficiency MHz bandwidth measurement

Our second measurement used an in-house made homodyne detector based on custom-made high quantum efficiency photodiodes and covered sideband frequencies between 5 and 100 MHz. We used the same homodyne detector in publication [21] to measure 12.3 dB of squeezing at 1550 nm. The detector's photo currents were directly subtracted, electronically amplified and fed forward to the spectrum analyzer. This allowed local oscillator powers as high as 5 mW saturating neither the homodyne detector's photodiodes nor the operational amplifiers. Due to the high electronic gain and the high local oscillator

5. High-bandwidth monolithic squeezing resonator

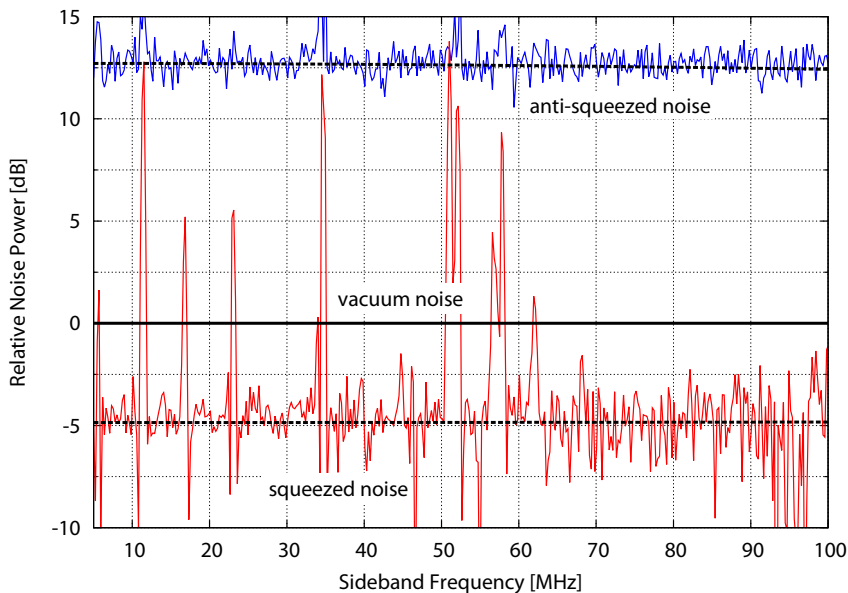


Figure 5.14.: Squeezed vacuum measurement from 5 to 100 MHz sideband frequency using a homodyne detector with 99% quantum efficiency. We measured squeezing (red) of 4.8 dB and anti-squeezing (blue) of 12.7 dB with respect to the vacuum noise level (black). The measurement is dark-noise corrected. The measured squeezing below 20 MHz is, however, not influenced by the dark noise correction due to the detector’s low dark noise at low frequencies. The total detection efficiency was fitted to be 72.5%. The dashed black lines correspond to our numerical simulation. The peaks in the squeezing spectrum originated from electronic pick-up of the homodyne detector due to antenna effects and are also visible in the detector’s dark noise. [63]

power, the detector yielded a dark-noise clearance of 20 dB at 5 MHz decreasing to less than 3 dB at 100 MHz. The high transimpedance gain as well as the finite speed of the photodiodes were responsible for the decreasing dark-noise clearance and limited the detector’s bandwidth. At frequencies above 100 MHz the low dark-noise clearance prevented useful squeezing measurements.

The experiment was performed with 5 mW local oscillator power, 375 mW harmonic pump power for the squeezing resonator, an RBW of 500 kHz, a VBW of 3 kHz and a sweep time of 170 ms. The measurements without dark-noise correction yielded a nonclassical noise suppression of about 4.8 dB at 5 MHz and about 2 dB at 100 MHz, which was limited by a dark-noise clearance as low as 3 dB. Fig. 5.14 shows dark-noise corrected measurements of squeezed and anti-squeezed

5.8. High detection efficiency GHz bandwidth measurement

quadratures, normalized to the vacuum noise level. We measured squeezing values of up to 4.8 dB and anti-squeezing of up to 12.7 dB over the full detected spectrum from 5-100 MHz. The sharp peaks in the spectrum originated from electronic pick-up from the power supply due to antenna effects and a Pound-Drever-Hall modulation frequency at 24 MHz.

Using the squeezed light measurement, we deduced the photodiode's detection efficiencies to be around 99% with a homodyne efficiency of $\eta = \eta_{\text{vis}}^2 \cdot (1 - L) = 0.73$. This refers to a total detection efficiency of 0.725. The measured squeezing value between 5 and 100 MHz is thus limited mainly by the homodyne visibility η_{vis} and the optical path losses $L = 27\%$.

We again simulated the measured spectrum with the given parameters for the cavity (including linewidth), the pump field and the different homodyne detection efficiency (see section 5.6.2) using N.L.C.S. The simulation nicely fitted the measurements for squeezing as well as anti-squeezing and are depicted as dashed lines in Fig. 5.14.

5.8. High detection efficiency GHz bandwidth measurement

For the last squeezed light measurement I implemented a home-made homodyne detector using custom made photodiodes with 99% quantum efficiency. We also stabilized the pump phase for the squeezing resonator as well as the homodyne detector phase to improve the measurement results.

I will characterize the homodyne detector's performance and present some dark-noise as well as vacuum noise measurements. The stabilization techniques for the pump field and the homodyne detector phase will be explained schematically. I will present optimized squeezed light measurements up to 1.6 GHz sideband frequency. Finally, the total optical loss will be analyzed and the limitation to the measured squeezing will be discussed.

5.8.1. Custom-made GHz homodyne detector characterization

A novel homodyne detector design was developed by M. Mehmet to combine a large measuring bandwidth with highly efficient photodiodes.

5. High-bandwidth monolithic squeezing resonator

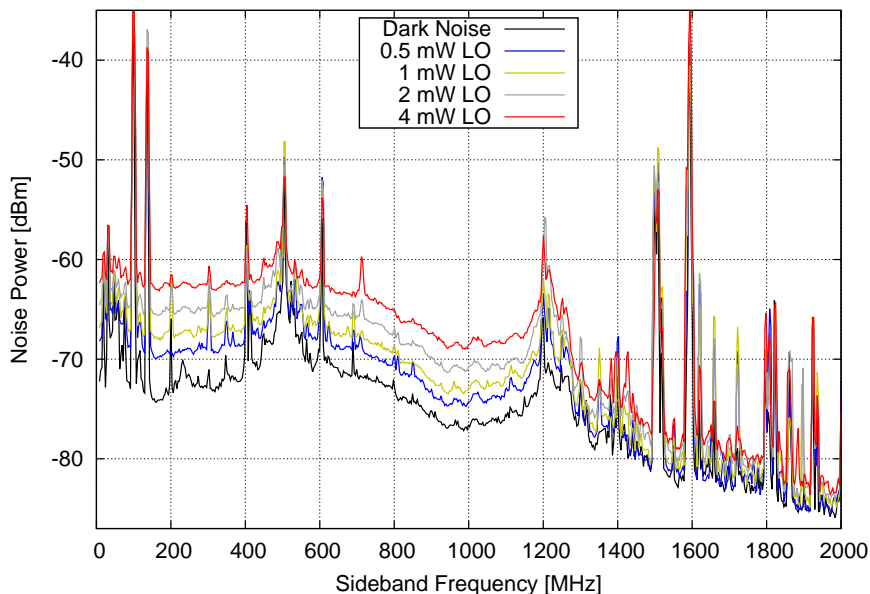


Figure 5.15.: Characterization of the in-house made homodyne detector using InGaAs photodiodes with an active area of $70\ \mu\text{m}$ and a quantum efficiency of 99%. The plot shows the dark noise as well as the vacuum noise levels for different local oscillator powers. The dark-noise clearance is around 10 dB at 200 MHz and 7 dB at 1 GHz with a local oscillator power of 4 mW. Several peaks due to electronic pick-up appear in the spectrum, especially peaks at 101 MHz and 138 MHz from PDH modulation frequencies.

The homodyne detector circuit was using the directly subtracted currents of two photodiodes. The outputs were divided into an AC and a DC path with transimpedance amplifiers converting the differential current into voltages. The AC path contained two microwave amplification transistors type *Mini circuits MAR-6+* for the high frequency AC signal generation.

We used custom made InGaAs photodiodes with an active area of $70\ \mu\text{m}$ and a specified quantum efficiency of 99% for the homodyne detector. The photodiodes suffered from high electronic pick-up noise due to a large TO housing as well as a combined pin for cathode and ground. The photodiode was effectively forming an antenna, which contaminated large parts of the spectrum with electro-magnetic interspersal.

We characterized the homodyne detector's dark noise and performed vacuum noise measurements using different local oscillator powers (see

5.8. High detection efficiency GHz bandwidth measurement

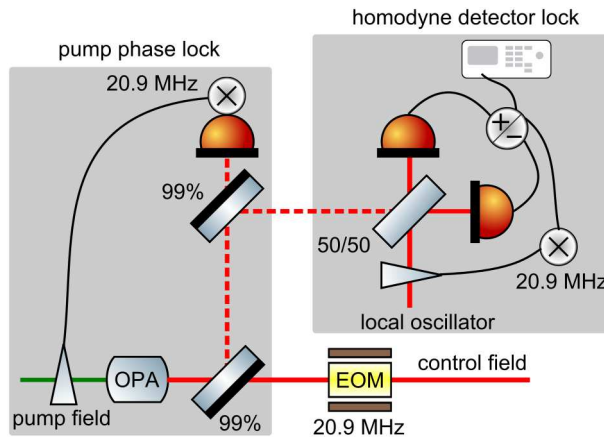


Figure 5.16.: Schematic of the stabilization for the pump phase and homodyne detection phase. An EOM imprinted a phase modulation at 20.9 MHz on the control beam. We injected about $500 \mu\text{W}$ into the squeezing resonator and used a photodetector in the squeezing path for the pump phase stabilization. The homodyne detection phase between the squeezed field and the local oscillator was stabilized via the homodyne detector output signal.

Fig. 5.15). The vacuum noise level at 4 mW local oscillator power was around 10 dB at 200 MHz and 7 dB at 1 GHz. Above 1.2 GHz, both the dark noise and the vacuum noise included a high number of electronic pick-up peaks. Nevertheless the dark-noise clearance was as high as 2 dB up to a frequency of 2 GHz. Further electronic noise is present below 1 GHz, with the highest contribution being Pound-Drever-Hall modulation frequencies at 101 MHz and 138 MHz as well as their harmonics. Despite the high electronic pick-up, the homodyne detector was capable of measuring squeezing with a high detection efficiency and a high dark-noise clearance over a range of 2 GHz.

5.8.2. Stabilization techniques for the monolithic squeezing resonator

The second improvement for the experiment was the implementation of a full stabilization scheme for the pump phase of the squeezing resonator as well as for the homodyne detector phase. The cavity was again held on resonance via manually tuning the crystal temperature and thus stabilizing the crystal length.

The enhanced experimental setup is depicted in Fig. 5.16. We inserted an EOM in the control beam path of the monolithic squeezing resonator, imprinting a phase modulation at 20.9 MHz on the beam.

5. High-bandwidth monolithic squeezing resonator

About 500 μW entered the cavity and generated a parametric gain signal for the pump phase stabilization. A photodetector with a built-in mixer demodulated the corresponding error signal in transmission of a 99% mirror in the squeezing path. This control signal was fed to a piezo-actuated mirror in the pump path for stabilizing the squeezer to deamplification. We measured the open-loop gain to have a unity-gain frequency of 1.7 kHz (see appendix A.3).

The phase modulation of 20.9 MHz on the control field was also detected with the homodyne detector, demodulated by an external mixer and fed to a piezo-actuated mirror in the local oscillator path. This stabilized the homodyne detection readout phase by changing the local oscillator phase with respect to the squeezed field.

5.8.3. High detection efficiency measurement results

We performed a measurement using the in-house made high detection efficiency homodyne detector and stabilizing the squeezer's pump phase and the homodyne detection phase (see Fig. 5.17).

The experiment used a pump power of 230 mW, a local oscillator power of about 4 mW, an RBW of 3 MHz, a VBW of 1 kHz and a sweep time of 540 ms. We plotted an averaged dark-noise corrected spectrum from 5 MHz to 1.6 GHz, which was normalized to the vacuum noise level. The spectrum yielded a maximal squeezing value (red) of about 5.3 dB below 100 MHz and a maximal anti-squeezing of around 11 dB (blue) at low MHz frequencies. At 1 GHz sideband frequency the dark-noise corrected nonclassical noise suppression was about 3.5 dB, which was still around 3 dB without dark-noise correction.

Electronic pick-up peaks were indeed spoiling the spectrum as expected from the homodyne detector characterization (see section 5.8.1). Additionally, a feature in the squeezed and anti-squeezed spectrum at 900 MHz was visible. This was most likely also an artifact of the electronic circuit design.

We did not observe a higher squeezing value by further increasing the pump power. This was mainly due to the relative instability of the pump phase lock with increasing power and high thermal effects, limiting the available intra-cavity power.

Figure 5.18 depicts a loss calculation and suggests total optical loss of around 25% by using the highest squeezing and anti-squeezing values as a reference. The estimated initial squeezing value was about 12.3 dB in this case. This suggests a slightly increased homodyne detection visibility of about 91% with respect to the former measure-

5.8. High detection efficiency GHz bandwidth measurement

ment results. Based on this, one can indeed infer a quantum efficiency for the photodiodes of around 99 %.

An N.L.C.S. simulation using the total optical loss (25 %) and the resonator parameters is depicted as dashed lines in Fig. 5.17. The simulated spectra are again in good agreement with the measured data.

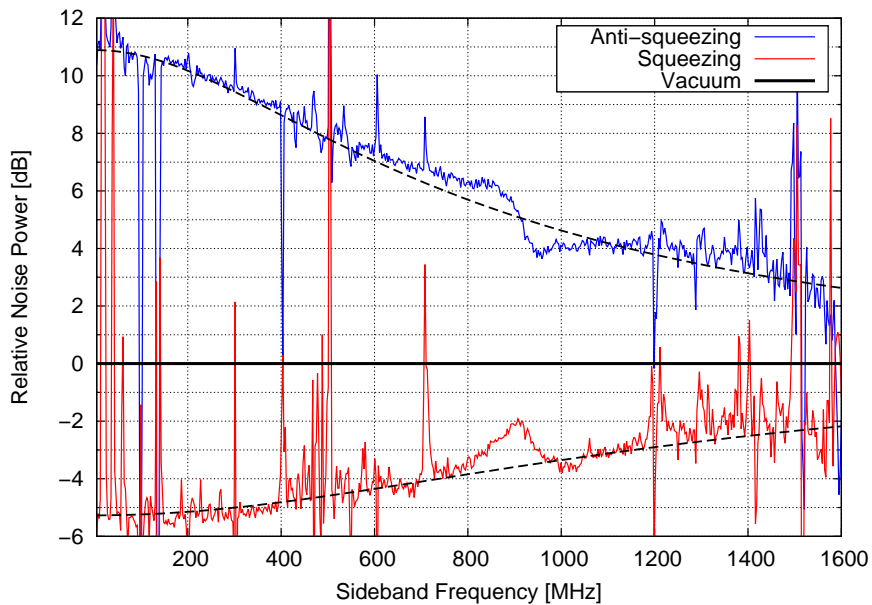


Figure 5.17.: Squeezing (red) and anti-squeezing (blue) spectra for the experiment with pump phase and homodyne detection phase stabilized. The measurements are normalized to the vacuum noise level and dark-noise corrected as well as averaged. A pump power of 230 mW and a local oscillator power of 4 mW were used. The maximally obtained squeezing is about 5.3 dB below 200 MHz and 3.5 dB at 1 GHz. Without dark-noise correction the squeezing was still 3 dB at 1 GHz.

5. High-bandwidth monolithic squeezing resonator

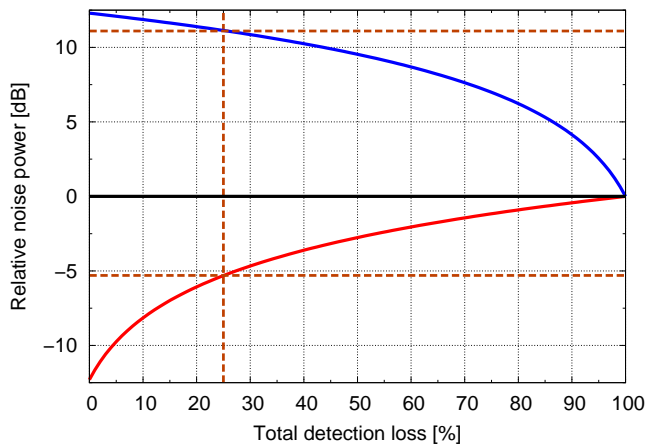


Figure 5.18.: Simulated total loss for the squeezing measurement with stabilized pump phase and homodyne detection phase. The simulation used an initial squeezing value of 12.3 dB at low MHz frequencies. A total optical loss of 25 % is deduced, with the main contribution of 18 % from the homodyne detection visibility, and the remaining 7 % assumed to be optical path loss.

5.9. Parasitic frequency doubling in the monolithic crystal

The crystal did not only generate a down-converted squeezed field at 1550 nm, but also up-converted the pump photons to the harmonic wavelength at 387.5 nm. This effect is due to the high intra-cavity pump power of some 72 W at 775 nm. A picture of the ultra-violet beam is depicted in Fig. 5.19. We had neither optics nor photo-detectors at this specific wavelength, so we could not properly analyze the frequency doubled light. The reason for the harmonic light generation was possibly a non-specified reflectivity at 387.5 nm for the squeezing resonator. So the crystal surfaces might have acted as a cavity for the ultra-violet light and thus favored a decay of 775 nm photons to 387.5 nm. This wavelength is specified to be outside the transparency window of the material. Thus the very high absorption on the order of 20 %/cm (KTP at 390 nm) potentially lead to grey-tracking of the crystal (for both see [67]) or thermal lensing inside the crystal. Blue light induced infrared absorption (BLIIRA see [68, 69]) might lead do additional loss for the squeezing at 1550 nm. For future experiments, the up-conversion to a harmonic light from the pump field has to be avoided to circumvent additional loss. A possibility

5.10. Path difference for high-bandwidth homodyne detection

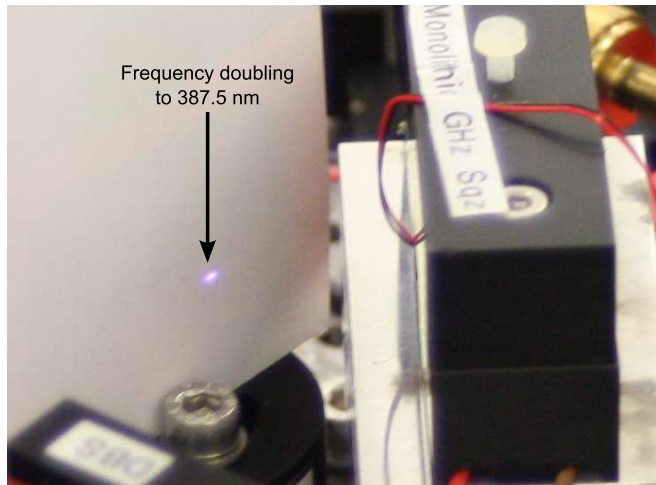


Figure 5.19.: Incidentally generated second harmonic light of the 775 nm pump field inside the squeezing resonator. This light had a wavelength of 387.5 nm and was made visible on a white sheet of paper due to the fluorescence effect of UV-light.

would be to have an anti-reflective coating at this specific wavelength. This highly reduces the resonant enhancement of the 387.5 nm field and decrease the decay probability from 775 nm to 387.5 nm photons.

5.10. Path difference for high-bandwidth homodyne detection

Another interesting effect observed in our experiment is related to measuring high sideband frequencies of the squeezed field. The non-classical light strongly degraded when using different optical lengths from the output ports of the homodyne detection beam splitter to the detector's photodiodes. This length difference changes the homodyne detection readout phase between the local oscillator (carrier frequency) and the signal field at a high frequency. The homodyne detector will measure the noise of the local oscillator instead of the squeezed noise, as explained in chapter 2.3.

We measured this effect by introducing a length difference of 27.5 cm after the homodyne beam splitter to the photodiodes (see Fig. 5.20). The squeezed and anti-squeezed noise is completely destroyed at a sideband frequency of 750 MHz and recovered at frequencies above 900 MHz. The measurement was performed with the *New Focus 1617-AC FS* homodyne detector from section 5.6.1.

5. High-bandwidth monolithic squeezing resonator

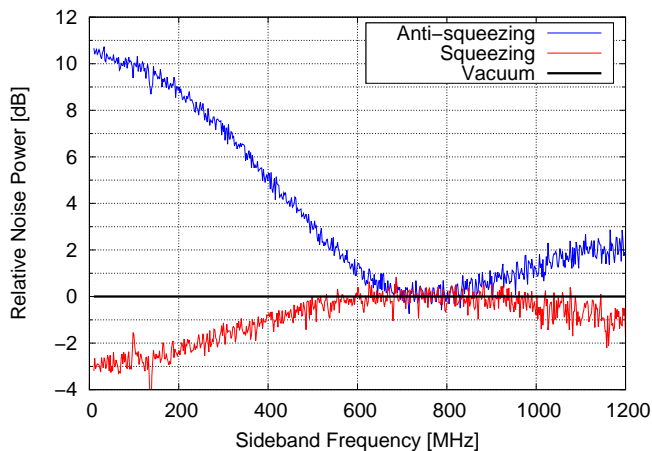


Figure 5.20.: Squeezed light measurement performed with the commercially available homodyne detector *New Focus 1617-AC FS*. We introduced a path length difference of 27.5 cm after the homodyne beam splitter to the photodiodes. The squeezing and anti-squeezing is degrading with increasing frequency and is reduced to vacuum noise level at about 750 MHz. Above 900 MHz and with increasing frequency the squeezing recovers again. Note that the squeezing at higher frequencies is naturally decreasing due to the finite cavity linewidth.

This effect has to be kept in mind when generating squeezed states at high sideband frequencies, especially when using two-mode squeezing in fiber-based QKD systems, where one part of the beam is transmitted through a long fiber.

5.11. Summary & Outlook

This chapter introduced a new design for a 2.6 mm long monolithic crystal cavity with an output coupling reflectivity for the fundamental squeezing wavelength of $R_{1550} = 64\%$. The reflectivity was chosen to obtain a maximum nonclassical noise suppression at 1 GHz by simulating the squeezed output with N.L.C.S.

In the experiment, the generation of a broadband squeezed state at 1550 nm ranging from 5 MHz to 1.6 GHz sideband frequency was realized. Three different homodyne detectors were used to perform consecutive measurements for different frequency bands. We used an optical parametric intra-cavity pump power of about 47-73 W for the squeezing generation. A commercially available balanced photo receiver directly observed squeezing of up to 2 dB between 10 MHz

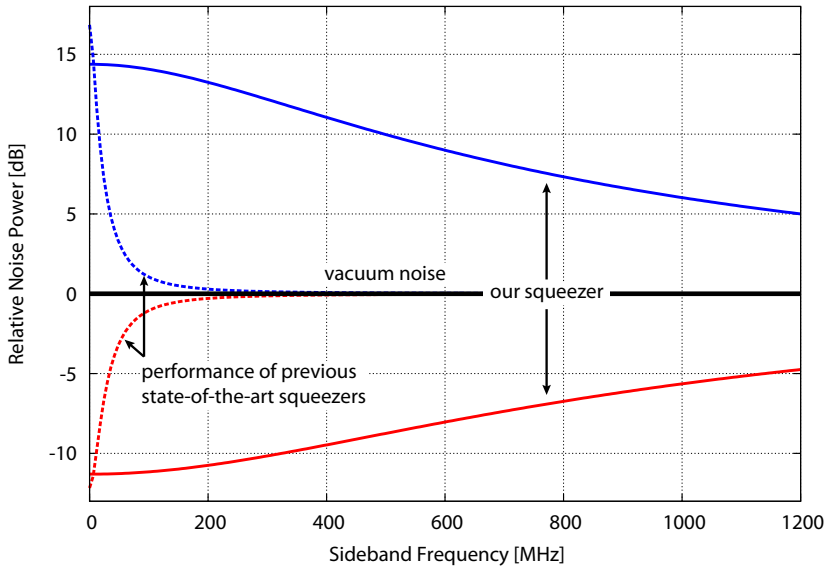


Figure 5.21.: N.L.C.S. simulations comparing a typical squeezing resonator as in [21] (dashed lines) and the monolithic GHz bandwidth squeezing resonator reported in this experiment (solid lines). Our simulation assumes a total detection efficiency of 0.96, as realized in [21] for both simulated spectra. The squeezing source reported here generates almost the same squeezing strengths as state of the art sources. However, it offers a 25-fold increase in bandwidth compared to typical squeezing resonators. [63]

and 1.2 GHz. The second measurement used an in-house made homodyne detector based on photodiodes with quantum efficiencies near unity but with a low measuring bandwidth. It detected a nonclassical quantum noise suppression of up to 4.8 dB from 5 to 100 MHz. The final measurement was performed with an in-house made GHz bandwidth homodyne detector using fast 70 μm active area photodiodes and 99% quantum efficiency. The pump phase and the homodyne detector phase were stabilized, which yielded a dark-noise corrected nonclassical noise suppression of 5.3 dB below 200 MHz and 3.5 dB at 1 GHz.

All three measured homodyne detector spectra were compared to numerical simulations using identical parameters, but with different quantum efficiencies for the detectors. The simulations are self-consistent and in very good agreement with the measurements.

5. High-bandwidth monolithic squeezing resonator

Based on our analysis, the measured squeezing was limited by the homodyne detector visibility (0.91), propagation loss (0.92) and partly by the quantum efficiencies of the photodiodes (0.99). This resulted in a total detection efficiency of about 0.75 (25% loss) for the final experiment.

We simulated our squeezing resonator setup with a total detection efficiency of 0.96 as achieved for low bandwidths in [21]. The simulation shows around 10 dB of nonclassical noise suppression at MHz frequencies and more than 5 dB at GHz frequencies (see Fig. 5.21). The simulation shows that our design of a monolithic squeezing resonator is feasible to be used as a high-bandwidth squeezed light source with a large squeezing factor in future experiments.

6

Chapter 6.

GHz bandwidth entanglement generation

6.1. Introduction

Entanglement based QKD in the continuous-variable regime can be realized via two-mode squeezed states of light. The two-mode squeezing is typically generated by overlapping two single-mode squeezed fields on a 50/50 beam splitter. The outputs of the beam splitter will then be entangled and can be used to distribute a quantum key between two homodyne detectors, often called Alice and Bob (see [40, 34]). As mentioned before, a high squeezing bandwidth would offer the advantage of a higher measurement speed, resulting in a higher robustness against decoherence and a higher secret key rate (see chapter 1).

Our goal in this chapter was a proof of principle experiment for generating high-bandwidth entangled states of light as a resource for QKD in the future. After successfully designing and testing the monolithic crystal squeezing resonator in the previous chapter, I implemented two of them for the generation of entanglement. The two-mode squeezing was detected via two homodyne detectors with GHz bandwidth and custom made photodiodes with a quantum efficiency of 99%. The measurements violated the Duan criterion for entangled states over a bandwidth of more than 1 GHz.

I will first describe the experimental setup and present the mode-matchings for the two squeezing resonators. Afterwards, I will characterize the subtraction of the two homodyne detectors. The entanglement measurement will be described in three parts: overlapping one squeezer with a vacuum state (“v-class”), overlapping two squeezers

6. GHz bandwidth entanglement generation

(“s-class”) and a calculation of the Duan value from the measurements. A discussion of the experimental results will be presented before the chapter will end with a short summary and an outlook.

6.2. Experimental setup

The experiment used an Ytterbium-doped fiber laser at 1550 nm from *NKT Photonics* type *Koheras AdjustiK* including an external fiber amplifier type *Koheras BoostiK* with 5 W output power. After passing through a Faraday isolator to prevent back coupling of the high laser power, a modecleaner resonator was length-stabilized to filter the laser’s TEM₀₀ mode and suppress amplitude- and phase noise. A small fraction of about 10 mW from the main laser beam was used as local oscillator for homodyne detection.

A schematic of the most important part of the experimental setup is depicted in Fig. 6.1. About 1 W of laser power was frequency doubled inside a second harmonic generation cavity similar to the one in chapter 3. The resulting 800 mW of 775 nm laser light were used as pump fields for two squeezing resonators. A modecleaner cavity filtered the frequency doubled field and acted as a diagnostic tool for mode-matching the 775 nm pump light to the squeezers. The MC is not shown in the picture for simplicity.

The experiment used two monolithic crystals of the type designed in chapter 5.3. A temperature controller stabilized both cavities on resonance and achieved quasi-phase matching for the nonlinear process. The outputs of both squeezed light sources were overlapped on a 50/50 beam splitter, thus creating entanglement. A piezo-actuated mirror shifted the phase of one of the squeezed beams in the path before the beam splitter. This enabled an adjustment of the two squeezing phases with respect to each other.

A homodyne detector in each output port of the beam splitter measured the two-mode entanglement. The homodyne signals were subtracted with a *Mini Circuits* power splitter and acquired with a spectrum analyzer. This gave access to the field variances for verifying the violation of Duan’s inequality (see equation 2.42).

The optical paths after the entanglement beam splitter as well as the path lengths between the homodyne beam splitters and the photodiodes were designed to be equal. This avoided a degradation of the entanglement strength at higher sideband frequencies (compare chapter 5.10).

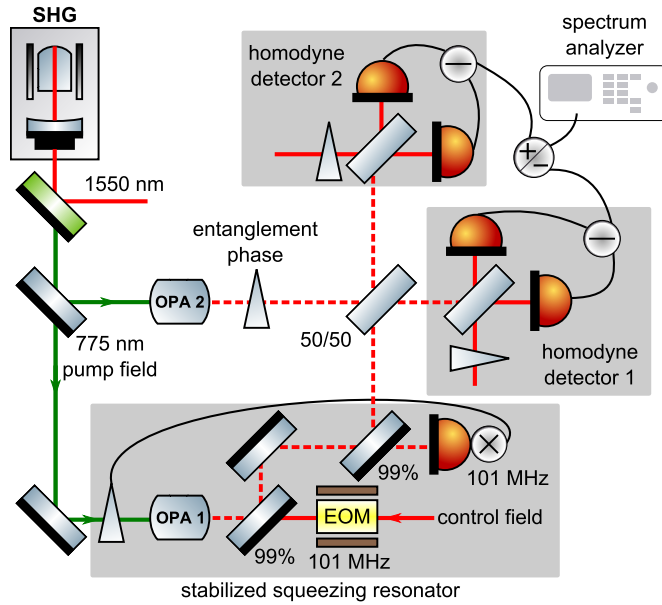


Figure 6.1.: Schematic setup for the GHz entanglement experiment. The two monolithic squeezing resonators (OPA1 & OPA2) were pumped by 775 nm light coming from a single second harmonic generation cavity (SHG). The cavity lengths for the squeezers were stabilized on resonance via temperature control. A control field was injected into OPA1 to stabilize the pump phase and the two homodyne detector phases. The squeezed outputs of OPA1 and OPA2 were overlapped on a 50/50 beam splitter. After subtraction of the two homodyne detector signals, a spectrum analyzer was used to acquire the field variances.

6.2.1. Stabilized homodyne detection

The experimental goal was to violate the “Duan criterion” for inseparability to verify the entanglement. This required a measurement of the variance of the difference and the sum of the two orthogonal quadratures $\text{Var}(\hat{X}_A - \hat{X}_B)$ and $\text{Var}(\hat{P}_A + \hat{P}_B)$ as explained in chapter 2.4.

To stabilize the homodyne detection readout, a control field of 50 mW at 1550 nm was coupled into OPA1 through a 99% mirror in the squeezed light path. An EOM applied a phase modulation of 101 MHz to the beam. This was used to first stabilize the relative pump phase and subsequently to stabilize the homodyne readout phase (compare chapter 5.8.2).

The first loop was controlling the relative phases between the pump field and the control field of the squeezing resonator via a piezo-actuated mirror. The pump phase was stabilized to parametric de-

6. GHz bandwidth entanglement generation

amplification of the control beam with a resonant photodetector in transmission of a 99 % mirror in the squeezed light path. This was necessary to turn the control field into a reference for the squeezed state.

Afterwards the readout phase of the homodyne detection was tuned to the required quadratures for the entanglement measurement. This was done via stabilizing the relative phases between the control field and the local oscillators after interference at the homodyne beam splitter.

The measurement of $\text{Var}(\hat{X}_A - \hat{X}_B)$ was performed by stabilizing both homodyne detectors to the squeezed quadrature of OPA1 with the demodulated error signal at 101 MHz. This error signal was picked off via a *Mini Circuits* power splitter at the AC output of the homodyne detectors.

The measurement of $\text{Var}(\hat{P}_A + \hat{P}_B)$ was acquired by stabilizing both homodyne detectors to the anti-squeezed quadrature of OPA1 with a DC-lock. One homodyne detector was stabilized to the inverted (-P) quadrature to realize the plus sign for this measurement.

6.2.2. Mode-matchings for OPA1 and OPA2

In this section, I will describe the mode-matching of the control and the pump fields to both squeezing resonators. The control field at OPA2 was later blocked for the entanglement measurements and was only used for adjusting the squeezed field. I used the same techniques as described in chapter 5.4.1 for the adjustment procedure.

The mode-matching for the control fields were performed in transmission of a 99 % mirror. The cavity lengths were tuned by actuating the crystal temperature via a Peltier-element. A photodetector in transmission of the crystal measured the mode spectra for squeezing resonator 1 (see Fig. 6.2a) and squeezing resonator 2 (see Fig. 6.2b). The mode-matching for the first squeezer was better than 95 %, while the mode-matching for the second squeezer was about 85 %.

The pump field mode-matchings were acquired by stabilizing the temperatures of the crystals to cavity resonance as well as to the quasi phase-matching conditions. The 1550 nm control field was thus converted to its second harmonic at 775 nm. The harmonic fields were then mode matched to a three-mirror modecleaner cavity in the pump path of the squeezing resonators. A piezo-actuated mirror was used to scan the length of the MC. The corresponding mode spectra were detected by a highly sensitive photodetector in transmission of the

modecleaner. I measured mode-matchings of more than 98% for the pump field of both squeezing resonators (see Fig. 6.3a & 6.3b).

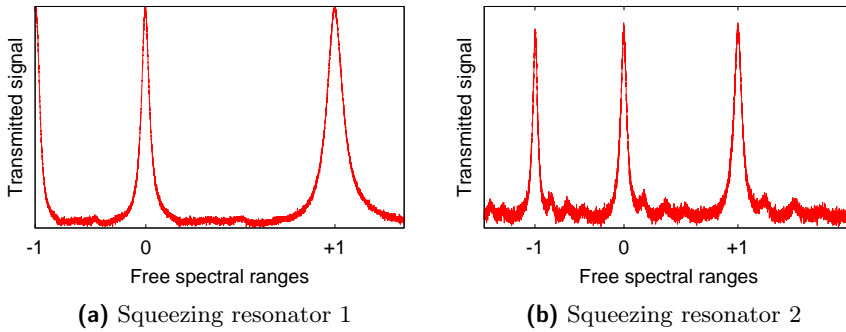


Figure 6.2.: Mode-matchings for the 1550 nm control field to both squeezing resonators. The measurements were performed in transmission of the monolithic resonator by heating the nonlinear crystal and thus changing the cavity's optical length. The mode-matching for squeezing resonator 1 (left) was about 95% and the mode-matching for squeezing resonator 2 (right) was about 85%.

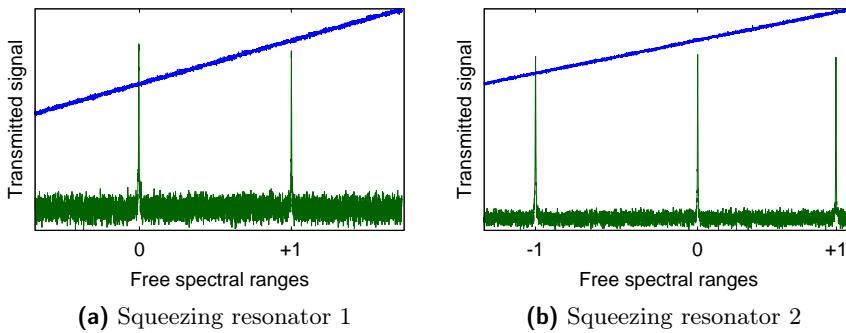


Figure 6.3.: Mode-matchings for the pump field at 775 nm to both squeezing resonators. The measurements were performed by frequency doubling the 1550 nm field in the nonlinear cavities and mode-matching the resulting 775 nm light to a modecleaner in their pump path. The plots show the ramp signal used to scan the MC cavity length (blue) and the transmitted signal of the 775 nm pump field (dark-green). The mode-matching for both cavities was better than 98%.

6. GHz bandwidth entanglement generation

6.2.3. Homodyne detector characterization

The experiment employed two identical homodyne detectors, which measured in the output ports of the entanglement beam splitter. The detectors consisted of custom made InGaAs photodiodes with an active area of $70\ \mu\text{m}$ and a quantum efficiency of 99% (see chapter 5.8.1). The AC paths contained two microwave amplification transistors, one of type *Mini circuits ERA-5XSM+* and one *Mini circuits MAR-6+* for the high frequency AC signal generation (see appendix Fig. A.6). The AC outputs of the detectors were split up in two parts by commercially available power splitters from *Mini circuits*. One part was used to extract error signals for locking the homodyne detector's phases as described in section 6.2.1. The remaining signals were subtracted by a *Mini circuits* power splitter type *ZFSCJ-2-4+* over a frequency range of 5-1600 MHz.

The red and blue lines in figure 6.4 show the vacuum noise levels

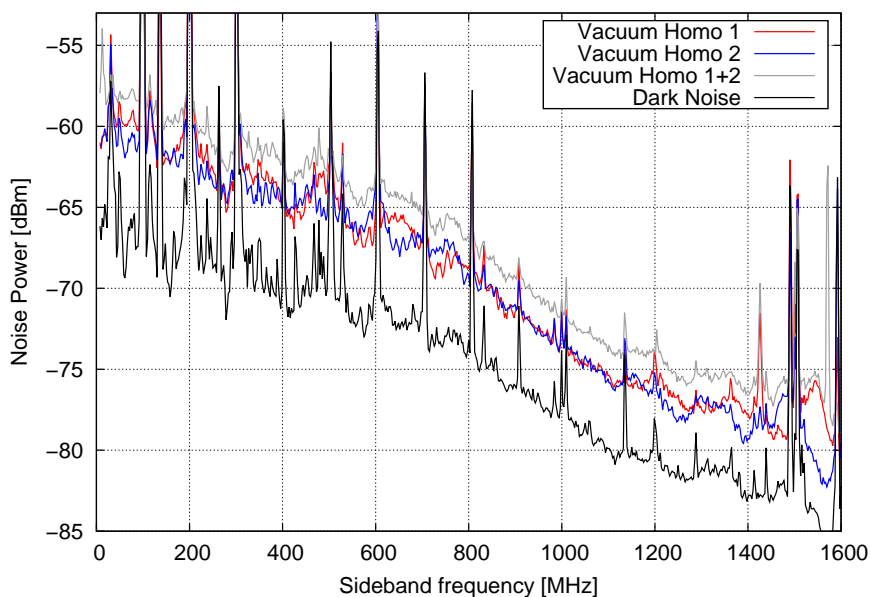


Figure 6.4.: Vacuum noise levels for 6 mW LO on homodyne detector 1 (red) and 5 mW LO power on homodyne detector 2 (blue) as well as the combined vacuum after the subtraction of the signals (gray). The spectrum was measured with an RBW of 3 MHz, a VBW of 1 kHz and a sweep time of 540 ms. The LO powers are adjusted such that the vacuum noise at the frequency range around 1 GHz is equal. The dark-noise clearance (black) of the subtraction for both homodyne detectors is around 6 dB at 1 GHz.

of both individual homodyne detectors. Their levels were measured to be slightly different. This was caused by different amplifications from the homodyne detector's electronic circuits, especially due to differing performances of the microwave amplifiers. I compensated for this effect by adjusting the local oscillator powers for both homodyne detectors, such that the vacuum noise levels around 1 GHz sideband frequency were equal. The local oscillator power for detector 1 was 6 mW, while the local oscillator power on detector 2 was 5 mW. Note that the vacuum noise of both detectors was still at different noise powers over large parts of the spectrum.

The combined vacuum noise of both detectors is depicted in gray (see Fig. 6.4) and shows a dark noise (black) clearance of 6 dB at 1 GHz. Electronic pick-up was visible at a variety of frequencies of the homodyne detector spectra and is explained in appendix A.4.

A more detailed characterization including a linearity check of the individual homodyne detectors is given in the appendix Figs. A.8 and A.9.

6.3. V-class entanglement measurement

The first measurement was performed with one of the squeezers blocked. This is often referred to as a “v-class” entanglement measurement. Here, the entanglement is created by overlapping a single mode squeezed beam with a vacuum state on a 50/50 beam splitter. As mentioned in section 6.2.1, X denotes the squeezed (amplitude) quadrature, while P denotes the anti-squeezed (phase) quadrature of OPA1.

A measured v-class entanglement spectrum of squeezing resonator 1 is depicted in Fig. 6.5, while the v-class spectrum normalized to the vacuum noise level is plotted in Fig. 6.6. I blocked the signal paths to measure the vacuum noise (gray) using 6 mW (5 mW) of local oscillator power for homodyne detector 1 (homodyne detector 2). The entanglement measurements used 210 mW of pump power at 775 nm and 500 μ W of control field power at 1550 nm for the squeezing resonator. The spectra were detected from 5 MHz to 1.6 GHz sideband frequency. Some noise peaks from the phase modulated sidebands at 101 MHz and their harmonics are visible across the whole frequency band. They slightly degrade the spectrum but were necessary for the phase stabilization of the homodyne detectors.

In red the homodyne detection phases were stabilized to measure the

6. GHz bandwidth entanglement generation

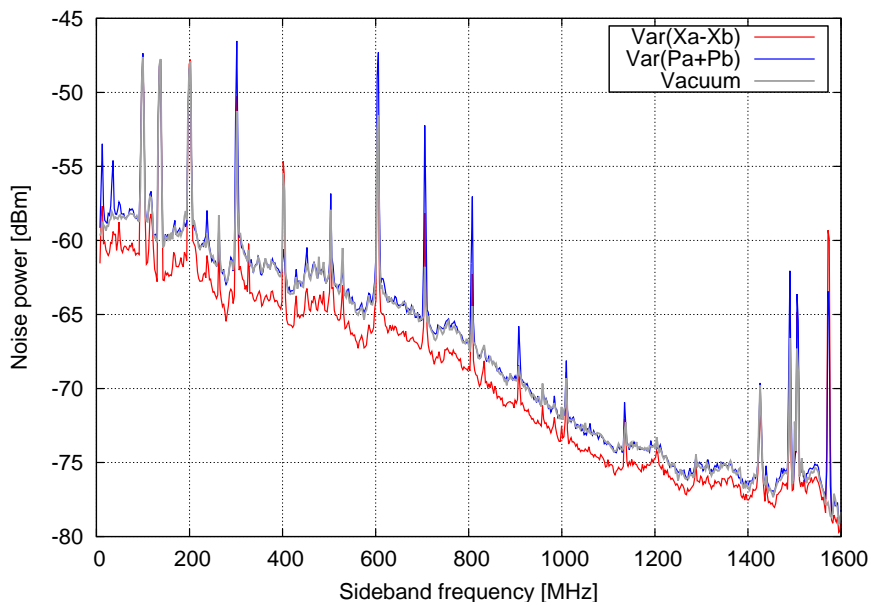


Figure 6.5.: V-class entanglement spectra for squeezing resonator 1. I used a pump power of 210 mW and a local oscillator power of 6 mW (5 mW) for homodyne detector 1 (homodyne detector 2). The homodyne detectors measured $\text{Var}(\hat{X}_A - \hat{X}_B)$ (red) and $\text{Var}(\hat{P}_A + \hat{P}_B)$ (blue) as well as the combined vacuum noise (gray) from 5-1600 MHz sideband frequency. A spectrum analyzer used an RBW of 3 MHz, a VBW of 1 kHz and a sweep time of 540 ms to compute the depicted variances.

squeezed quadrature with both detectors. This corresponds to a measurement of $\text{Var}(\hat{X}_A - \hat{X}_B)$ and shows a maximal nonclassical noise suppression of about 2.4 dB at 150 MHz and 1.4 dB at 1 GHz, respectively.

I measured the blue curve by stabilizing both homodyne detection phases to the anti-squeezed quadrature. This corresponds to a measurement of $\text{Var}(\hat{P}_A + \hat{P}_B)$. The anti-squeezed quadratures effectively cancel each other due to the negative phase flip at the entanglement beam splitter, while the vacuum adds up. In total the measured variance drops to the vacuum level.

In summary the v-class entanglement detects one quadrature measurement below the vacuum noise, while the orthogonal quadrature is exactly at the vacuum noise level.

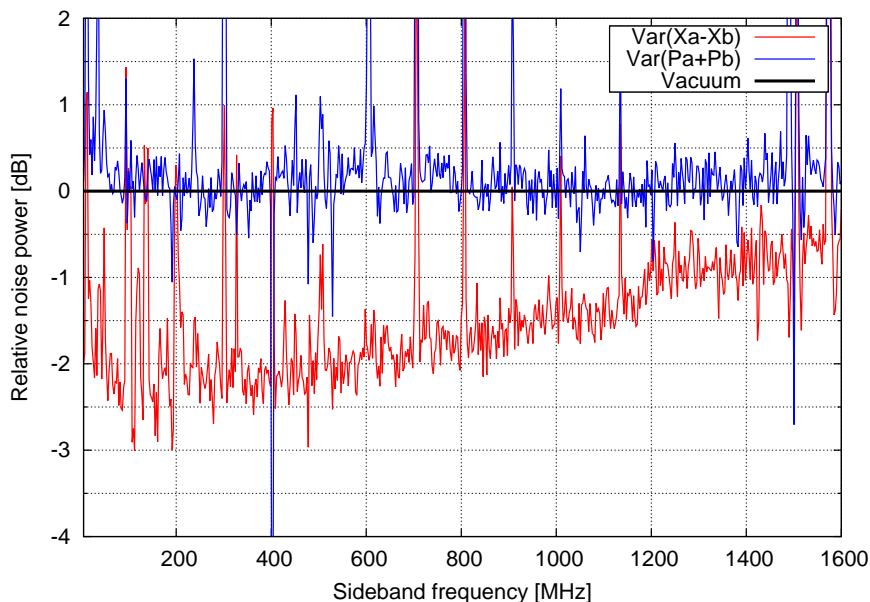


Figure 6.6.: V-class entanglement spectra from Fig. 6.5 normalized to the vacuum noise level (black). In red $\text{Var}(\hat{X}_A - \hat{X}_B)$ shows a maximal nonclassical noise suppression of 2.4 dB at 150 MHz and around 1.4 dB at 1 GHz. In blue the variance of the sum for the orthogonal quadratures $\text{Var}(\hat{P}_A + \hat{P}_B)$ is depicted.

6.4. S-class entanglement measurement

The so called “s-class” measurement uses two (or more) single-mode squeezed light sources to create entanglement. The squeezed fields are overlapped on a 50/50 beam splitter with a phase difference of 90° . Regarding the phase space picture, the squeezing ellipses thus are orthogonally oriented at the beam splitter. By detecting the variances of the difference of the amplitude quadratures [$\text{Var}(\hat{X}_A - \hat{X}_B)$] and the sum of the phase quadratures [$\text{Var}(\hat{P}_A + \hat{P}_B)$] one can observe a nonclassical noise suppression below the combined vacuum noise.

I measured an s-class entanglement spectrum from 5-1600 MHz sideband frequency using 230 mW of pump power and 6 mW (5 mW) of local oscillator power (see Fig. 6.7). Figure 6.8 depicts a spectrum normalized to the vacuum noise level. All spectra were averaged using two consecutive measurements. The peaks showing up in all measurements are again mainly due to the control field’s phase modulation at 101 MHz, which was used to stabilize the homodyne phases.

6. GHz bandwidth entanglement generation

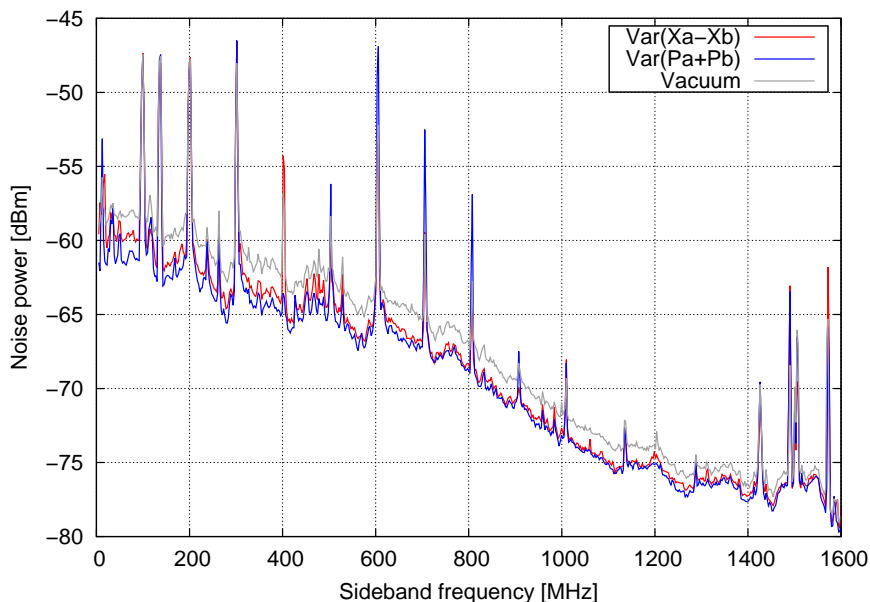


Figure 6.7.: S-class entanglement spectra from 5-1600 MHz measured via homodyne detection. I used a pump power of 230 mW for both squeezing resonators, a local oscillator power of 6 mW (5 mW) for homodyne detector 1 (homodyne detector 2), an RBW of 3 MHz, a VBW of 1 kHz and a sweep time of 540 ms. Both spectra were averaged twice by measuring two consecutive spectra for each quadrature.

The homodyne detector phases were stabilized to the control field of squeezer 1, which also defined the orientation of the quadratures. A piezo-actuator shifted the phase in squeezing path 2 and tuned it to be orthogonal to squeezer 1.

The red lines in the plots show a measurement of $\text{Var}(\hat{X}_A - \hat{X}_B)$ (see Figs. 6.7 & 6.8). The homodyne detectors effectively observed the squeezing of the stabilized squeezer 1, while the anti-squeezing of squeezer 2 was canceled. I measured a nonclassical noise suppression over a frequency range of about 1600 MHz, with a maximum of 1.8 dB at 100 MHz and about 1.3 dB at 1 GHz below the combined vacuum noise (black).

The blue lines in Fig. 6.7 and 6.8 show a measurement of $\text{Var}(\hat{P}_A + \hat{P}_B)$, which is acquired by stabilizing the homodyne detectors to the anti-squeezing of squeezer 1. However, the anti-squeezing was canceled at the two readouts due to the phase flip at the entanglement beam splitter (see section 6.3). A piezo-actuator in the beam path of squeezer 2 was manually tuned to observe the squeezed quadrature. The sec-

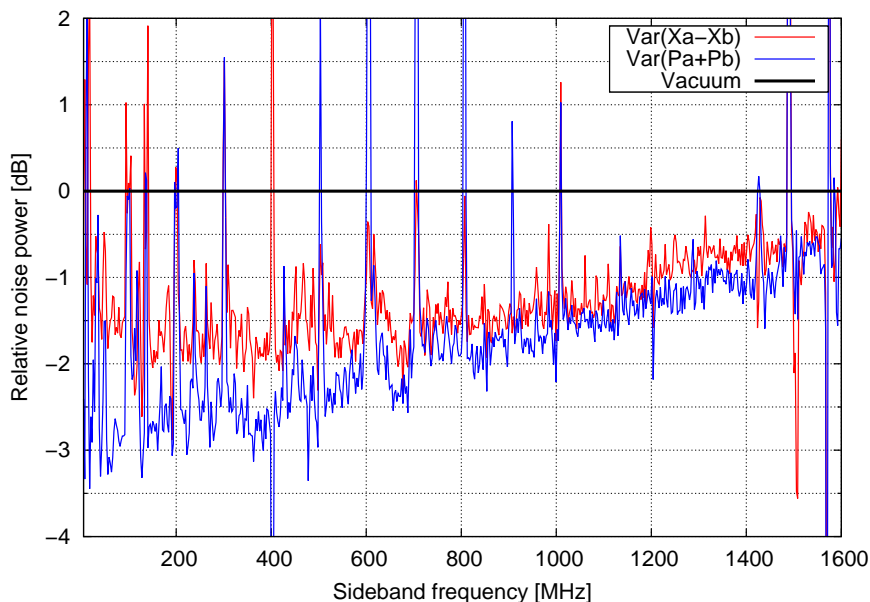


Figure 6.8.: S-class entanglement spectra from Fig. 6.7 normalized to the vacuum noise. The measurement of both orthogonal quadratures showed a nonclassical noise suppression with a maximum of around 2.8 dB at 100 MHz for $\text{Var}(\hat{P}_A + \hat{P}_B)$. At 1 GHz the quadrature measurements yielded 1.3 dB for $\text{Var}(\hat{X}_A - \hat{X}_B)$ and 1.6 dB for $\text{Var}(\hat{P}_A + \hat{P}_B)$. The dark-noise clearance was around 9 dB at 100 MHz and 6 dB at 1 GHz, which resulted in dark noise limited measurement spectra (see section 6.5).

ond quadrature also yielded a nonclassical noise suppression over a frequency range of about 1600 MHz, with a maximum of 2.8 dB at 100 MHz and about 1.6 dB at 1 GHz below the combined vacuum noise (black).

The combination of the two quadrature measurements demonstrates the broadband entanglement from 5-1600 MHz sideband frequency.

6.4.1. Duan criterion spectrum

The measurement data of the s-class entanglement spectra were used to calculate the quantum state inseparability via the Duan criterion (see chapter 2.4). I will explain how to translate the criterion to the measured data in our experiment.

The Duan criterion was developed to define a measure of the entanglement strength for continuous-variable states [44]. In the special

6. GHz bandwidth entanglement generation

symmetric case of our setup it reads

$$\text{Var}(\hat{X}_A - \hat{X}_B) + \text{Var}(\hat{P}_A + \hat{P}_B) \geq 1.$$

Here, the vacuum for one detector is normalized to $\frac{1}{4}$ and thus the threshold of 1 denotes two times the combined variance of the vacuum. Note that the two homodyne detectors measure two orthogonal quadratures in consecutive measurements. A violation of the inequality is a measure of the inseparability of the state, with zero being a perfectly entangled state.

As an intuitive explanation, the sum of the two orthogonal variances has to be smaller than the sum of the combined vacuum noise. Thus an overall nonclassical noise suppression below the total vacuum is achieved.

The measurement shows this behavior with a few exceptions at the modulation peaks. The calculated spectrum violated the Duan criterion over the whole frequency range of 5-1600 MHz. Its value at 1 GHz was 0.75 and a minimal value of around 0.6 was achieved for low MHz frequencies (see Fig. 6.9).

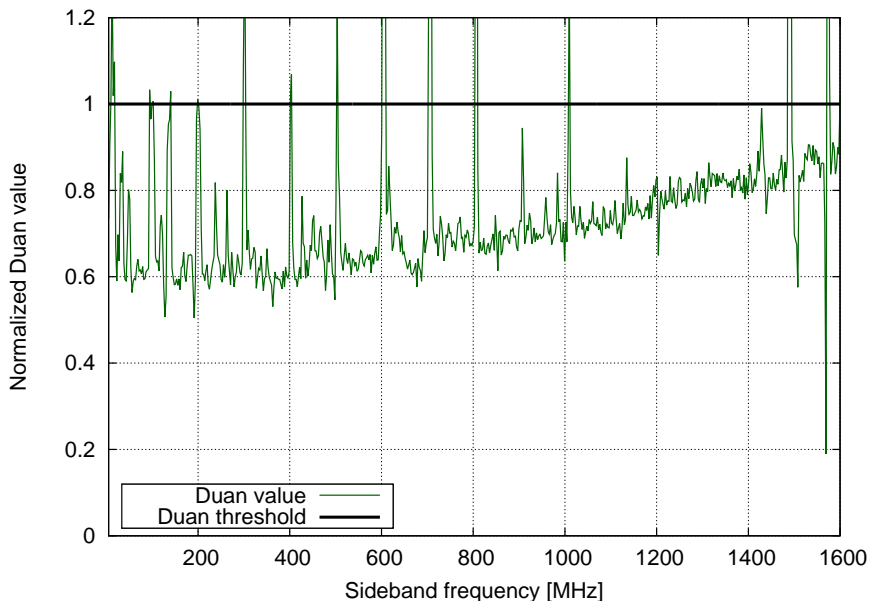


Figure 6.9.: Calculated Duan value for the sum of both quadratures' variances $\text{Var}(\hat{X}_A - \hat{X}_B) + \text{Var}(\hat{P}_A + \hat{P}_B)$ (green) with respect to twice the combined vacuum noise level (black). Duan's inequality was violated over the whole spectrum with a value of about 0.6 at 200 MHz and 0.75 at 1 GHz sideband frequency.

6.5. Discussion of the total detection loss

The v-class and s-class entanglement measurements yielded a much lower two-mode squeezing value than expected from the squeezing measurement in the previous chapter 5.8.3. I will give an overview of the possible reasons and solutions to the problems.

Optical loss from mirrors & lenses

The two-mode squeezed fields were using more optics compared to the single-mode squeezing experiment and thus suffered from more optical loss. In this case the additional loss channels were the entanglement beam splitter, mode-matching lenses for the overlap of the single-mode squeezers and additional steering mirrors.

In principle the path lengths can still be optimized to achieve lower optical loss. However, it will inevitably be higher for detecting two-mode squeezing.

Homodyne detection visibility

One loss source was encountered in chapter 5.5. It was difficult to adjust the homodyne detection visibility for the monolithic crystal cavities due to a deformation of the control field mode. Using two of these monolithic resonators increases the effect of this imperfection. Their control beams were neither good references for mode matching on the entangling beam splitter, nor were they helpful for adjusting the visibilities of the two homodyne detectors. The contrasts of both homodyne detectors and the contrast at the entanglement beam splitter have to be taken into account as $\eta_{\text{total}} = \eta_{\text{homo}}^2 \cdot \eta_{\text{ent-bs}}$ with the η denoting the contrasts. The square at the homodyning efficiency is introduced solely from the calculation of the variance by the spectrum analyzer. This can be derived from the calculations in [70]. With the estimated individual contrasts of below 90 %, the total detection efficiency for the s-class measurement was well below 72 %. However, the total detection efficiency for the v-class measurement was around 81 %, since the contrast at the entanglement beam splitter was intrinsically 100 %. The different losses for the v-class and s-class were visible in the measured spectra (see Figs. 6.6 & 6.8). A maximum squeezing value of 2.4 dB was measured using resonator 1 for v-class entanglement, while a maximum squeezing value of 1.8 dB was measured using the same resonator for s-class entanglement.

6. GHz bandwidth entanglement generation

Homodyne detectors dark-noise clearance

The dark-noise clearance for the given local oscillator power was only 9 dB at 100 MHz and 6 dB at 1 GHz for the subtraction of both homodyne detectors. The entanglement spectra were therefore dark noise limited.

Using power splitters with different splitting ratios to extract the error signals in the detector's AC outputs will enhance the dark-noise clearance. The experiment was performed with 50/50 splitters, effectively introducing 50 % of signal loss.

Different gain for the homodyne detectors

The measured vacuum noise levels for both homodyne detectors were not equal over the whole frequency band. This was because both electronic circuits had different frequency dependent gain profiles, although they were built to be identical. In particular, the microwave amplifiers (*Mini circuits MAR-6+* and *ERA-5XSM+*) did not have exactly the same amplification over the entire spectrum. The effect is clearly visible in Fig. 6.4, where the spectra of the individual homodyne detectors were compared for all frequencies.

A different gain at both detectors prevents an optimal cancellation of the anti-correlated noise in the subtraction of the two homodyne measurements.

A solution to this would be to use industrially produced homodyne detectors, which really show identical amplification and are optimized for microwave frequency measurements.

Phase relation at the entanglement beam splitter

The entanglement phase was not stabilized in the experiment and the homodyne and pump phase locks were quite unstable due to impedance matching problems and electronic cross-coupling. This is a potential source of phase noise, which in general decreases the measured squeezing. This problem has to be addressed especially when the high bandwidth entanglement is used as an application in quantum key distribution systems.

Total detection loss

The overall detection loss for the individual squeezing resonators and for the combined two-mode squeezing was difficult to estimate. How-

ever, the limitation to the maximal entanglement value of around 3 dB suggested a total loss of about 50 %.

6.6. Summary & Outlook

The experimental results in this chapter serve as a proof of principle for the generation and detection of entangled states of light with GHz bandwidth.

I generated bipartite entangled states of light at 1550 nm by overlapping two single-mode squeezed fields on a beam splitter. The squeezing was generated via parametric down conversion in two identical monolithic PPKTP crystal cavities. Two fast homodyne detectors measured the entanglement with around 1.6 GHz bandwidth. The experimental results yielded a minimal Duan-value of about 0.6 (0.75 at 1 GHz) with a Duan-threshold of 1 for separable states. The experiment was limited by optical loss, unequal electrical amplification for the homodyne detection, insufficient pump power (see chapter 5.8.3), low dark-noise clearance and possibly phase noise. The total detection loss was estimated to be 50 %.

A further optimization of the individual squeezing resonators and the overall setup will likely enable the detection of 10 dB entanglement with GHz bandwidth (compare chapter 5.11). The measured two-mode squeezing values are in principle already suitable for entanglement based QKD. However, an implementation of our source into the experiment of Eberle [34] is technically difficult due to the high switching rate necessary. More importantly, the experiment in this thesis did not violate the EPR-criterion [71] mandatory for the QKD protocol used by Eberle [72]. Nevertheless, the experiment marks a first step towards high data rate quantum key distribution via two-mode squeezed states of light with potential applications in urban networks in the near future.

7

Chapter 7.

Squeezed light generated via the cascaded Kerr effect

7.1. Introduction

The previous chapters gave a description of experiments to generate squeezed and entangled states of light via the effect of optical parametric amplification. Here, we will exploit a different method for the generation of squeezed light: the cascaded Kerr effect.

Optical parametric amplification is a solely second order nonlinear effect. The cascaded Kerr effect is a second order nonlinear effect mimicking the third order nonlinear Kerr effect (see chapter 2.5.2). The Kerr effect possesses some distinct advantages and disadvantages compared to the OPA effect:

1. The Kerr effect does not need a frequency doubled pump field. A field at the fundamental wavelength acts as the driving field for the nonlinear process. It has the advantage of a simpler overall experimental setup, but the fact that the pump field is also present on the squeezed vacuum is disadvantageous. Both have to be separated from each other.
2. A drawback for the generation of Kerr squeezing is that the necessary pump power is considerably higher than the pump power for typical OPA squeezers with MHz bandwidths. In the given experiment the intra-cavity pump power was of the order of 15-30 W, which is the same order of magnitude as the pump power

7. Squeezed light generated via the cascaded Kerr effect

for the monolithic squeezing resonator with GHz bandwidth in the previous chapters.

3. The Kerr effect offers the outstanding possibility of generating non-gaussian states in the continuous variable regime (see [73]). Although the squeezing strength to produce a non-gaussian state is presumably in the order of 15 dB and even higher making it an extremely challenging task.

The third point in particular provides an intriguing motivation for the generation of squeezed states using the cascaded Kerr effect. This effect has never been experimentally demonstrated so far, and therefore offers a unique tool for the investigation of fundamental quantum phenomena (see chapter 2.5.2). The goal of the experiment was, however, a first proof of principle for the generation of squeezed light via the cascaded Kerr effect at 1550 nm.

The chapter will first introduce the overall concept of the experiment, which differs significantly from the squeezed light setups in the previous chapters. The new bow-tie squeezing resonator design will be discussed and I will explain the squeezed sideband extraction method via a modecleaner cavity. I will explain the experimental setup and give a characterization of the cascaded Kerr squeezing resonator with measured squeezing spectra. To the best of my knowledge, this is the first experimental demonstration of a cascaded Kerr effect generating a nonclassical noise reduction. The limitations of the measured squeezing will be discussed with the focus on optical loss. I will conclude the chapter with a summary and an outlook.

The experiment was performed in collaboration with A. Pal Singh and was part of his master thesis (see [74]). It will be discussed in more detail in a paper currently under preparation and in his PhD thesis.

7.2. Designing the Kerr squeezing experiment

Previous experiments for the generation of continuous-wave squeezed light via the cascaded Kerr effect did not achieve a nonclassical noise suppression (see [75, 76, 77]). This was due to technical noise showing a $1/f$ behavior and thus spoiling the vacuum noise within the measurement band of the squeezed light around 5 MHz. However, the presence of a cascaded Kerr effect was verified in these experiments by observing the suppression of technical noise.

Our conceptual design principle for the Kerr squeezing resonator

7.2. Designing the Kerr squeezing experiment

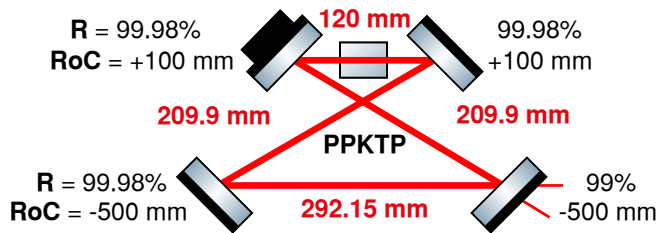


Figure 7.1.: Schematic design of the bow-tie type Kerr squeezing resonator. The total optical length is about 840mm including the PPKTP crystal's refractive index of 1.816 for 1550 nm.

aimed at measuring at high sideband frequencies in the range of several hundred MHz up to some GHz to avoid most technical noise sources. The high necessary pump field powers for the cascaded Kerr effect demanded a large power enhancement factor (finesse) in the cavity. However, the large finesse restricted the cavity linewidth and thus squeezing bandwidth to very low frequencies. We circumvented the problem of a high frequency readout by measuring at higher free spectral ranges of the squeezing resonator (compare [78]).

We used a 83.2cm long bow-tie resonator as squeezed light source, with a high power enhancement factor of about 382 for the 1550 nm pump field and a free spectral range of 358.3 MHz (see section 7.2.1 for details). The cavity's finesse for 775 nm was chosen to be small to suppress a parasitic frequency doubling to this wavelength. A second harmonic conversion in a cascaded Kerr nonlinear resonator would have acted as a loss channel for the squeezed field.

An off-resonant modecleaner cavity separated the remaining pump field at the carrier frequency of the squeezer from the squeezed sidebands (see section 7.2.2 for details). In transmission of the modecleaner, the squeezed sidebands were detected via homodyne detection at multiple free spectral range frequencies (358.3 MHz and 1074.9 MHz).

7.2.1. Kerr squeezing resonator design

A schematic of the resonator design is depicted in Fig. 7.1. The cavity was a bow-tie type resonator with a geometrical length of 832 mm using a 10 mm long PPKTP crystal ($n_{1550} = 1.816$) as the nonlinear medium. We measured the absorption of PPKTP to be $\alpha_{1550} = 84 \pm 40$ ppm/cm at 1550 nm in [56] and estimated its effective

7. Squeezed light generated via the cascaded Kerr effect

nonlinearity to be $d_{\text{eff}} = 7.3 \text{ pm/V}$. The end surfaces of the crystal were anti-reflection coated ($\text{AR} \leq 0.05 \%$). The four mirror's reflectivities were $R_{1-3} = 99.98 \%$, and $R_{\text{outcouple}} = 99 \%$ at 1550 nm . The corresponding cavity finesse at 1550 nm was about 590 with a free spectral range of 358.3 MHz and a linewidth as narrow as $\text{FWHM} = 600 \text{ kHz}$. Two of the cavity's mirrors were plano-concave with radii of curvature of -500 mm , while the other two mirrors were plano-convex with radii of curvature of $+100 \text{ mm}$, respectively. The waist size inside the PPKTP crystal was accordingly as small as $w_{1550} = 30.5 \text{ }\mu\text{m}$. The four mirror's reflectivities at the harmonic wavelength of 775 nm were $R_{1-4} = 20 \%$ to suppress the generation probability of a frequency doubled field with a low finesse.

The cavity possessed an acrylic glass housing with shock absorbing material to reduce air fluctuations and acoustic noise. The PPKTP crystal was housed in an oven construction with the temperature stabilized to about 70° C via a Peltier-element. This temperature was chosen to be on phase mis-matching and thus highly reduced the SHG effect. More importantly, it was stabilized to achieve the highest pos-

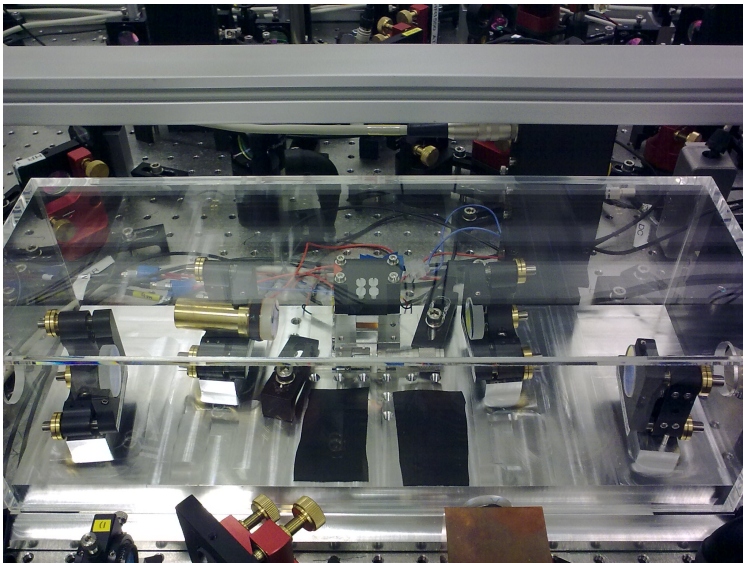


Figure 7.2.: Picture of the Kerr squeezing bow-tie resonator showing the aluminum baseplate, the mirror mounts from *New Focus* (left and right) and the oven construction for the PPKTP crystal (center). An acrylic glass housing was placed on top of the cavity to reduce air pressure fluctuations. A shock absorbing material was glued to the housing but is not present in this photograph to allow the interior of the cavity to be seen.

7.2. Designing the Kerr squeezing experiment

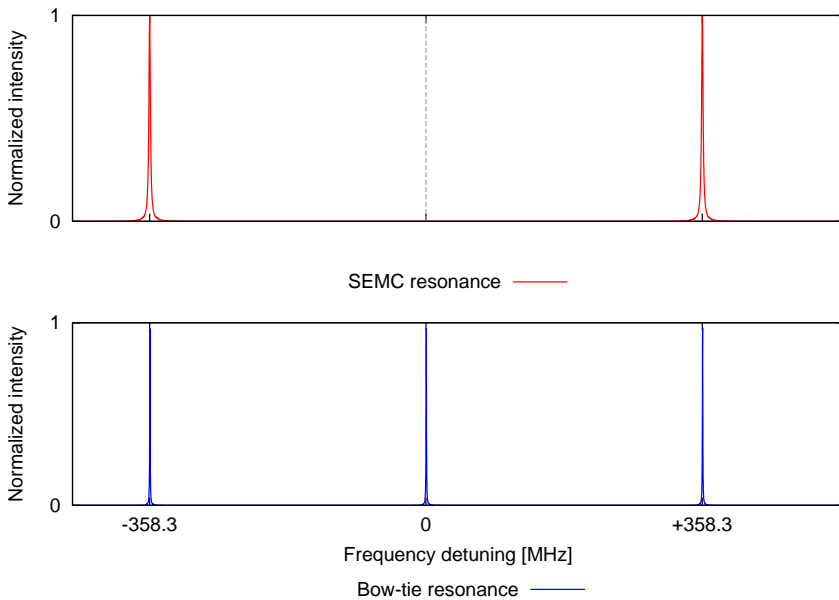


Figure 7.3.: Free spectral range comparison of the Kerr squeezing bow-tie resonator (bottom) and the sideband extraction modecleaner (top). The cavity lengths are adjusted such that the FSR of the SEMC is exactly twice the frequency of the bow-tie. For measuring the squeezed sidebands at 358.3 MHz, the bow-tie is stabilized to the fundamental resonance at 0 Hz. The squeezing is generated on the resonance frequency as well as on all further FSRs (358.3 MHz, 716.6 MHz, 1074.9 MHz,...). By holding the SEMC in the center of its FSR (dotted dark-grey line), the squeezed sidebands at 358.3 MHz and 1074.9 MHz are transmitted through the cavity, while the bright carrier is off-resonant and thus reflected.

sible cascaded Kerr effect at the minimum of second harmonic generation (see chapter 2.5.2).

A photograph of the quasi-monolithic bow-tie resonator without the shock absorbing material is shown in Fig. 7.2. More photographs and an schematic view of the CAD drawing of the cavity design are depicted in appendix A.6.

7.2.2. Sideband extraction modecleaner concept

Two parts contributed to the output of the bow-tie squeezing resonator in reflection: The bright pump field at 1550 nm with about 40 mW at the carrier frequency and the squeezed field inside the cavity linewidth expanding to frequencies at its free spectral ranges. A detection of the squeezed field at the initial resonance frequency was

7. Squeezed light generated via the cascaded Kerr effect

not possible due to the high pump field intensity (carrier) and the low squeezing bandwidth (600 kHz). The squeezed light was instead measured at the bow-tie cavity's free spectral ranges of 358.3 MHz and 1074.9 MHz.

We designed a three-mirror ring cavity to separate the squeezed sidebands from the bright carrier. This sideband extraction mode-cleaner (SEMC) had a free spectral range of 716.6 MHz, exactly twice the bow-tie resonator's frequency. Its full width at half maximum (FWHM) was about 1.2 MHz. The remaining pump field (carrier) on the squeezed beam was thereby reflected off the SEMC, while the squeezed vacuum sidebands were transmitted through the cavity by holding it in the center between two resonance peaks. Further details are given in the caption of Fig. 7.3.

7.3. Experimental setup

A schematic of the experimental setup is shown in Fig. 7.4. The experiment used the Ytterbium-doped fibre laser at 1550 nm from *NKT Photonics* type *Koheras AdjustiK*, including an external fiber amplifier type *Koheras BoostiK* with 5 W output power from chapter 6.2. After transmission through a three-mirror ring cavity as pre-modecleaner, the beam was split to serve as a pump beam for the bow-tie resonator and as a local oscillator for the homodyne detection. An EOM imprinted phase modulation sidebands on the laser in the pump field path at 101 MHz for a Pound-Drever-Hall stabilization of the bow-tie resonator. The light reflected from the bow-tie resonator was used to stabilize the cavity length with a photodetector in transmission of a 99 % mirror. The output of the squeezing resonator consisted of the fundamental pump field's carrier as well as the squeezed sidebands. A three-mirror modecleaner cavity (SEMC) separated the squeezed sidebands from the bright carrier (see section 7.2.2). The SEMC was manually tuned to the center between two adjacent free spectral ranges for s-polarisation. A homodyne detector with GHz bandwidth and high-efficiency photodiodes (see chapter 5.6.1) detected the vacuum squeezing in transmission of the SEMC at 358.3 MHz and 1074.9 MHz.

7.3.1. Bow-tie & SEMC mode-matchings

The fundamental pump field at 1550 nm was mode-matched to the bow-tie resonator with about 96 % input efficiency (see Fig. 7.5a).

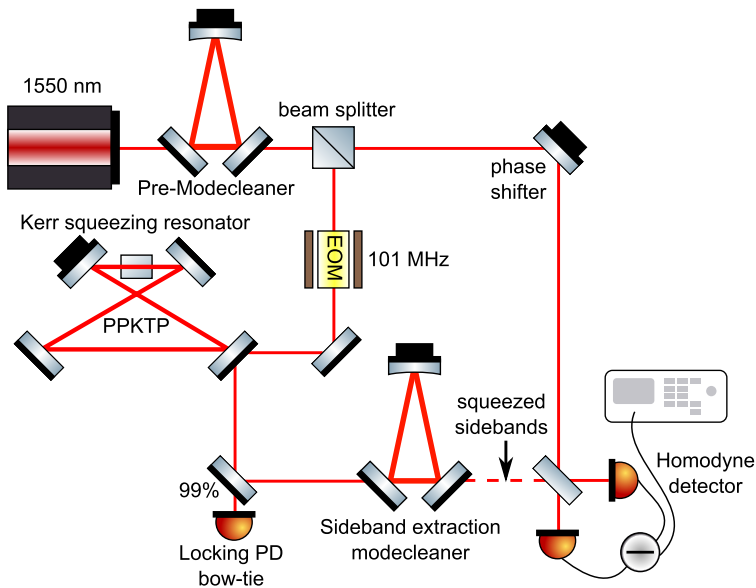


Figure 7.4.: Schematic of the experimental setup for Kerr squeezing. EOM: electro-optic modulator imprinting a phase modulation of 101 MHz to the beam to stabilize the bow-tie via PDH; Locking PD bow-tie: photodetector for the bow-tie cavity’s length stabilization; Sideband extraction modecleaner: three-mirror ring cavity to separate the squeezed sidebands at subsequent FSRs from the bright carrier.

The mode-matching was mainly limited by the elliptical eigenmode shape in the bow-tie resonator due to an astigmatism of about 8 % for the designed cavity.

The reflected carrier including the squeezed sidebands was mode-matched to the SEMC with an estimated efficiency of 98 % (see Fig. 7.5b). The mode-matching to the SEMC was crucial in order to minimize loss on the squeezed field in transmission of the cavity, since a mode mismatch directly translates to loss for the squeezing measurement.

7.3.2. Homodyne detector visibility

We measured the homodyne detector visibility by overlapping the local oscillator field at the homodyne detection beam splitter with a control field transmitted through the SEMC. The SEMC was therefore stabilized to resonance via PDH locking technique. Both beams were adjusted to have the same optical power. A piezo-actuated mirror in the local oscillator path continuously shifted the relative phases

7. Squeezed light generated via the cascaded Kerr effect

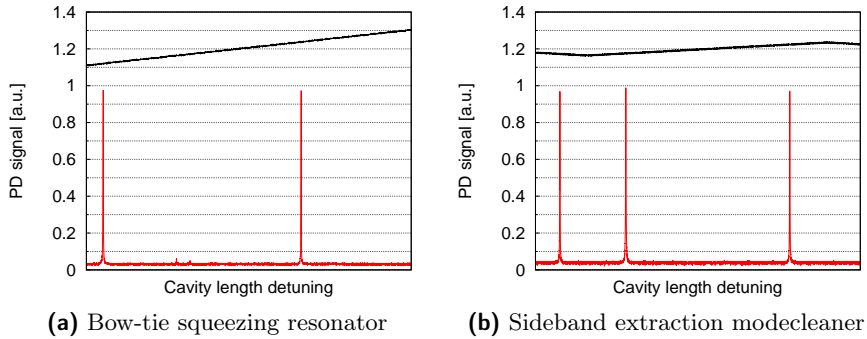


Figure 7.5.: Mode-matchings of both resonators measured in transmission. The red lines shows the mode scan with a ramp signal (black) over a full free spectral range of the cavities. For the bow-tie squeezing resonator (a), two higher order modes are visible in the center of the FSR. They are presumably emerging from astigmatism inherent in the cavity design. The mode-matching efficiency was estimated to be around 96%. For the SEMC (b), a good mode-matching is crucial due to a direct translation from mode-matching to loss on the squeezed field. The SEMC mode-matching was estimated to be around 98%.

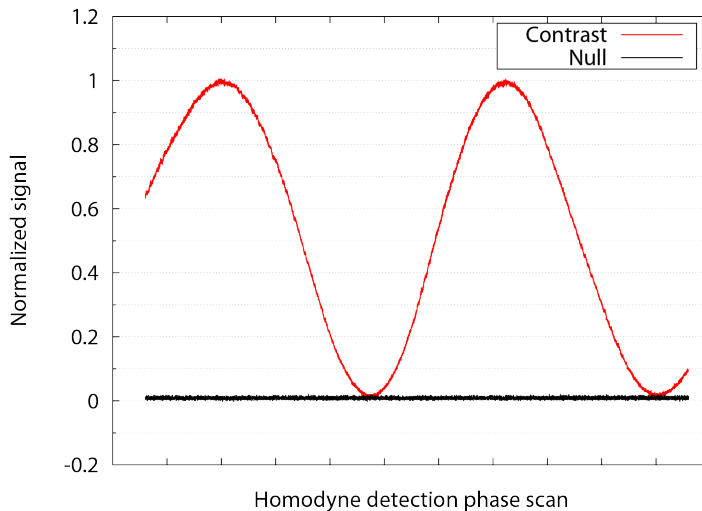


Figure 7.6.: Homodyne detection visibility measured with a photodetector. The local oscillator field and a control field with equal powers were overlapped on the homodyne detection beam splitter. A piezo-actuated mirror phase shifted the local oscillator and gave rise to the interference contrast signal (red). A null measurement was performed as reference for perfect homodyne visibility (black). We measured the contrast to be around 98.9%.

of the two beams. The visibility was estimated to be 98.9% by measuring the interference contrast with a photodetector (see Fig. 7.6). The homodyne detector was the same custom designed, high bandwidth detector as described in chapter 5.6.1. The detector's photodiodes had a quantum efficiency of 94% in the Kerr squeezing setup.

7.4. Measurement results

It was important to verify the presence of the Kerr effect in the bow-tie resonator to ensure that the generated squeezing was due to the cascaded Kerr effect. For this we measured the deformation of the cavity's resonance peaks by lengthening (Fig. 7.7a) and shortening (Fig. 7.7b) the cavity, respectively.

In this experiment, we tuned the temperature to quasi-phase-mismatch condition for the SHG process, since the cascaded Kerr effect is maximal at this point (see chapter 2.5.2). However, it is not vanishing at ideal quasi-phase-matching for a periodically-poled nonlinear medium [79, 80].

We injected three different fundamental pump field powers into the Kerr squeezing resonator, while detuning the cavity length. Without a Kerr effect present at low pump powers, the resonance peak had the typical symmetrical Airy-peak shape. An increase of pump power

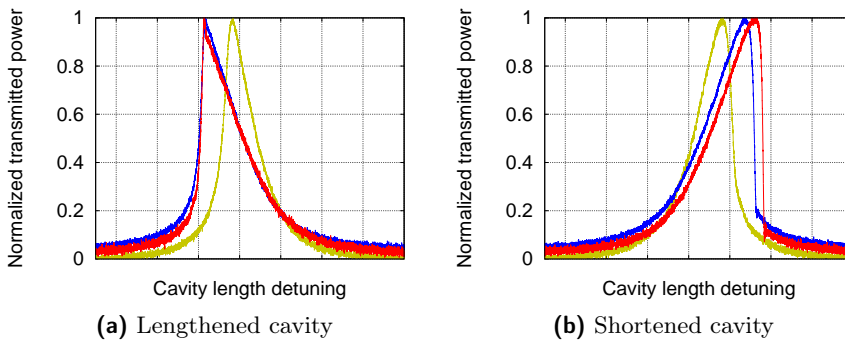


Figure 7.7.: Kerr effect induced resonance peak deformation for the bow-tie resonator for a lengthened cavity (left) and a shortened cavity (right). Three different input powers were used with 73 mW (yellow), 147 mW (blue) and 218 mW (red). The resonance peak shows the typical power dependent deformation for a Kerr nonlinear resonator. The PPKTP absorption of $\alpha_{1550} = 84 \pm 40$ ppm/cm at 1550 nm could be ruled out as the source of the deformation.

7. Squeezed light generated via the cascaded Kerr effect

lead to a deformation of the Airy-peak shape, depending on the pump power as well as the scanning direction. The deformation is caused by the nonlinear phase shift of the circulating laser light via the cascaded Kerr effect. Their typical shapes are described in more detail in [76, 77]. The Kerr-like shaped resonance peaks show meta-stable states, the so called critical points. Stabilizing the cavity as close as possible to these critical points will lead to Kerr squeezed light with maximal squeezing (see [81]).

Figures 7.7a and 7.7b clearly show power dependent resonance peak deformations due to the Kerr effect. High scanning frequencies for the cavity length were applied to the piezo-actuator to ensure that thermal effects due to absorption in the PPKTP crystal can be neglected. Indeed, there were no signs of absorption effects, which can be confirmed by the independent measurement in [56] yielding an absorption for PPKTP as low as $\alpha_{1550} = 84 \pm 40$ ppm/cm at 1550 nm.

7.4.1. Kerr squeezing measurements at subsequent free spectral ranges

We performed Kerr squeezing measurements at the first (358.3 MHz) and the third (1074.9 MHz) free spectral range of the bow-tie cavity. The squeezing resonator was pumped with 85 mW of 1550 nm light and was stabilized on resonance. The squeezed vacuum sidebands as well as the bright pump field carrier were propagated to the SEMC, which was manually stabilized in the center of the two fundamental s-polarized modes. While the bright carrier was reflected off the SEMC and dumped, the squeezed sidebands were transmitted through the cavity and mode-matched to the homodyne detection beam splitter. A homodyne detector with high bandwidth detected the squeezed light with 4 mW of local oscillator power. The dark-noise clearance with 4 mW of local oscillator power was about 9.5 dB at 358.3 MHz and about 8.4 dB at 1074.9 MHz.

The measured squeezing spectra show the Kerr squeezing and Kerr anti-squeezing at 358.3 MHz (see Fig. 7.8) and 1074.9 MHz (see Fig. 7.9) sideband frequency, respectively. The measurements are dark-noise corrected and normalized to the vacuum level. They yield a squeezing value of around 2 dB and an anti-squeezing value of 9.5 dB at 358.3 MHz as well as a squeezing value of around 2.2 dB and an anti-squeezing value of 8.2 dB at 1074.9 MHz. Due to the good dark-noise clearance, the non-corrected squeezing values were only about 0.1-0.2 dB lower.

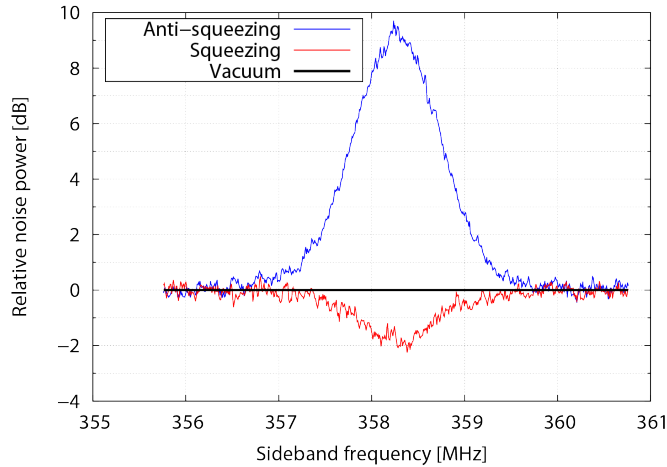


Figure 7.8.: Normalized Kerr squeezing spectrum at 358.3 MHz sideband frequency with a resolution bandwidth of 500 kHz, a video bandwidth of 200 Hz and a sweep time of 250 ms. The fundamental pump power was 85 mW at 1550 nm with a local oscillator power of 4 mW. The measurements are dark-noise corrected. A nonclassical noise suppression of 2 dB is detected with a squeezing bandwidth of about 600 kHz as a result of the bow-tie cavity's linewidth.

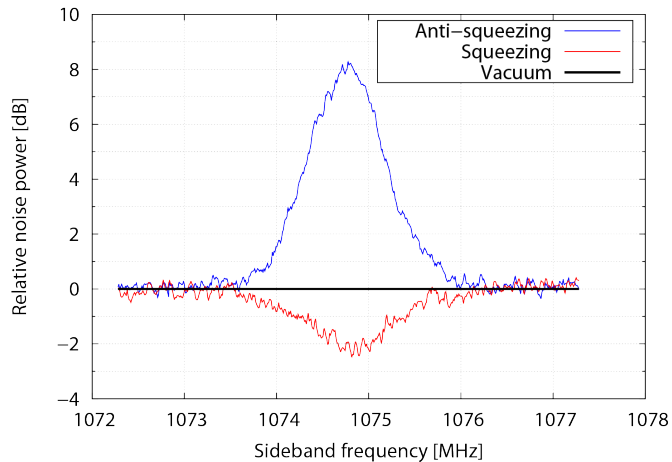


Figure 7.9.: Normalized Kerr squeezing spectrum at 1074.9 MHz sideband frequency with a resolution bandwidth of 500 kHz, a video bandwidth of 200 Hz and a sweep time of 125 ms. The fundamental pump power was 85 mW at 1550 nm with a local oscillator power of 4 mW. The measurements are dark-noise corrected. We detected a nonclassical noise suppression of about 2.2 dB with a squeezing bandwidth of about 600 kHz as a result of the bow-tie cavity's linewidth.

7. Squeezed light generated via the cascaded Kerr effect

We achieved a real nonclassical noise suppression, rather than a classical noise suppression as in previous experiments. The squeezed quadrature measurement clearly drops below the vacuum level and no technical noise is spoiling the vacuum level in the experiment. Although an off-resonant detuning close to the critical point would have yielded a higher squeezing value, we did not achieve this due to the intrinsic instability of the resonator design.

7.5. Simulated & estimated loss

In this section, I simulated the loss in the Kerr squeezing experiment by using the squeezing (2.0 dB) and anti-squeezing (9.6 dB) values for 358.3 MHz at 85 mW pump power. The initial squeezing value for 85 mW pump was fitted to be 13.4 dB. I related the decrease in squeezing as well as in anti-squeezing to increasing losses. The simulation stated that losses of 61 % are in accordance with the measured squeezing values (see Fig. 7.10). This loss value possibly included the effect of phase noise induced by the SEMC and the bow-tie resonator, which could not be separated from the effect of optical loss in the experiment.

After simulating the total optical losses, I estimated the individual loss sources in the experimental setup. The estimation exhibits large errors due to pump power dependent phase noise and conversion loss. I considered the following loss contributions:

Optical path loss

The homodyne detection visibility was measured to be 98.9 %, the photodiode detection efficiency was around 94 % and the losses due to optical elements, such as mirrors or lenses, can be estimated to contribute around 8-12 %. The overall optical path losses sum up to around 15.4-19.9 % (**0.801-0.846** detection efficiency) from those sources.

Bow-tie intra-cavity loss

The internal loss of the bow-tie Kerr squeezing resonator was estimated to be around 45.3 % (**0.547** detection efficiency). We compared the pump field power entering the bow-tie coupling mirror with the back reflected light on cavity resonance to estimate this value. It is

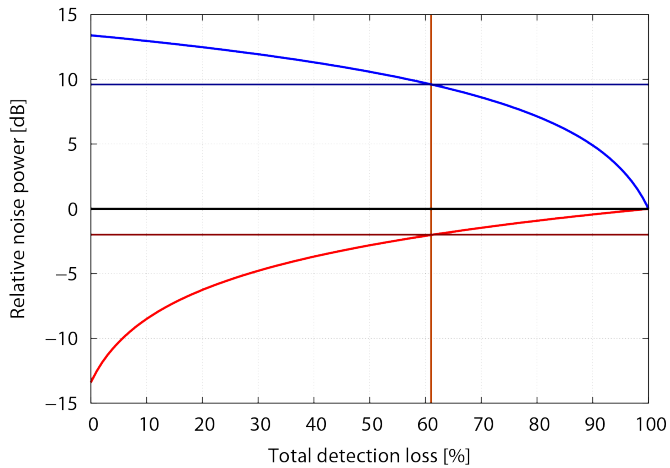


Figure 7.10.: Total detection loss simulated for the Kerr squeezing resonator with a pump power of 85 mW. The simulated loss for 2.0 dB squeezing (dark-red) and 9.6 dB anti-squeezing (dark-blue) is about 61 %. The simulation is based on the measurement at 358.3 MHz and does not distinguish between optical loss and phase noise.

by far the highest contribution and consists mostly of frequency doubling of the fundamental pump field at 1550 nm to 775 nm light. The second harmonic field was measured and simulated to be at least 10 % of the circulating light power at 85 mW pump power. The losses from conversion were strongly dependent on the fundamental pump power. Additional but almost negligible loss sources in the bow-tie cavity were stray light losses and optical absorption in the PPKTP crystal. The impedance matching of the cavity also acted as a loss channel for the squeezed field. Some fraction of the squeezing was therefore transmitted through the other cavity mirrors where the nonclassical field was not detected.

Sideband extraction modecleaner loss

The optical losses at the SEMC can be divided up into two main contributions.

The first is the transmission loss through the SEMC due to impedance mismatch and mode mismatching to the cavity. The impedance mismatch was estimated to be around 8.65 % by measuring the resonance peak in reflection of the cavity.

The second loss contribution was the mismatch of the free spectral ranges for the SEMC (716.331 MHz) and the bow-tie cavity

7. Squeezed light generated via the cascaded Kerr effect

($2 \cdot 358.265 \text{ MHz} = 716.53 \text{ MHz}$). The corresponding FSR deviation for both cavities was around 200 kHz. This mismatch led to an additional loss channel for the transmitted squeezing sidebands. It was taken into account using the SEMC linewidth of 1.15 MHz and the FSR deviation of 200 kHz. The effect was difficult to determine due to the imprecise measurement of the FSRs of both cavities. We estimated the effect to cause another 2.9 % of loss.

With the impedance mismatch and the FSR inequality included, the overall transmission loss of the SEMC was measured to be 11.3 % (**0.887** detection efficiency).

Phase noise

The higher squeezing, but lower anti-squeezing values at 1074.9 MHz in comparison to 358.3 MHz suggest that phase noise is affecting the measurements. The Kerr effect induced deformation of the resonance peak decreased the cavity lock stability. This led to an increased phase noise at higher pump powers. We could, however, not exactly determine the phase noise contribution in the experimental setup.

Total optical loss

The estimated total detection efficiency for the Kerr squeezing measurement was between **0.39** and **0.41**, corresponding to a total loss of around 59-61 % (see table 7.1). Since the estimated loss contributions presumably have large errors, their overall result fits nicely to the simulated loss of 61 % from the squeezing measurement (see Fig. 7.10). Taking into account the large phase noise for the given resonator design, we have to assume an optical loss of below 61 % with a large phase noise contribution. However, the effect of phase noise was degrading the squeezing stronger at higher pump powers.

Type	Detection efficiency
Homodyne detection	0.978
Photodiode quantum efficiency	0.94
Optical path: Mirrors and lenses	0.88-0.92
Kerr bow-tie internal loss	0.547
SEMC optical transmission	0.887
Total efficiency	0.39-0.41

Table 7.1.: Optical loss contributions

7.6. Summary & Outlook

The experiment introduced a first measurement of squeezed light via the cascaded Kerr effect using a bow-tie type resonator. We measured a maximal nonclassical noise reduction of around 2.2 dB at 1074.9 MHz sideband frequency and a wavelength of 1550 nm. The squeezing resonator consisted of a quasi phase matched PPKTP crystal with temperature stabilization in a bow-tie cavity configuration using a fundamental pump field power of 85 mW. A high bandwidth homodyne detector performed the measurement with an estimated quantum efficiency of 94 % and a local oscillator power of 4 mW. The squeezing strength was limited by an overall optical loss of around 61 %, including a large, but unknown, phase noise contribution.

In future experiments, a quasi-monolithic bow-tie resonator design should be a feasible enhancement of the current setup. This will result in a reduction of the phase noise, which is probably mainly induced by the instability of the current cavity design. The PPKTP crystal's second harmonic generation on phase mismatch must also be decreased to avoid losses. Furthermore, the linewidth of the sideband extraction modecleaner should be increased, in order to avoid losses on the squeezed field due to impedance mismatch of the SEMC as well as free spectral range detuning.

Even with the high optical losses in the experiment, we measured an anti-squeezing value of up to 9.6 dB. This result paves the way to a squeezed light generation via the cascaded Kerr effect with more than 10 dB of squeezing. More importantly, the generation of non-gaussian states of light in the continuous variable regime seems feasible with the implementation of the cascaded Kerr effect. This will open up a new window in fundamental quantum research using continuous-variable nonclassical states of light.

8

Chapter 8.

Conclusion

Since the first experimental demonstration of squeezed states of light almost 30 years ago, squeezing sources have developed to a level where they can fulfill applications in a broad variety of physics experiments. In gravitational wave detectors they recently evolved to be important pillars for further enhancing the sensitivities. State of the art squeezing resonators already reached the design parameters to be used in third generation GW detectors and even promise to achieve measurements beyond the standard quantum limit.

In quantum key distribution, however, the journey for squeezed light has just begun. Future applications and fundamental research will need new approaches in nonclassical light generation and will potentially benefit greatly from an enhanced squeezing bandwidth [82, 83].

In this thesis, I presented the experimental realization of a second harmonic generation cavity with the highest ever observed conversion efficiency of $(95 \pm 0.81)\%$ from 1550 nm to 775 nm. The frequency doubled light was generated to act as a pump field for our nonclassical light sources. The SHG is able to be used as an effective tool for the frequency conversion of nonclassical quantum states.

The thesis presented the generation and detection of a broadband squeezed field at 1550 nm without using a fundamental cavity. This yielded a white squeezing spectrum with 0.3 dB nonclassical noise suppression with a bandwidth of 2 GHz. The measurement results were limited by a large optical loss of about 80 % and by insufficient pump power. However, to the best of my knowledge, I experimentally detected the largest continuous-wave squeezing bandwidth so far.

Furthermore, I have demonstrated the generation of squeezed light

8. Conclusion

with 3.5 dB nonclassical noise suppression over a bandwidth of more than 1 GHz sideband frequency at the telecommunication wavelength of 1550 nm. The optical loss of 25 % was the limiting factor for the measured squeezing, which was simulated to exceed 10 dB (5.5 dB at 1 GHz) with a reduced loss contribution of only 4 %.

I performed a proof of principle experiment using two of the aforementioned squeezing resonators to generate two-mode entanglement with GHz bandwidth. The Duan value was calculated to be at least 0.75 over a bandwidth of 1.2 GHz having a minimum of 0.6 at 200 MHz with 1 being the Duan-threshold. In principle, a further developed version of the GHz bandwidth squeezing resonator is able to achieve about a 20-fold increase in measurement speed for QKD experiments compared to the squeezed light source used in [84, 34].

This thesis also reports on the first experimental realization of squeezed light via the cascaded Kerr effect. We achieved a nonclassical noise suppression of about 2.0 dB at 358.3 MHz and 2.2 dB at 1074.9 MHz below the vacuum noise level, respectively. The experimental measurements were limited by optical loss and phase noise, which resulted in a value of 0.61 for the total detection efficiency. Our demonstration of squeezed light via the cascaded Kerr effect might mark the starting point for the generation of non-gaussian quantum states in the continuous-variable regime.

The various new approaches in squeezed light generation presented in this thesis offer distinct advantages compared to conventional squeezed light sources. They have the potential to be further developed for QKD applications and offer new possibilities for research on fundamental quantum effects.



Appendix A.

Appendix

A.1. Open-loop gain for the high conversion efficiency SHG

We designed a custom servo controller for the electronic feedback loop of SHG cavity's length stabilization. The open-loop gain transfer function was measured in Fig. A.1 and yielded a unity-gain frequency of about 4 kHz.

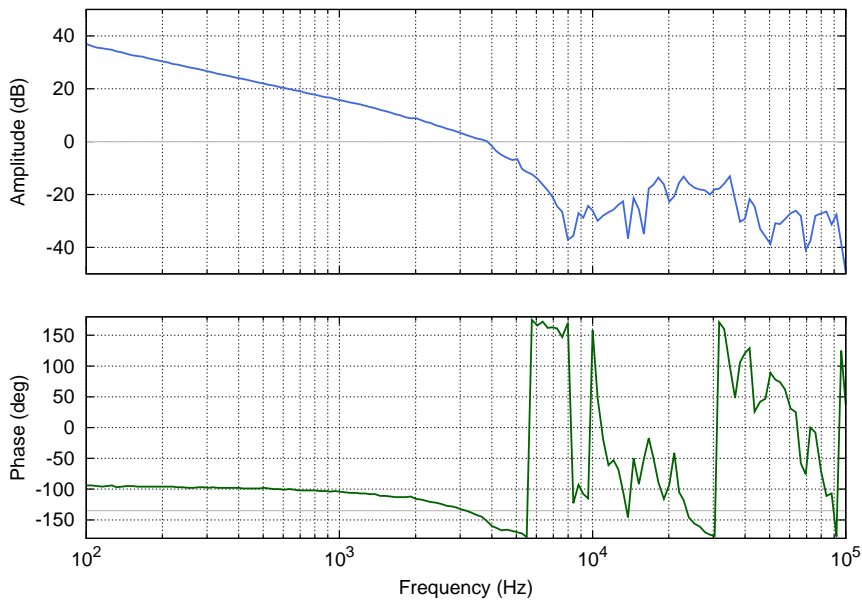


Figure A.1.: SHG open loop gain with a unity gain frequency of around 4 kHz.

A. Appendix

A.2. Monolithic squeezing resonator N.L.C.S. simulations

The N.L.C.S. script for simulating the monolithic squeezing resonator with a 2.6 mm long PPKTP crystal is depicted below.

```
# N.L.C.S. simulation file used for the monolithic GHz squeezer
# with 2.6 mm long PPKTP crystal
# File varies the fundamental mirror reflectivity
# of the input coupling mirror
# List value order is: fundamental, harmonic, idler.
# Output port indices: 1 - Reflection, 2 - Transmission.

# Parameter settings
p1 = 0.0, 0.9, 100 # variation of the fundamental reflectivity
p2 = 5e6, 1.5e9, 100 # variation of the sideband frequency
plot_col = 14
optimize = min

+++ NLCS configuration file +++
Laser {
w0 = 33.86e-6 # fundamental waist radius [m]
lambda = {1550e-9, 775e-9} # wavelength [m]
Port 1 {
P = {0.0, 0.1} # input power [W]
}
}

Cavity {
FSR = 31.75e9 # free spectral range [Hz]

Mirror 1 {
R = {p1, 0.98} # power reflectivity
}

Mirror 2 {
R = {0.9998, 0.9998} # power reflectivity
}

Crystal 1 {
chi = 6.5e-12 # crystal nonlinearity [m/V]
```

A.2. Monolithic squeezing resonator N.L.C.S. simulations

```
L = 0.0026 # length [m]
n = 1.816 # index of refraction for the fundamental wavelength
alpha = {0.0084, 0.0125} # linear power absorption [1/m]
}
}
```

```
Homo 1 {
theta = {0.0, 0.0} # homodyne angle [pi]
eta = {0.9} # quantum efficiency
optimize = true # detects squeezed quadrature
}
```

```
Plot {
scan = "frequency" # scanparameter
step = 100 # resolution of the x axis
eps = 1e-6 # steady state precision
y = "squeezing" # parameter for the y axis
range = {p2, p2} # plot range
}
```

The N.L.C.S. script for the simulation of the optical parametric oscillator threshold is depicted below. Note, the higher effective nonlinearity chosen for the PPKTP crystal. This was a result from the squeezing measurement, where the simulation scripts were using the higher value for fitting the experimental results properly. The fitted nonlinearity of 7.3 pm/V is the definitive value for our PPKTP crystal.

The simulation yielded a threshold of 655 mW external pump power.

```
# N.L.C.S. simulation for the parametric oscillation threshold
# the variation parameter is the harmonic pump power
# Threshold Power: P_th = 655 mW
# List value order is: fundamental, harmonic, idler.
# Output port indices: 1 - Reflection, 2 - Transmission.
```

```
Laser {
w0 = 33.86e-6 # fundamental waist radius [m]
lambda = {1550e-9, 775e-9} # wavelength [m]
Port 1 {
P = {0.0, 0.0} # input power [W]
}
}
```

A. Appendix

```
Cavity {
FSR = 31.75e9 # free spectral range [Hz]

Mirror 1 {
R = {0.64, 0.98} # power reflectivity
}

Mirror 2 {
R = {0.9998, 0.9998} # power reflectivity
}

Crystal 1 {
chi = 7.3e-12 # nonlinearity [m/V]
L = 0.0026 # length [m]
n = 1.816 # index of refraction
alpha = {0.0084, 0.0125} # linear power absorption [1/m]
}
}

Homo 1 {
theta = {0.0, 0.0} # homodyne angle [pi]
eta = {0.9} # quantum efficiency
optimize = true
}

Plot {
scan = "harmonic power" # scanparameter
step = 100 # resolution of the x axis
eps = 1e-6 # steady state precision
y = "squeezing" # parameter for the y axis
range = {0, 1.0} # plot range
}
```

A.2.1. Pictures from the experimental setup

Some pictures were taken in the laboratory to show the experimental design around the squeezing resonator, especially the pump path (see Fig. A.2), the control path to the homodyne detector (see Fig. A.3) and the inputs/outputs of the squeezer (see Fig. A.4).

A.2. Monolithic squeezing resonator N.L.C.S. simulations

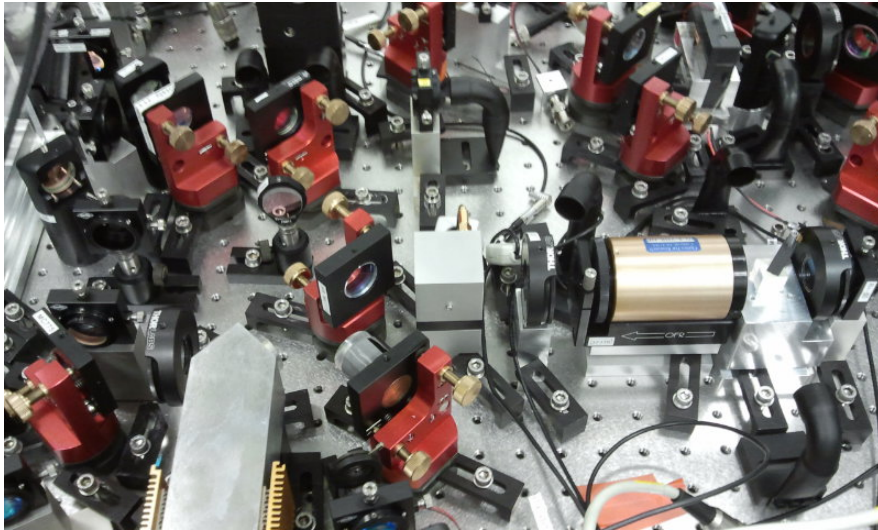


Figure A.2.: Photograph of the pump path to the monolithic squeezing resonator.

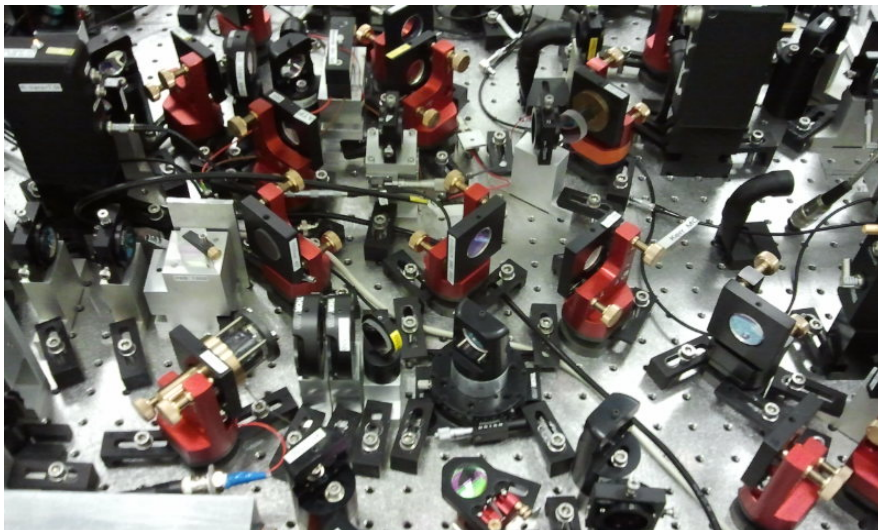


Figure A.3.: Photograph of the monolithic squeezing resonator and the path for the squeezed field to the homodyne detector (not visible in the picture).

A. Appendix

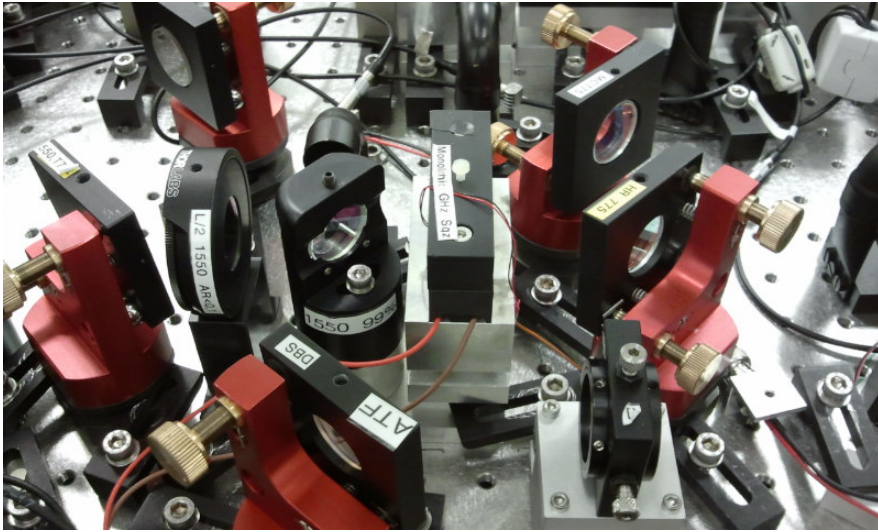


Figure A.4.: Photograph of the monolithic squeezing oven with the control field entering from the left side and the pump field entering from the right side.

A.3. Pump phase stabilization open-loop gain

A.3. Pump phase stabilization open-loop gain

A custom designed servo controller was used for the pump phase stabilization of the monolithic squeezing resonator. The open-loop transfer function of the electronic feedback loop is depicted in Fig. A.5 and yields a unity-gain frequency of 1.8 kHz. The pump phase and homodyne readout stabilization coupled with the high efficiency photodiodes were responsible for the increased squeezed light measurement performance of chapter 5.8.3 with respect to the measurements in chapter 5.6.2.

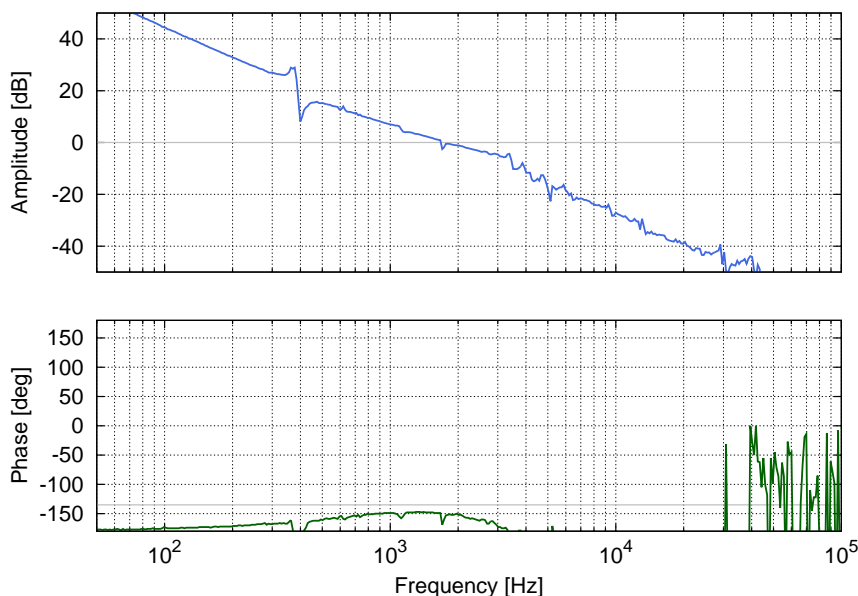


Figure A.5.: Open-loop gain of the pump phase lock for the monolithic squeezing resonator with a unity-gain frequency of about 1.8 kHz.

A.4. GHz bandwidth homodyne detector circuit

I used two identically built homodyne detectors with GHz bandwidth designed by M. Mehmet (see Fig. A.6). They were used for the detection of the two-mode entangled beams and their AC outputs were subtracted to get access to the required variances.

A.5. GHz entanglement homodyne detector spectra

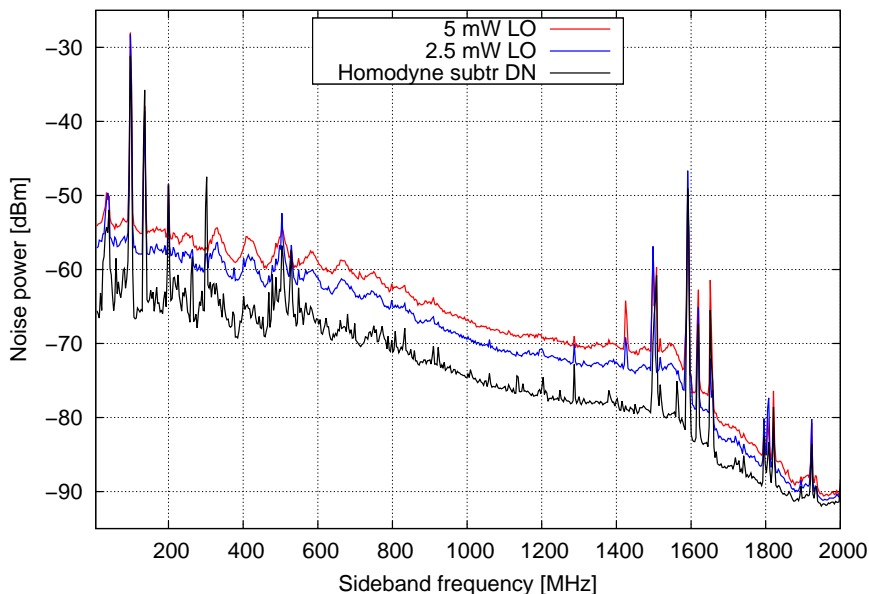


Figure A.7.: Subtracted signal of the two GHz homodyne detectors using a conventional power splitter by *Mini Circuits* type *ZFSCJ-2-4+*. Doubling the power results in a 3 dB increase in noise power as expected from a linearly behaving homodyne detector measuring vacuum noise.

A.5. GHz entanglement homodyne detector spectra

A measurement spectrum for the subtracted signals of the two homodyne detectors is depicted in Fig. A.7 for 2.5 mW and 5 mW of local oscillator power. The noise level is rising 3 dB with doubling the power, as expected for a vacuum noise limited measurement spectrum. This is a proof for the linear behavior of the subtracted homodyne detection signals.

The two individual noise spectra from the GHz bandwidth homodyne detectors are depicted in Fig. A.8 for homodyne detector 1 and in Fig. A.9 for homodyne detector 2. The spectra show a similar behavior with homodyne detector 2 having slightly more noise below 500 MHz, while homodyne detector 1 exhibits a ripple at around 1400 MHz. Several electronic pick-up peaks arise in the spectra below 500 MHz and above 1000 MHz. The lower frequency peaks are due to Pound-Drever-Hall locking frequencies at 20.9 MHz, 101 MHz and 138 MHz as well as their harmonics. The higher frequency peaks

A. Appendix

above 1400 MHz are probably GPS tracking signals as well as mobile phone frequencies. More importantly all the peaks also show up in the dark noise spectra of both homodyne detectors and are thus electronic pick-up.

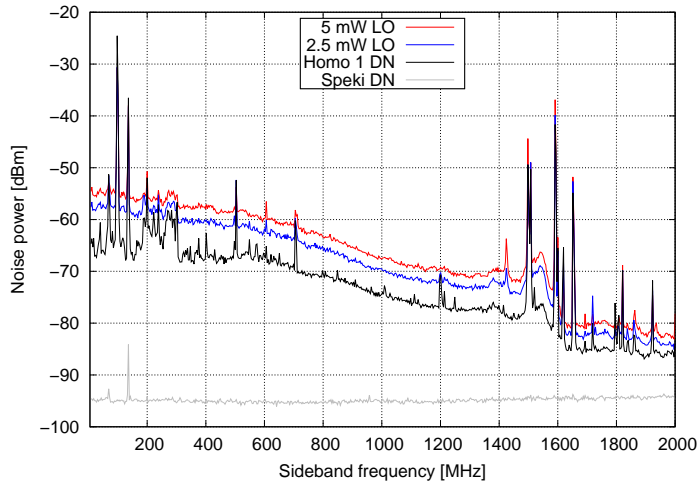


Figure A.8.: Characterization of the first GHz bandwidth homodyne detector using custom made photodiodes with a quantum efficiency of 99%.

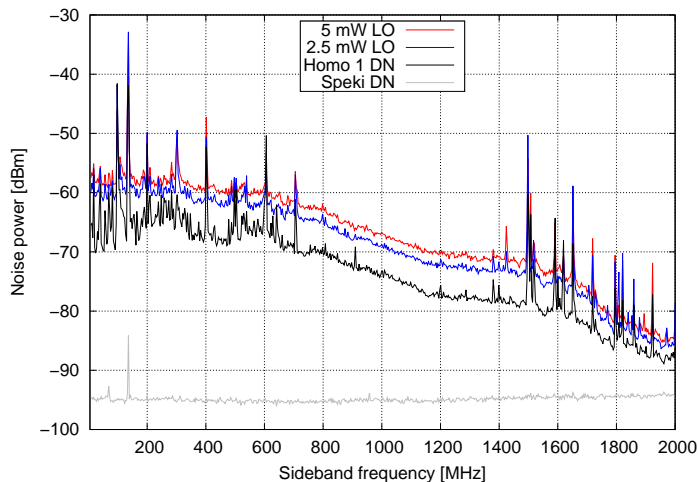


Figure A.9.: Characterization of the second GHz bandwidth homodyne detector using custom made photodiodes with a quantum efficiency of 99%

A.6. Kerr squeezing bow-tie experimental pictures

A.6. Kerr squeezing bow-tie experimental pictures

Photographs of the quasi-monolithic bow-tie resonator designed to generate Kerr squeezing are depicted in Figs. A.10, A.11, A.12, A.13 on the next pages. They show the aluminum baseplate, the mirror mounts from *New Focus* and the oven construction for the 10 mm long PPKTP crystal. The cavity's geometrical round-trip length was 832 mm.

A. Appendix

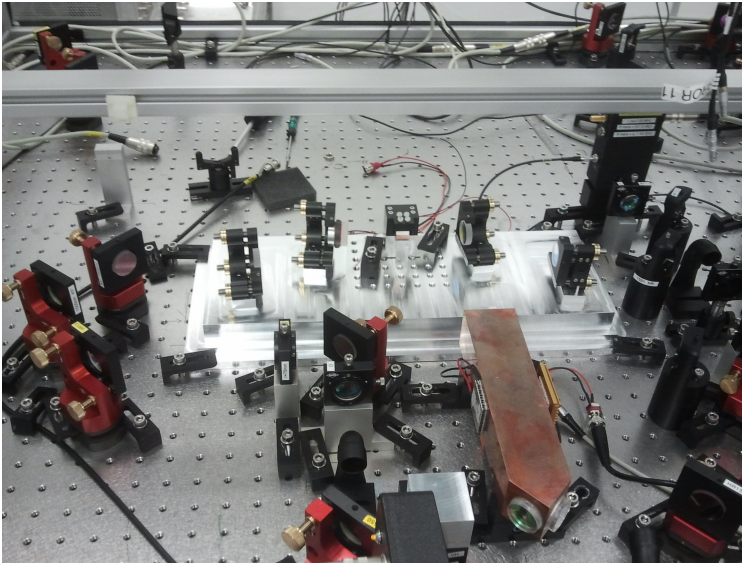


Figure A.10.: Front view of the Kerr squeezing bow-tie resonator in the experimental setup.

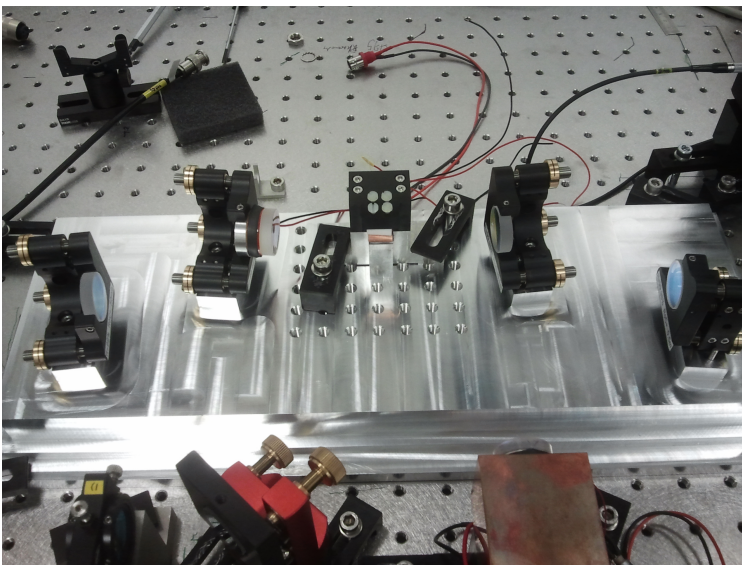


Figure A.11.: Front view of the Kerr squeezing bow-tie resonator.

A.6. Kerr squeezing bow-tie experimental pictures

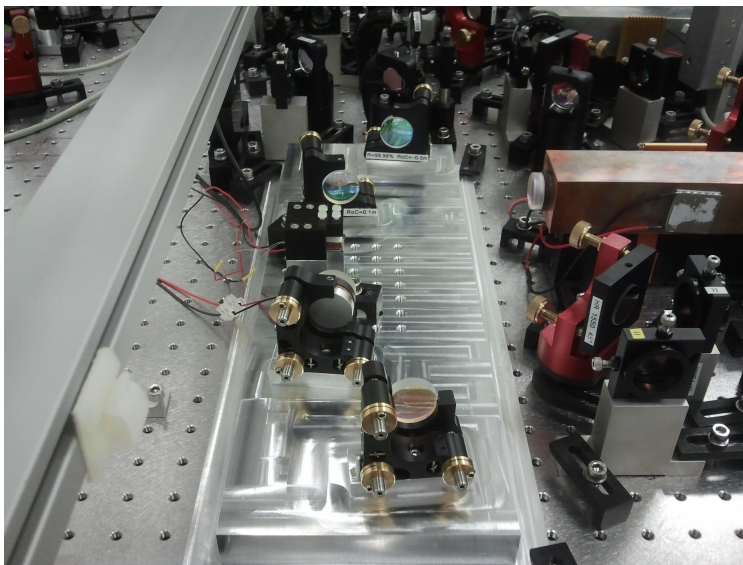


Figure A.12.: Side view of the Kerr squeezing bow-tie resonator.

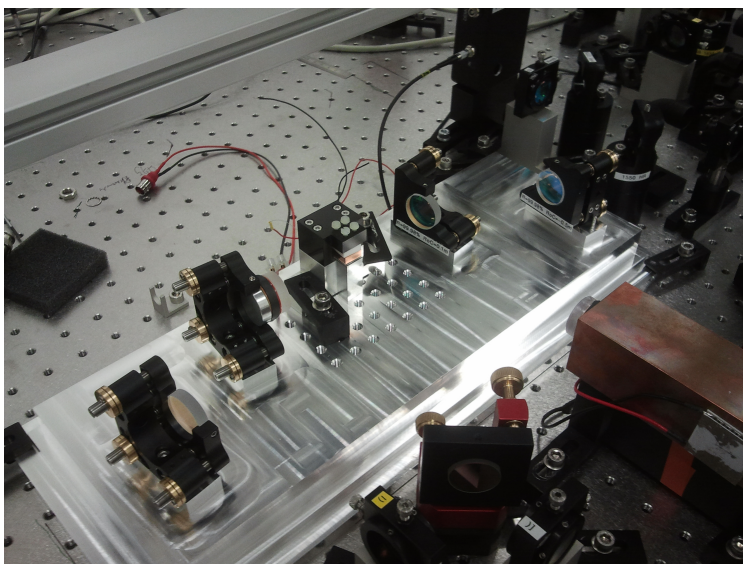


Figure A.13.: Isometric view of the Kerr squeezing bow-tie resonator.

A.7. Kerr squeezing bow-tie CAD drawings

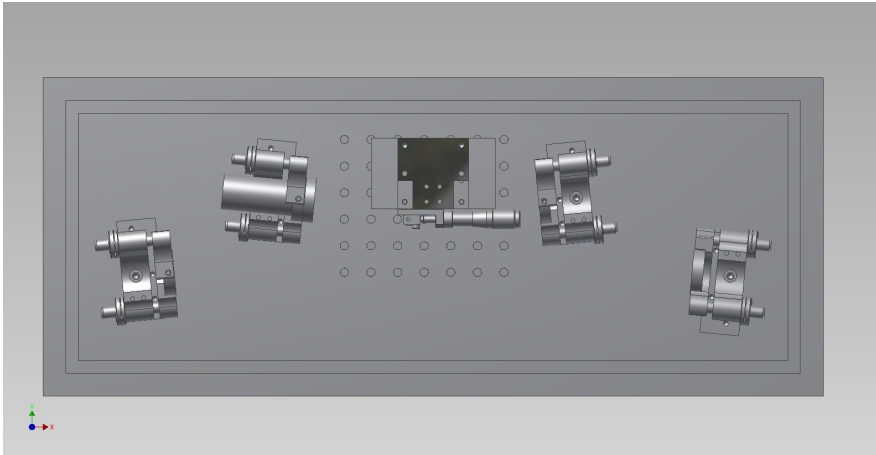


Figure A.14.: Top view of the schematic CAD drawing of the complete bow-tie resonator designed with Autodesk Inventor.

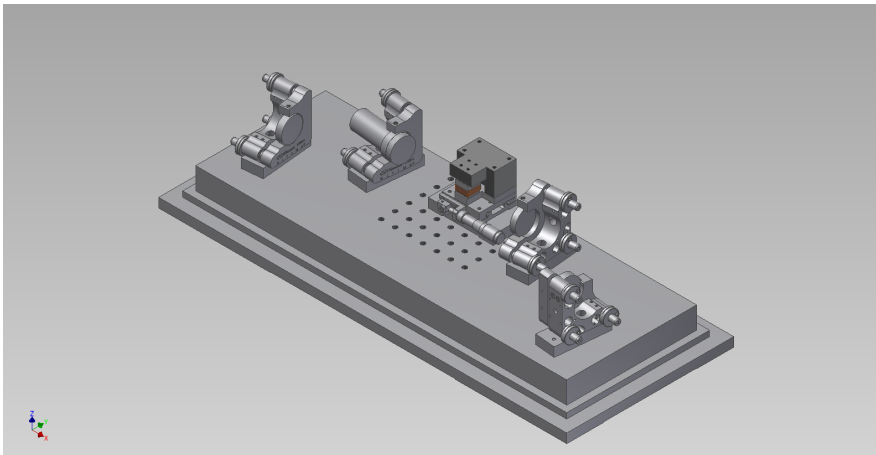


Figure A.15.: View of the isometric perspective of the schematic CAD drawing of the complete bow-tie resonator designed with Autodesk Inventor.

The CAD drawings for the bow-tie resonator were designed by A. Pal Singh and show a schematic view of the construction holding the cavity mirrors and the PPKTP crystal with its housing including the temperature stabilization elements (see Figs. A.14 & A.15).

Bibliography

- [1] A. Buonanno and Y. Chen, *Optical noise correlations and beating the standard quantum limit in advanced gravitational-wave detectors*, *Classical and Quantum Gravity* **18**, L95 (2001). 21
- [2] S. L. Danilishin and F. Y. Khalili, *Quantum Measurement Theory in Gravitational-Wave Detectors*, *Living Reviews in Relativity* **15**, (2012). 21
- [3] C. M. Caves, *Quantum-mechanical noise in an interferometer*, *Physical Review D* **23**, 1693 (1981). 21
- [4] W. P. Bowen, R. Schnabel, P. K. Lam and T. C. Ralph, *Experimental Investigation of Criteria for Continuous Variable Entanglement*, *Physical Review Letters* **90**, 43601 (2003). 21
- [5] H. Yuen and J. Shapiro, *Optical communication with two-photon coherent states—Part I: Quantum-state propagation and quantum-noise*, *Information Theory, IEEE Transactions on* **24**, 657 (1978). 21
- [6] A. K. Ekert, *Quantum Cryptography Based on Bell's Theorem*, *Physical Review Letters* **67**, 661 (1991). 21
- [7] C. Rodò, O. Romero-Isart, K. Eckert and A. Sanpera, *Efficiency in Quantum Key Distribution Protocols with Entangled Gaussian States*, *Open Systems & Information Dynamics* **14**, 69 (2007). 21
- [8] J. DiGuglielmo, B. Hage, A. Franzen, J. Fiurášek and R. Schnabel, *Experimental characterization of Gaussian quantum-communication channels*, *Physical Review A* **76**, 12323 (2007). 21
- [9] H. P. Yuen, *Two-photon coherent states of the radiation field*, *Physical Review A* **13**, 2226 (1976). 21
- [10] R. E. Slusher, L. W. Hollberg, B. Yurke, J. C. Mertz and J. F. Valley, *Observation of Squeezed States Generated by Four-Wave*

BIBLIOGRAPHY

- Mixing in an Optical Cavity*, Physical Review Letters **55**, 2409 (1985). 21
- [11] H. Vahlbruch, M. Mehmet, S. Chelkowski, B. Hage, A. Franzen, N. Lastzka, S. Goßler, K. Danzmann and R. Schnabel, *Observation of Squeezed Light with 10-dB Quantum-Noise Reduction*, Physical Review Letters **100**, 33602 (2008). 21, 22
- [12] T. Eberle, S. Steinlechner, J. Bauchrowitz, V. Händchen, H. Vahlbruch, M. Mehmet, H. Müller-Ebhardt and R. Schnabel, *Quantum Enhancement of the Zero-Area Sagnac Interferometer Topology for Gravitational Wave Detection*, Physical Review Letters **104**, 251102 (2010). 21, 22
- [13] S. Spälter, M. Burk, U. Ströckner, A. Sizmann and G. Leuchs, *Propagation of quantum properties of sub-picosecond solitons in a fiber*, Optics Express **2**, 659 (1998). 21
- [14] R. E. Slusher, P. Grangier, A. LaPorta, B. Yurke and M. J. Potasek, *Pulsed Squeezed Light*, Physical Review Letters **59**, 2566 (1987). 21
- [15] R. Dong, J. Heersink, J. F. Corney, P. D. Drummond, U. L. Andersen and G. Leuchs, *Experimental evidence for Raman-induced limits to efficient squeezing in optical fibers*, Optics Letters **33**, 116 (2008). 21
- [16] L.-A. Wu, H. J. Kimble, J. L. Hall and H. Wu, *Generation of Squeezed States by Parametric Down Conversion*, Physical Review Letters **57**, 2520 (1986). 22
- [17] L.-A. Wu, M. Xiao and H. J. Kimble, *Squeezed states of light from optical parametric oscillator*, Journal of the Optical Society of America **B4**, 1465 ff. (1987). 22
- [18] C. Silberhorn, P. K. Lam, O. Weiß, F. König and N. Korolkova, *Generation of Continuous Variable Einstein-Podolsky-Rosen Entanglement via the Kerr Nonlinearity in an Optical Fiber*, Physical Review Letters **86**, 4267 (2001). 22
- [19] D. W. C. Brooks, T. Botter, S. Schreppler, T. P. Purdy, N. Brahms and D. M. Stamper-Kurn, *Non-classical light generated by quantum-noise-driven cavity optomechanics*, Nature **488**, 476 (2012). 22

- [20] B. Yurke, *Use of cavities in squeezed-state generation*, Physical Review A **29**, 408 (1984). 22
- [21] M. Mehmet, S. Ast, T. Eberle, S. Steinlechner, H. Vahlbruch and R. Schnabel, *Squeezed light at 1550 nm with a quantum noise reduction of 12.3 dB*, Optics express **19**, 25763 (2011). 22, 72, 79, 89, 90
- [22] H. Vahlbruch, A. Khalaidovski, N. Lastzka, C. Gräf, K. Danzmann and R. Schnabel, *The GEO 600 squeezed light source*, Classical and Quantum Gravity **27**, 084027 (2010). 22
- [23] B. Sathyaprakash and B. F. Schutz, *Physics, astrophysics and cosmology with gravitational waves*, Living Reviews in Relativity **12**, (2009). 22
- [24] G. M. Harry and others for the LIGO Scientific Collaboration, *Advanced LIGO: the next generation of gravitational wave detectors*, Classical and Quantum Gravity **27**, 84006 (2010). 22
- [25] T. Accadia, F. Acernese, F. Antonucci, P. Astone, G. Ballardin, F. Barone, M. Barsuglia, A. Basti, T. S. Bauer, M. Bebronne *et al.*, *Status of the Virgo project*, Classical and Quantum Gravity **28**, 114002 (2011). 22
- [26] H. Grote and others for the LIGO Scientific Collaboration, *The GEO 600 status*, Classical and Quantum Gravity **27**, 084003 (2010). 22
- [27] KAGRA Collaboration, *Interferometer design of the KAGRA gravitational wave detector*, Physical Review D **88**, 043007 (2013). 22
- [28] LIGO Scientific Collaboration, *A gravitational wave observatory operating beyond the quantum shot-noise limit*, Nature Physics **7**, 962 (2011). 23
- [29] LIGO Scientific Collaboration, *Enhanced sensitivity of the LIGO gravitational wave detector by using squeezed states of light*, Nature Photonics **7**, 613 (2013). 23
- [30] H. Grote, K. Danzmann, K. Dooley, R. Schnabel, J. Slutsky and H. Vahlbruch, *First long-term application of squeezed states of light in a gravitational-wave observatory*, Physical review letters **110**, 181101 (2013). 23

BIBLIOGRAPHY

- [31] M. Punturo, M. Abernathy, F. Acernese, B. Allen, N. Andersson, K. Arun, F. Barone, B. Barr, M. Barsuglia, M. Beker *et al.*, *The Einstein Telescope: a third-generation gravitational wave observatory*, *Classical and Quantum Gravity* **27**, 194002 (2010). 23
- [32] D. Dieks, *Communication by EPR devices*, *Physics Letters A* **92**, 271 (1982). 23
- [33] W. K. Wootters and W. H. Zurek, *A single quantum cannot be cloned*, *Nature* **299**, 802 (1982). 23
- [34] T. Eberle, *Realization of finite-size quantum key distribution based on Einstein-Podolsky-Rosen entangled light*, PhD Thesis, Leibniz Universität Hannover, 2013. 23, 53, 91, 105, 124
- [35] G. S. Vernam, *Cipher printing telegraph systems: For secret wire and radio telegraphic communications*, *Journal of the AIEE* **45**, 109 (1926). 23
- [36] M. Mehmet, H. Vahlbruch, N. Lastzka, K. Danzmann and R. Schnabel, *Observation of squeezed states with strong photon-number oscillations*, *Physical Review A* **81**, 13814 (2010). 24
- [37] J. Lodewyck, M. Bloch, R. García-Patrón, S. Fossier, E. Karpov, E. Diamanti, T. Debuisschert, N. J. Cerf, R. Tualle-Brouri, S. W. McLaughlin and P. Grangier, *Quantum key distribution over 25 km with an all-fiber continuous-variable system*, *Physical Review A* **76**, 42305 (2007). 24, 53
- [38] M. Mehmet, T. Eberle, S. Steinlechner, H. Vahlbruch and R. Schnabel, *Demonstration of a quantum-enhanced fiber Sagnac interferometer*, *Optics Letters* **35**, 1665 (2010). 24, 53
- [39] R. García-Patrón and N. J. Cerf, *Continuous-Variable Quantum Key Distribution Protocols Over Noisy Channels*, *Physical Review Letters* **102**, 130501 (2009). 24
- [40] S. L. Braunstein and P. van Loock, *Quantum information with continuous variables*, *Review of Modern Physics* **77**, 513 (2005). 27, 31, 91
- [41] A. Einstein, B. Podolsky and N. Rosen, *Can Quantum-Mechanical Description of Physical Reality Be Considered Complete?*, *Physical Review* **47**, 777 ff. (1935). 31

- [42] E. Jakeman, C. Oliver and E. Pike, *Optical homodyne detection*, Advances in Physics **24**, 349 (1975). 31
- [43] H. P. Yuen and J. H. Shapiro, *Generation and detection of two-photon coherent states in degenerate four-wave mixing*, Optics letters **4**, 334 (1979). 31
- [44] L.-M. Duan, G. Giedke, J. I. Cirac and P. Zoller, *Inseparability Criterion for Continuous Variable Systems*, Physical Review Letters **84**, 2722 (2000). 34, 101
- [45] S. Ast, *Erzeugung gequetschter Lichtfelder mit einer Bandbreite über 1 GHz*, Diploma thesis, Leibniz Universität Hannover, 2009. 37, 41
- [46] A. Berzanskis, K. H. Feller and A. Stabinis, *Squeezed light generation by means of cascaded second-order nonlinearity*, Optics Communications **118**, 438 (1995). 37
- [47] R. W. Boyd, *Nonlinear Optics* (Academic Press, 2003). 38, 42
- [48] S. Kawamura, M. Ando, N. Seto, S. Sato, T. Nakamura, K. Tsubono, N. Kanda, T. Tanaka, J. Yokoyama, I. Funaki *et al.*, *The Japanese space gravitational wave antenna: DECIGO*, Classical and Quantum Gravity **28**, 094011 (2011). 41
- [49] T. Meier, B. Willke and K. Danzmann, *Continuous-wave single-frequency 532 nm laser source emitting 130 W into the fundamental transversal mode*, Optics Letters **35**, 3742 (2010). 41
- [50] P. Kumar, *Quantum frequency conversion*, Optics Letters **15**, 1476 (1990). 41
- [51] J. Huang and P. Kumar, *Observation of quantum frequency conversion*, Physical Review Letters **68**, 2153 (1992). 41
- [52] S. Ast, R. Moghadas Nia, A. Schönbeck, N. Lastzka, J. Steinlechner, T. Eberle, M. Mehmet, S. Steinlechner and R. Schnabel, *High-efficiency frequency doubling of continuous-wave laser light*, Optics letters **36**, 3467 (2011). 42, 43, 49, 50, 55
- [53] G. D. Boyd and D. A. Kleinman, *Parametric Interaction of Focused Gaussian Light Beams*, Journal of Applied Physics **39**, 8 ff. (1968). 42

BIBLIOGRAPHY

- [54] R. L. Targat, J.-J. Zondy and P. Lemonde, *75%-Efficiency blue generation from an intracavity PPKTP frequency doubler*, Optics Communications **247**, 471 (2005). 42
- [55] M. Y. Vyatkin, R. I. Yagodkin, A. V. Avdokhin, A. G. Dronov, S. V. Popov, J. R. Taylor and V. P. Gapontsev, *25W average-power, second-harmonic-generation of a linearly-polarized Er fiber source in PPKTP and its application for tandem harmonic generation in UV*, Advanced Solid-State Photonics (TOPS) 155 (2004). 45
- [56] J. Steinlechner, S. Ast, C. Krüger, A. Pal Singh, T. Eberle, V. Händchen and R. Schnabel, *Absorption Measurements of Periodically Poled Potassium Titanyl Phosphate (PPKTP) at 775 nm and 1550 nm.*, Sensors **13**, 565 (2013). 45, 55, 71, 109, 116
- [57] K. R. Parameswaran, J. R. Kurz, R. V. Roussev and M. M. Fejer, *Observation of 99% pump depletion in single-pass second-harmonic generation in a periodically poled lithium niobate waveguide*, Optics Letters **27**, 43 (2002). 47
- [58] N. Lastzka, *Analyse nichtlinearer Resonatoren*, Diploma thesis, Universität Hannover, 2005. 48
- [59] N. Lastzka, *Numerical modelling of classical and quantum effects in non-linear optical systems*, PhD Thesis, Leibniz Universität Hannover, 2010. 48
- [60] C. E. Vollmer, C. Baune, A. Sambrowski, T. Eberle, V. Händchen, J. Fiurášek and R. Schnabel, *Quantum Up-Conversion of Squeezed Vacuum States from 1550 to 532 nm*, Physical Review Letters **112**, 073602 (2014). 52
- [61] C. Baune, A. Schönbeck, A. Sambrowski, J. Fiurášek and R. Schnabel, *Quantum non-Gaussianity of frequency up-converted single photons*, Optics Express **22**, 22808 (2014). 52
- [62] S. Ast, A. Sambrowski, M. Mehmet, S. Steinlechner, T. Eberle and R. Schnabel, *Continuous-wave nonclassical light with gigahertz squeezing bandwidth*, Optics letters **37**, 2367 (2012). 54, 56, 59, 61
- [63] S. Ast, M. Mehmet and R. Schnabel, *High-bandwidth squeezed light at 1550 nm from a compact monolithic PPKTP cavity*, Optics express **21**, 13572 (2013). 66, 72, 79, 80, 89

- [64] R. J. Senior, G. N. Milford, J. Janousek, a. E. Dunlop, K. Wagner, H.-A. Bachor, T. C. Ralph, E. H. Huntington and C. C. Harb, *Observation of a comb of optical squeezing over many gigahertz of bandwidth*, Optics express **15**, 5310 (2007). 79
- [65] K. McKenzie, N. Grosse, W. P. Bowen, S. E. Whitcomb, M. B. Gray, D. E. McClelland and P. K. Lam, *Squeezing in the Audio Gravitational-Wave Detection Band*, Physical Review Letters **93**, 161105 (2004). 79
- [66] G. Breitenbach, T. Müller, S. F. Pereira, J.-P. Poizat, S. Schiller and J. Mlynek, *Squeezed vacuum from a monolithic optical parametric oscillator*, Journal of the Optical Society of America B **12**, 2304 (1995). 79
- [67] B. Boulanger, I. Rousseau, J. P. Fève, M. Maglione, B. Menaert and G. Marnier, *Optical studies of laser-induced gray-tracking in KTP*, IEEE Journal of Quantum Electronics **35**, 281 (1999). 86
- [68] H. Mabuchi, E. S. Polzik and H. J. Kimble, *Blue-light-induced infrared absorption in KNbO₃*, Journal of the Optical Society of America B **11**, 2023 (1994). 86
- [69] J. Hirohashi, V. Pasiskevicius, S. Wang and F. Laurell, *Picosecond blue-light-induced infrared absorption in single-domain and periodically poled ferroelectrics*, Journal of Applied Physics **101**, 033105 (2007). 86
- [70] P. K. Lam, *Applications of Quantum Electro-Optic Control and Squeezed Light*, PhD Thesis, Australian National University, 1998. 103
- [71] M. D. Reid, *Demonstration of the Einstein-Podolsky-Rosen paradox using nondegenerate parametric amplification*, Physical Review A **40**, 913 (1989). 105
- [72] F. Furrer, T. Franz, M. Berta, A. Leverrier, V. B. Scholz, M. Tomamichel and R. F. Werner, *Continuous variable quantum key distribution: Finite-key analysis of composable security against coherent attacks*, Physical review letters **109**, 100502 (2012). 105
- [73] T. Tyc and N. Korolkova, *Highly non-Gaussian states created via cross-Kerr nonlinearity*, New Journal of Physics **10**, 023041 (2008). 108

BIBLIOGRAPHY

- [74] A. Pal Singh, *Aufbau eines gefalteten Wanderwellenresonators zur Beobachtung des kaskadierten Kerr-Effekts bei 1550nm*, Diploma thesis, Leibniz Universität Hannover, 2013. 108
- [75] A. G. White, P. K. Lam, D. E. McClelland, H.-A. Bachor and W. J. Munro, *Kerr noise reduction and squeezing*, Journal of Optics B: Quantum and Semiclassical Optics **2**, 553 (2000). 108
- [76] A. Khalaidovski, *Der optische Kerr-Effekt im Fabry-Perot Interferometer*, Diploma thesis, Universität Hannover, 2007. 108, 116
- [77] A. Thüring, *Investigations of coupled and Kerr non-linear optical resonators*, PhD Thesis, Universität Hannover, 2009. 108, 116
- [78] M. Heurs, J. G. Webb, T. C. Ralph and E. H. Huntington, in *Lasers and Electro-Optics/Quantum Electronics and Laser Science Conference: 2010 Laser Science to Photonic Applications, CLEO/QELS 2010* (PUBLISHER, 2010). 109
- [79] C. B. Clausen, O. Bang and Y. S. Kivshar, *Spatial solitons and induced Kerr effects in quasi-phase-matched quadratic media*, Physical review letters **78**, 4749 (1997). 115
- [80] K. Wang, L. Qian, D. Zhang, H. Yang and H. Zhu, *Cascaded nonlinear phase shifts in quasi-phase-matched structures*, Physical Review A **76**, 013805 (2007). 115
- [81] A. Thüring and R. Schnabel, *Critical Kerr nonlinear optical cavity in the presence of internal loss and driving noise*, Physical Review A **84**, 033839 (2011). 116
- [82] S. Zippilli, M. Paternostro, G. Adesso and F. Illuminati, *Entanglement Replication in Driven Dissipative Many-Body systems*, Physical Review Letters **110**, 040503 (2013). 123
- [83] S. Zippilli and F. Illuminati, *Non-Markovian dynamics and steady-state entanglement of cavity arrays in finite-bandwidth squeezed reservoirs*, Physical Review A **89**, 033803 (2014). 123
- [84] T. Eberle, V. Händchen, J. Duhme, T. Franz, F. Furrer, R. Schnabel and R. F. Werner, *Gaussian Entanglement for Quantum Key Distribution from a Single-Mode Squeezing Source*, **21**, 13 (2011). 124

Acknowledgements

The time I spent at the Albert Einstein institute during my PhD thesis was full of people that I would like to thank.

First of all, I like to thank Roman Schnabel for being my PhD advisor and guide through the world of squeezed light. It was amazing to be part of his quantum interferometry group. I want to thank Karsten Danzmann for letting me be a part of the leading institute on gravitational physics and for being my second PhD thesis advisor. Special thanks to Klemens Hammerer who will be the chair in my PhD thesis defense and who was always helping me to understand some theory in quantum optics.

I like to say thank you to my amazing girlfriend Melanie. She did not only fill my personal life with joy but did also contribute a lot in my work. Without you I would have failed in the entanglement measurement.

A great thank you to Aiko who was teaching me a lot as the supervisor of my diploma thesis. It was a pleasure working with you and having some beverages after work.

My office mates Henning and Olli deserve some special thanks. The fun we had in the office was taking us directly to Nerdvana. In this context, I also like to thank my new office mates Germán and Thomas who were keeping up to the tradition of my former mates.

I like to thank Amrit, Axel and Ramon for surviving my treatment as their thesis supervisor.

Moritz deserves a massive thank you for a lot of help in the lab and especially for the design of the GHz homodyne detector.

Thank you Colin, Katha, Heather, Olli, Melanie and Steffen for the Game of Thrones breakfast and Heather for having plenty of cake together.

Thank you Amrit, Axel, Christoph, Heather, Melanie, Ramon and Sacha for proof reading my thesis.

I also like to thank Carl, Hauke and Martin for sharing a flat with me for several years and for being very good friends of mine.

I like to thank Nico Lastzka for programming N.L.C.S. and Andreas Freise for programming “Finesse”. Both simulation tools were exces-

BIBLIOGRAPHY

sively used during my PhD time.

There are several people I would like to thank due to enriching my personal life or for helping me during my PhD thesis. Some of them are Andreas, Amrit, Arndt, Axel, Benni, Christina B., Christina V., Christoph, Daniel, Dirk, Felix, Germán, Henning K., Henning V., Katha, Kirsten, Lisa, Marina, Max, Michi, Moritz, Oliver, Phillip K., Phillip S., Ramon, Sabine, Sascha, Sebastian, Sina, Stefan, Steffen, Thomas, Timo, Tobias G., Tobias M., Vitus, Yvonne as well as all guys from the electronic workshop, the mechanical workshop and the secretaries.

I like to thank the AEI football team for letting me participate in winning the physics cup.

Arigatou to Hidetaka Miyazaki of From Software.

I acknowledge support from the IMPRS on Gravitational Wave Astronomy, the European grant QESSENCE and the cluster of excellence QUEST.

Last but not least and definitely the most important thank you goes to my parents. Vielen Dank Mama und Papa für eure Unterstützung all die Jahre hinweg.

Curriculum Vitae

Personal Data

Stefan Ast
Hahnenstraße 6
30167 Hannover

Email: stefanast@gmx.de

Born: October 3, 1983 in Verden
Single, german

Academic History

- | | |
|-----------|--|
| 1990–1996 | Grundschule und Orientierungsstufe, Dörverden |
| 1996–2003 | Gymnasium am Wall, Verden |
| 2003–2009 | Diploma studies in Physics at Gottfried Wilhelm Leibniz Universität Hannover |
| 2008–2009 | Diploma thesis in Physics at the Institute for Gravitational Physics, Gottfried Wilhelm Leibniz Universität Hannover

Diploma thesis:
Erzeugung gequetschter Lichtfelder mit einer Bandbreite über 1 GHz (Generation of squeezed light with a bandwidth of more than 1 GHz) |
| 2009–2014 | Doctoral studies in Physics at the Institute for Gravitational Physics, Gottfried Wilhelm Leibniz Universität Hannover |

List of Publications

- [1] **S. Ast**, M. Mehmet and R. Schnabel, *High-bandwidth squeezed light at 1550 nm from a compact monolithic PPKTP cavity*, Optics express **21**, 13572 (2013).
- [2] **S. Ast**, A. Sambrowski, M. Mehmet, S. Steinlechner, T. Eberle and R. Schnabel, *Continuous-wave nonclassical light with gigahertz squeezing bandwidth*, Optics letters **37**, 2367 (2012).
- [3] **S. Ast**, R. Moghadas Nia, A. Schönbeck, N. Lastzka, J. Steinlechner, T. Eberle, M. Mehmet, S. Steinlechner and R. Schnabel, *High-efficiency frequency doubling of continuous-wave laser light*, Optics letters **36**, 3467 (2011).
- [4] J. Steinlechner, **S. Ast**, C. Krüger, A. Pal Singh, T. Eberle, V. Händchen and R. Schnabel, *Absorption measurements of periodically poled potassium titanyl phosphate (PPKTP) at 775 nm and 1550 nm*, Sensors **13**, 565 (2013).
- [5] M. Mehmet, **S. Ast**, T. Eberle, S. Steinlechner, H. Vahlbruch and R. Schnabel, *Squeezed light at 1550 nm with a quantum noise reduction of 12.3 dB*, Optics express **19**, 25763 (2011).
- [6] J. Aasi, J. Abadie, ...**S. Ast**, ..., *et al.*, *Application of a Hough search for continuous gravitational waves on data from the fifth LIGO science run*, Classical and Quantum Gravity **31**, 085014 (2014).
- [7] J. Aasi, J. Abadie, ...**S. Ast**, ..., *et al.*, *Constraints on cosmic strings from the LIGO-Virgo gravitational-wave detectors*, Physical review letters **112**, 131101 (2014).
- [8] J. Aasi, J. Abadie, ...**S. Ast**, ..., *et al.*, *Gravitational waves from known pulsars: results from the initial detector era*, The Astrophysical Journal **785**, 119 (2014).

- [9] J. Aasi, J. Abadie, ...**S. Ast**, ..., *et al.*, *First searches for optical counterparts to gravitational-wave candidate events*, The Astrophysical Journal Supplement Series **211**, 7 (2014).
- [10] J. Aasi, B. Abbot, ...**S. Ast**, ..., *et al.*, *Search for gravitational waves associated with gamma-ray bursts detected by the Inter-Planetary Network*, Physical review letters **113**, 011102 (2014).
- [11] J. Aasi, B. Abbot, ...**S. Ast**, ..., *et al.*, *Methods and results of a search for gravitational waves associated with gamma-ray bursts using the GEO600, LIGO, and Virgo detectors*, Physical Review D **89**, 122004 (2014).
- [12] J. Aasi, B. Abbot, ...**S. Ast**, ..., *et al.*, *Narrow-band search of continuous gravitational-wave signals from Crab and Vela pulsars in Virgo VSR4 data*, arXiv preprint arXiv:1410.8310 (2014).
- [13] J. Aasi, B. Abbot, ...**S. Ast**, ..., *et al.*, *Characterization of the LIGO detectors during their sixth science run*, arXiv preprint arXiv:1410.7764 (2014).
- [14] J. Aasi, B. Abbot, ...**S. Ast**, ..., *et al.*, *Searching for stochastic gravitational waves using data from the two co-located LIGO Hanford detectors*, arXiv preprint arXiv:1410.6211 (2014).
- [15] J. Aasi, J. Abadie, ...**S. Ast**, ..., *et al.*, *Search for long-lived gravitational-wave transients coincident with long gamma-ray bursts*, Physical Review D **88**, 122004 (2013).
- [16] J. Aasi, J. Abadie, ...**S. Ast**, ..., *et al.*, *Einstein@ Home all-sky search for periodic gravitational waves in LIGO S5 data*, Physical Review D **87**, 042001 (2013).
- [17] J. Aasi, J. Abadie, ...**S. Ast**, ..., *et al.*, *Search for gravitational waves from binary black hole inspiral, merger, and ringdown in LIGO-Virgo data from 2009–2010*, Physical Review D **87**, 022002 (2013).
- [18] J. Aasi, J. Abadie, ...**S. Ast**, ..., *et al.*, *Prospects for localization of gravitational wave transients by the Advanced LIGO and Advanced Virgo Observatories*, arXiv preprint arXiv:1304.0670 (2013).

- [19] J. Aasi, J. Abadie, ...**S. Ast**, ..., *et al.*, *Parameter estimation for compact binary coalescence signals with the first generation gravitational-wave detector network*, *Physical Review D* **88**, 062001 (2013).
- [20] J. Aasi, J. Abadie, ...**S. Ast**, ..., *et al.*, *Enhanced sensitivity of the LIGO gravitational wave detector by using squeezed states of light*, *Nature Photonics* **7**, 613 (2013).
- [21] J. Aasi, J. Abadie, ...**S. Ast**, ..., *et al.*, *Directed search for continuous gravitational waves from the Galactic center*, *Physical Review D* **88**, 102002 (2013).
- [22] J. Aasi, J. Abadie, ...**S. Ast**, ..., *et al.*, *The characterization of Virgo data and its impact on gravitational-wave searches*, *Classical and Quantum Gravity* **29**, 155002 (2012).
- [23] P. Evans, J. Fridriksson, ...**S. Ast**, ..., *et al.*, *Swift follow-up observations of candidate gravitational-wave transient events*, *The Astrophysical Journal Supplement Series* **203**, 28 (2012).